Würzburger Geographische Arbeiten

Julius-Maximilians-
UNIVERSITÄT WÜRZBURG

Band 123

Christian Büdel

Quaternary alluvial fan morphodynamics and basin sedimentation in North Iran

Würzburg University Press

Christian Büdel

Quaternary alluvial fan morphodynamics and basin sedimentation in North Iran

WÜRZBURGER GEOGRAPHISCHE ARBEITEN

Herausgegeben vom Institut für Geographie und Geologie der Universität Würzburg in Verbindung mit der Geographischen Gesellschaft Würzburg

Herausgeber
R. Baumhauer, B. Hahn, H. Job, H. Paeth, J. Rauh, B. Terhorst

Schriftleitung
R. Klein

Band 123

Die Schriftenreihe Würzburger Geographische Arbeiten wird vom Institut für Geographie und Geologie zusammen mit der Geographischen Gesellschaft herausgegeben. Die Beiträge umfassen mit wirtschafts-, sozial- und naturwissenschaftlichen Forschungsperspektiven die gesamte thematische Bandbreite der Geographie. Der erste Band der Reihe erschien 1953.

Christian Büdel

Quaternary alluvial fan morphodynamics and basin sedimentation in North Iran

Würzburg University Press

Dissertation, Julius-Maximilians-Universität Würzburg
Philosophische Fakultät, 2017

Eingereicht mit dem Titel:
Integrative geomorphological mapping approach for reconstructing Quaternary alluvial fan morphodynamics and basin sedimentation in North Iran

Gutachter: Prof. Dr. Roland Baumhauer, Prof. Dr. Barbara Sponholz

Impressum

Julius-Maximilians-Universität Würzburg
Würzburg University Press
Universitätsbibliothek Würzburg
Am Hubland
D-97074 Würzburg
www.wup.uni-wuerzburg.de

© 2020 Würzburg University Press
Print on Demand

ISSN 0510-9833 (print)
ISSN 2194-3656 (online)
ISBN 978-3-95826-114-3 (print)
ISBN 978-3-95826-115-0 (online)
DOI 10.25972/WUP-978-3-95826-115-0
urn:nbn:de:bvb:20-opus-184508

Except otherwise noted, this document – excluding the cover – is licensed under the Creative Commons Attribution-ShareAlike 4.0 International License (CC BY-SA 4.0):
https://creativecommons.org/licenses/by-sa/4.0/

The cover page is licensed under the Creative Commons Attribution-NonCommerical-NoDerivatives 4.0 International License (CC BY-NC-ND 4.0):
https://creativecommons.org/licenses/by-nc-nd/4.0

Acknowledgements

I gratefully thank my primary advisor Prof. Dr. Roland Baumhauer for the opportunity to do this project and for the always reliable support during the last years. I am very thankful to my colleague and friend M.Sc. Seyed Majid Padashi, who was my experienced partner during all field work and who also never hesitated to be my sincere ears and my tongue in Iran. Majid always was the guarantor for safe and successful fieldwork. Also, I want to thank Prof. Dr. Reza Sarvati, Dr. Mahmoud Majidifard and Prof. Dr. Arash Malekian for welcoming me in Iran, the *mehmandust* they offered me, and for their scientific support. Furthermore, I gratefully thank for the professional support and the impressive logistics provided by the Geological Survey of Iran over several years of intense cooperation and field work. Special thanks for the Head of Geological Survey of Iran (GSI) Mr. Korehie, Deputy Manager of Geology Dr. Ghalamghash and his predecessor Dr. Ghassemi, Regional Geology Manager Dr. Shahidi and also Education and International affairs Manager Mr. Meyguni for kind support. I am also thankful to the Bayerische Forschungsallianz and the UniBund (Würzburg) for financial support. Furthermore, I would like to thank our cooperation partners in Germany, where Prof. Dr. Britta Schütt and Dr. Philipp Hoelzmann with their team (Freie Universität Berlin) provided excellent scientific support and laboratory facilities and Dr. Hoelzmann intensively helped to improve this work in several discussions and reviews. I want to express my sincere gratitude to Prof. Dr. Markus Fuchs and Dr. Johanna Lomax (Justus Liebig University Gießen), who were occupied with the OSL-dating tasks and providing excellent considerations about relative chronology and fundamentally enabled us to establish a valid chrono-stratigraphy for quaternary sediments. Furthermore Prof. Fuchs was my much-valued advisor for scientific approaches and project management. My acknowledgements also go to Prof. Dr. Martin Melles and Dr. Volker Wennrich (University of Cologne), for securely handling and investigating the sample cores and for measurements with their mulit-sensor core logger. I am very thankful to my colleagues in Würzburg. Dr. Erhard Schulz for advising me in microscopic analysis and thin section investigations, Dr. Tobias Ullmann for remote sensing expertise and Martin Krech for laboratory and field work support. I also say thank you to all my former and recent colleagues from Würzburg for not only scientific support, namely Jens Brauneck, Daniel Jäger, Jürgen Kempf, Birigt Mannig, Günter Moritz, Andreas Paxian, Ibrahim Sani, Christine Sandmeier, Doro Schill, Anja Scholten, Daniel Schwindt, Angela Tintrup gen. Suntrup, Inka Wilhelm.

Finally, I would like to express my deep gratitude to my family. My parents Burkhard and Evelin and my sister Ulrike for waking and cultivating my enthusiasm for understanding nature. I want to thank my wife Tina and my daughter Maria for coming to my life and for sharing this fascination with me. All of you allways encouraged, helped and supported me, and your patience and endurance ensured my vigor to fulfill this project.

Christian Büdel – Sömmersdorf, December 2016

Content

Content I
List of Figures III
List of Tables V
List of Pictures VI
Abstract VII
Zusammenfassung IX

1 Introduction 1
1.1 Hypothesis and project aims 1
1.2 Important aspects of geomorphologic research in Iran 3
1.2.1 A brief typology of playa, playa lake and sabkha 3
1.2.2 A summary of climate and lake level change in Iran 6
1.3 Regional Setting and study sites 10
1.3.1 Damghan Basin 10
1.3.2 Study Sites 14

2 Material and Methods 17
2.1 Geomorphological mapping and remote sensing 17
2.1.1 Geomorphological database and mapping standards 17
2.1.2 Base data and data analyses 22
2.2 Specific mapping and stratigraphic field work 29
2.2.1 Ground penetrating radar survey 29
2.2.2 Stratigraphic field work and section analysis 31
2.3 Analyzing geophysical and geochemical properties 33
2.4 Dating and establishing a valid chronostratigraphy 35

3 Results and Synthesis 37
3.1 Quaternary mapping and map unit description 37
3.1.1 Map sheets overview 37
3.1.2 Stratigraphic description of map units 39
3.1.2.1 Precambrian 39
3.1.2.2 Cambrian 39
3.1.2.3 Ordovician 40
3.1.2.4 Devonian 40
3.1.2.5 Triassic 41
3.1.2.6 Jurassic 41
3.1.2.7 Miocene 41
3.1.2.8 Neogen 41
3.1.2.9 Quaternary 42
3.1.3 Characteristics and spatial distribution of map elements 46
3.2 Description of alluvial apron geomorphology and surface stratigraphy 55

3.2.1 Prospectional mapping results and findings from stratigraphic fieldwork 55
3.2.2 Detailed field descriptions of the sections 62
3.2.3 Results of Laboratory analysis 71
3.3 Stratigraphy and sedimentological features of the playa sediments 76
3.3.1 Stratigraphy and initial core description 76
3.3.2 Geophysical and geochemical properties of playa sediment samples 76
3.4 Chronological order of investigated landforms and landform-genesis 95

4 Discussion 100
4.1 Correlation of basin morphology and playa sediments 100
4.2 Autochthonous and allochthonous gypsum contents 103
4.3 Chronostratigraphic framework 107
4.4 Morphodynamic history and phases of basin sedimentation 108

5 Conclusions 111
5.1 Geomorphological relationships 111
5.2 Geoarchives for morphogenetic correlation 111

References 113
Appendix I 123
Appendix II 124

List of Figures

Figure 1.1.1: The location of Damghan Basin in northeastern part of Iran 1
Figure 1.1.2: Relationship of morphogenetic proxy data and significance of different geoarchives. 2
Figure 1.2.1: Three distinct areas of process and structure and the playa-sabkha-terminology. 5
Figure 1.2.2: Current Köppen-Geiger climate classification of Iran. Additionally, to the area of interest (AOI).....7
Figure 1.2.3: Climatic Groups statistically derived from observational data.....8
Figure 1.2.4: Indications of past periods of varying humidity as derived from lake sediments in Northwestern Iran and Southeast Turkey. 9
Figure 1.3.1: The main landscapes of the basin and the sample sites of the study.....11
Figure 1.3.2: The climate gradient in Damghan basin. 13
Figure 1.3.3: Monthly averages and annual trends calculated from observational data (2002-2014) from Damghan City weather station. 14
Figure 2.1.1: The geodatabase concept of the Quaternary mapping project in Damghan.....21
Figure 2.1.2: The concept chart of geomorphological mapping and multi-method GIS analysis. 28
Figure 2.2.1: Locations of ground penetrating radar survey. 30
Figure 3.1.1: Field characteristics and optical differentiation of eroded alluvial fan surfaces 1 to 5. 43
Figure 3.1.2: Overview map of geomorphostructural map units in the mapping project.....48
Figure 3.1.3: Relationship between alluvial surfaces and the morphometry of their bounding slopes.....50
Figure 3.1.4: Overview map of geomorphodynamic map elements in the mapping project.....52
Figure 3.2.1: Overview of the GPR-profiles described in this study. 56
Figure 3.2.2: Radargrams of fine sediments at distal end of alluvial apron. 57
Figure 3.2.3: Radargram of Q^{al}_{0} prograded alluvial fan 58
Figure 3.2.4: Sediment logs of eroded alluvial fan surfaces. 60
Figure 3.2.5: The maps show relationships between mapped landforms (e.g. chronostratigraphic units) and typical spectral characteristics of their surfaces. 61
Figure 3.2.6: Location of section sites with main landscapes at the alluvial apron. 63
Figure 3.2.7: Drawing of sections S03-C-I & -II (bottom right) and S03-D-I (bottom left). 66
Figure 3.2.8: Drawing of sections S03-B-I & -II. 67
Figure 3.3.1: Drawing of sections S03-A-I and S03-A-II. 78

Figure 3.3.2: Locations of drilling sites B04-A and B02-A....81
Figure 3.3.3: Core log from playa sediments at site B04-A....82
Figure 3.3.4: High-resolution line scans of core B04-A....83
Figure 3.3.5: The granulometry of the combined section S03-A-I and –II....88
Figure 3.3.6: The element contents of section S03-A-I and-II......89
Figure 3.3.7: Granulometry and statistical and geochemical indicators of core B04-A reveal considerably shifting conditions at the c hange from facies 5-6 to 3-4. 91
Figure 3.3.8: The description and analytical data from core B04-A reveals a major change from ~400 cm upwards. 92
Figure 3.3.9: Aluminum and Titanium based potentials for biogenic silicates (BSi) in playa related sediments......94
Figure 3.4.1: Distribution of OSL ages and quaternary units.....97
Figure 4.1.1: The outlined facies of core B04-A. 101
Figure 4.1.2: The correlation of the lake related sediments shows several accumulation phases during the time of the maximum lake extent.....102
Figure 4.2.1: Sulfur and Strontium distribution in core B04-A and in terrace section S03-A-I & -II.....104
Figure 4.2.2: Relationships between core facies 3-4 and “Eroded lake and playa deposits”. 106
Figure 4.4.1: Morphogenetic model of alluvial apron development and OSL ages: 109
Figure 4.4.2: The past period humidity for Damghan Basin, as interpreted from morphological and geochemical evidence presented in this study.....110

List of Tables

Table 1.3.1: Coverage of the 11.4 km² large catchment, lithology, and age of geological formations within the combined watersheds of the investigated alluvial apron sequence. 15
Table 2.1.1: Overview of main data entries stored in the mapping projects geodatabase 18
Table 2.1.2: Coded values for new geomorphological classes, which were added to the GMK5-legend standard values. 19
Table 2.1.3: Overview of remote sensing data used in the project. 24
Table 2.3.1: List of applied laboratory analysis. 34
Table 3.1.1: Total area and area percentage of all mapping units, with focus on the quaternary units. 46
Table 3.1.2: Quaternary map units' zonal histograms for elevation- and slope-classes. 47
Table 3.1.3: The mapped steps and slopes and the percentage of their connection to distinct alluvial fan and apron surfaces. 54
Table 3.2.1: Clast analysis data shows typical characteristics of increased transport distances from medial (S03-C-II) to distal (S03-B-II) area of the alluvial fan. 60
Table 3.2.2: The layer properties of section S03-D-I 64
Table 3.2.3: The layer properties of section S03-C-II. 65
Table 3.2.4: The layer properties of section S03-C-I. 65
Table 3.2.5: The layer properties of section S03-B-II. 69
Table 3.2.6: The layer properties of section S03-B-I. 70
Table 3.2.7: Physical and chemical properties of eroded alluvial apron sediments. 71
Table 3.2.8: Content of selected major and minor elements in eroded a lluvial apron sediments. 72
Table 3.2.9: Physical and chemical properties of young alluvial fan generations. 73
Table 3.2.10: Content of selected major and minor elements in young alluvial fans. 74
Table 3.2.11: Top Layer characteristics of the sections reveal their chronostratigraphic relationship and the representative potential of the sections for the map units. 75
Table 3.2.12: Mineralogy derived from XRD measurements. Specified minerals are given with Powder Diffraction File (PDF) reference number. 76
Table 3.3.1: The layer properties of section S03-A-I & -II.. 80
Table 3.3.2: Segment description of core B04-A. 85
Table 3.4.1: OSL sample and section descriptions with map units. 96
Table 3.4.2: OSL ages and luminescence properties of the sediments. 96

List of Pictures

Picture 1.3.1: View to northern Alborz slope from south of the young alluvial fans S03-B. The fine sediments terrace clearly divides older from younger fan generations (Picture: C. Büdel, 2010). 10
Pictures 3.2.1: Alluvial fan surface $Q_{ap}5$ has a well-developed gypsic horizon with beard-shaped gypsum crystals of up to 14 cm in length; the right picture shows the excavated gypsum-beards (scale in cm; Pictures: C. Büdel, 2011). 59
Pictures 3.2.2: Section S03-B-I before torrential rains set in (above) and S03-B-II after a thunderstorm eroded the right handed wall (below) (Pictures: C. Büdel, 2011) 68
Picture 3.3.1: The Coring Site B04-A in the central playa of Damghan is characterized by massive halite salt crusts with polygonal structures (Picture: C. Büdel, 2012). 77
Picture 3.3.2: The root-shaped lime concretions from S03-A-II may indicate a former littoral area (Picture: C. Büdel, 2010) 79

Abstract

Several hundred meter thick alluvial fans are dominating the landscape of semiarid plains of north-eastern Iranian mountain-talus. These fans developed since Miocene times and are still prograding today. They are storing and transporting a major amount of weathered debris from the mountain ranges and sediments are directed to the depressions of the endorheic basins. In this course, the debris gets increasingly weathered and abraded to sand silt and clay fractions, which finally constitute the fine loamy layers of the typical central playa lakes and playas.

The study focused on the detailed investigation of a characteristic section of this prominent sediment cascades. The sediments were comprehensively documented by using a fully analytical geomorphological mapping approach, also suitable for the classification of the sediment's geomorphological system context. Therefore, a geodatabase structure was developed, which is capable of managing and analyzing geomorphological data. The corresponding data was acquired using remote sensing imagery, digital elevation models and field mapping campaigns. Additionally, mapped sediments were selected and analyzed to reveal representative stratigraphic and sedimentologic characteristics. The fieldwork was conducted in Damghan Basin on sections in geomorphologically subdivided alluvial apron sediments. The corresponding, more regularly layered and partly laminated sediments from the central playa, were also investigated and comparably described. Attending to the preparation of profile sections and the percussion core probing, samples from both origins were taken. Detailed lithostratigraphical and geochemical analyses were carried out in the laboratory, in order to develop sound comparable sediment and sediment alteration indices. In addition, OSL sampling was done on distinct alluvial fan surfaces, and the samples were measured and dated in the laboratory in order to develop a functional chronostratigraphy.

The results of the geomorphological and stratigraphical investigations reveal five classes of surface ages on the alluvial apron. Parallel to that observation, the ramming core samples exhibit four main phases of sediment development in the playa, each with internal differentiation. This brings up opportunities for a valid correlation of continuously deposited playa sediments, with widespread alluvial surfaces. By considering the OSL ages of selected terrestrial and lacustrine layers, the stratigraphy and relative chronological order of the studied sediments, are aligned to Pleistocene and mid to late Holocene periods. This is also confirmed by proxy ages from the chronological framework of the landscape development, within the basin. Geophysical and geochemical data reveals roughly cyclic sedimentation and sediment alteration that can also be observed in genetically differing geoarchives from alluvial fan surfaces to the playa sediments. These parallel developments are confirmed by the sequence-stratigraphic order of the archives which is derived from geomorphological mapping. We postulate a time span covered by the playa sediments from today to late Pleistocene times. Drying and lake level retreat at the end of Pleistocene is documented in parallel geoarchives of terrestrial and lacustrine origin. Thus, geomorphologic landform-succession and alluvial fan morphogenesis, as

well as geochemical and geophysical fingerprinting data of playa sediments characterize this development. Therefore, it is present in the two youngest generations of alluvial fans, which deposited at the toe of the alluvial apron and which incorporate reworked still water deposits of a former lake level terrace. The geochemical parameters, like pH-value and Ca/S-ratio, in both, sediments of a former lake level and those from the recent playa extent exhibit a similar development. In addition, Ti/Al-ratio shows the potential for quantifying lake level retreat, as it seems to be tightly depending on lake level and increasing transportation distances along the sediment cascade. Furthermore, the dessication affected the citizens of the ancient city of 'Tepe Hissar', who were cut off the direct access to the lake as a water reservoir, and were prone to subsequent geomorphological processes changing their environment.

Major Findings

- Analytical geomorphological mapping is a key tool for understanding the sedimentation history of the Iranian Quaternary and for describing Quaternary stratigraphic units of North Iran.

- The younger playa deposits in Damghan Basin cover a time span from today to Late Pleistocene. They are 10 meters thick and reveal very low organic matter contents throughout the core.

- Drying and lake level retreat is documented in parallel geoarchives (1) in geomorphologic landform-succession and alluvial fan morphogenesis and (2) in geochemical and geophysical fingerprinting data of playa sediments. Also a correlation to the archaeological evidence from 'Tepe Hissar' was observed.

- Sequences of torrential sedimentation are detectable signals and can be correlated in both: playa sediments and landform morphology.

Zusammenfassung

Die nordostiranische Gebirgsabdachung wird maßgeblich von mehrere hundert Meter mächtigen Schwemmfächern gebildet. Die Aufschüttung der Schwemmfächer setze im Miozän ein und bis heute progradieren die Fächer ins Beckeninnere. Dabei transportieren und speichern sie den Großteil des Verwitterungsschutts der Gebirgszone und die Sedimente werden von hier weiter in die zentralen Depressionen der endorheischen Beckenlandschaften geleitet. Auf ihrem Weg wird der Schutt weiter zerkleinert und verwittert, und bildet schließlich in feinen Sand-, Schluff- und Tongemengelagen die Lehmschichten der typischen zentralen Playaseen und Playas.

Mit der vorliegenden Studie wurde ein charakteristischer Abschnitt dieser bedeutenden Sedimentkaskade detailliert untersucht. Durch einen vollanalytischen geomorphologischen Kartieransatz sollten die Sedimente umfangreich erfasst und in ihren geomorphologischen Systemzusammenhang gebracht werden. Zu diesem Zweck wurde eine Geodatenbankstruktur entwickelt, die die Verwaltung und Analyse geomorphologischer Daten ermöglicht. Die entsprechenden Dateneinträge wurden aus spektralen Fernerkundungsdaten, digitalen Geländemodellen und den Feldkartierungen mehrerer Expeditionen extrahiert. Für die kartierten Sedimente wurden an repräsentativen Standorten zusätzlich die stratigraphischen und sedimentologischen Charakteristika ermittelt und mit den Kartenelementen verknüpft. Für die Feldarbeiten wurden die Sedimente einer typischen Schwemmfächerschürze des Damghan Beckens geomorphologisch untergegliedert und ergraben. Entsprechend wurden die, das Ende der Sedimentkaskade bildenden, regelmäßiger geschichteten und zum Teil laminierten Sedimente der Playa sondiert und vergleichbar beschrieben. Die Landformen wurden als Kartenelemente im Vektorformat gespeichert und nach standardisierten geomorphologischen Konzepten in Systemelemente aus Form, Material und Prozess klassifiziert. Spezifiziert wurden die Landformen und Landformelemente dann in den Klassen Moprhometrie und Morphographie (Form), Morphostruktur (Material), Morphodynamik und Morphogenese (Prozess), sowie Geomorphologie (System Synthese). Begleitend zu den Kartierungen und der Bearbeitung der Profilschnitte und Rammkernsondagen, wurden die Schichten beider Sedimentationsräume detailliert beprobt.

Weitere Untersuchungen zu Lithostratigraphie, Geochronologie und Geochemie der Sedimente wurden im Labor ausgeführt und sollten aussagekräftige Indizes zu Sedimenteigenschaften und Art und Alter der Sedimentvariation erbringen. Neben pH- und Leitfähigkeitsmessungen, sowie der Ionenchromatographie leicht löslicher Salze, wurde für alle Proben die Granulometrie mittels Laserdiffraktometrie ermittelt. Die mineralogische Zusammensetzung wurde röntgendiffraktometrisch bestimmt. Haupt- und Nebenelemente wurden im Wesentlichen mit einer Kombination aus Röntgenfluoreszenzmessungen (XRF) und optischer Emissionsspektrometrie von Königswasseraufschlüssen mittels induktiv gekoppeltem Plasma (ICP-OES) analysiert. Altersbestimmungen konnten lediglich an ausgewählten Proben der terrestrischen Sedimente durchgeführt werden; dabei wurden im Labor Dosi-

metrie und Optisch Stimulierte Lumineszenz gemessen (OSL) und daraus die Alter modelliert.

Die Ergebnisse der geomorphologischen und stratigraphischen Untersuchungen zeigen fünf Hauptphasen vergangener Schwemmfächeroberflächenaktivität. Parallel dazu konnten in den Rammkernen der zentralen Playa vier in sich gegliederte Hauptsedimentationsphasen nachgewiesen werden. Die kontinuierlichen Akkumulationsphasen der Playasedimente bieten aussagekräftige Korrelationen mit den Aktivitätsphasen auf den ausgedehnten Flächen der Schwemmfächerschürze. Über die OSL-Alter der ausgewählten terrestrischen und lakustrinen Sedimentschichten können Stratigraphie und relative Chronologie der untersuchten Sedimente/Pleistozänen und mittel- bis spätholozänen Perioden zugeordnet und in die allgemeine Chronostratigraphie des Beckens eingefügt werden.

Die lithostratigraphischen und geochemischen Messungen lassen auf zyklische Sedimentationsphasen schließen, die sich über Geoarchive verschiedenen Ursprungs von der Schwemmfächerschürze bis in die zentrale Playa koppeln lassen. Diese stratigraphische Entwicklung wurde über die historisch-genetische Systemrekonstruktion im Zuge der geomorphologischen Kartierung in ihren sequenzstratigraphischen Zusammenhang gebracht und bestätigt so die parallele Entwicklung der verschiedenen Geoarchive. Die untersuchten Playasedimente belegen somit eine Zeitspanne vom Spätpleistozän bis zur aktuell anhaltenden Phase. Die Entwicklung der verschiedenen Sedimentkörper zeigt auch den Wechsel zu trockeneren Bedingungen und die Austrocknung eines früher ausgedehnten (Playa-)Sees in spätpleistozäner Zeit an. Sowohl die geomorphologische Landformensukzession und Schwemmfächermorphogenese, wie auch das Elementsignal und die veränderten geophysikalischen und geochemischen Eigenschaften der Playasedimente charakterisieren diese Entwicklung. So ist diese präsent in den beiden jüngsten Schwemmfächergenerationen, die am Fuß der Schwemmfächerschürze liegen und erodierte Sedimente einer ehemaligen Seeterrasse beinhalten. Auch geochemische Parameter, hier die pH-Werte und das Ca/S-Verhältnis, der Schichten in Position der ehemaligen Seeterrasse, und der Schichtung innerhalb der rezenten Playaausdehnung weisen auf die zunehmende Salinität des ehemaligen Sees im Zuge der Austrocknung hin. Ergänzend hat das Ti/Al-Verhältnis Potential den Seespiegelrückzug zu quantifizieren, indem es als Indikator für zunehmende Transportdistanzen entlang der Sedimentkaskade genutzt wird.

Der beobachtete Seespiegelrückgang und die Phasen der Schwemmfächeraktivität können weiterhin mit Humiditätsphasen korreliert werden, die aus verschiedenen See- und Sumpfsedimenten des Nordiran bekannt sind. So beginnt in Damghan mit der Jüngeren Dryas eine intensive Trockenphase mit veränderten klimatischen Bedingungen. Nach einer folgenden Humiditätsphase mit neuerlichem Seehochstand können zwei weitere Trockenphasen im Frühholozän ausgemacht werden. Die letzte Trockenphase setzt somit nach einer mittelholozänen Phase relativer Stabilität ein. Dies deckt sich wiederum mit archäologischen Befunden der antiken Stadt ‚Tepe Hissar', die unweit des heutigen Damghan gelegen, im Zuge des Seespiegelrüchgangs vom direkten Wasserzugang abgeschnitten worden sein muss.

Wesentliche Erkenntnisse

- Die analytisch-geomorphologische Kartierung bildet ein essentielles Werkzeug zur Untersuchung der Sedimentation im iranischen Quartär und zur Beschreibung der quartären stratigraphischen Einheiten des Nordiran.

- Die jüngeren Playasedimente des Damghan Beckens repräsentieren einen Zeitabschnitt, der von heute bis in das Spätpleistozän reicht. Sie weisen eine Mächtigkeit von 10 Meter auf und enthalten durchweg sehr geringe Anteile an organischer Substanz.

- Austrocknung und Seespiegelrückgang sind in Damghan parallel in zwei Geoarchivtypen dokumentiert. Sie zeigen sich (1) in der geomorphologischen Landformenfolge und Schwemmfächerentwicklung und (2) im Wandel der geochemischen und geophysikalischen Charakteristika der Playasedimente. Die Enticklung konnte auch mit dem archäologischen Befund der antiken Stadt „Tepe Hissar“ korelliert werden.

- Sequenzen mit torrentieller Sedimentation konnten ebenfalls in beiden Sedimentationsräumen erkannt und korreliert werden.

1 Introduction

1.1 Hypothesis and project aims

The Project, which is presented in this study, started in 2009 during a first field trip to the Damghan Basin in North Iran (Fig. 1.1.1). This first field trip established a close cooperation between the Geological Survey of Iran in Teheran and the Julius-Maximilians University in Würzburg. The cooperation partners agreed on the main objective of the joint efforts, which was an enhancement of 1:25 000 Geological maps of Iran regarding their informative content of quaternary stratigraphy. The research team selected Damghan Basin as a representative area for detailed studies about quaternary landscape development and basin sedimentation. Further investigations were scheduled and elaborated and the first questions were grouped around classification and approachability of potential geoarchives (cf. Büdel et al. 2017).

Figure 1.1.1: The location of Damghan Basin in northeastern part of Iran.

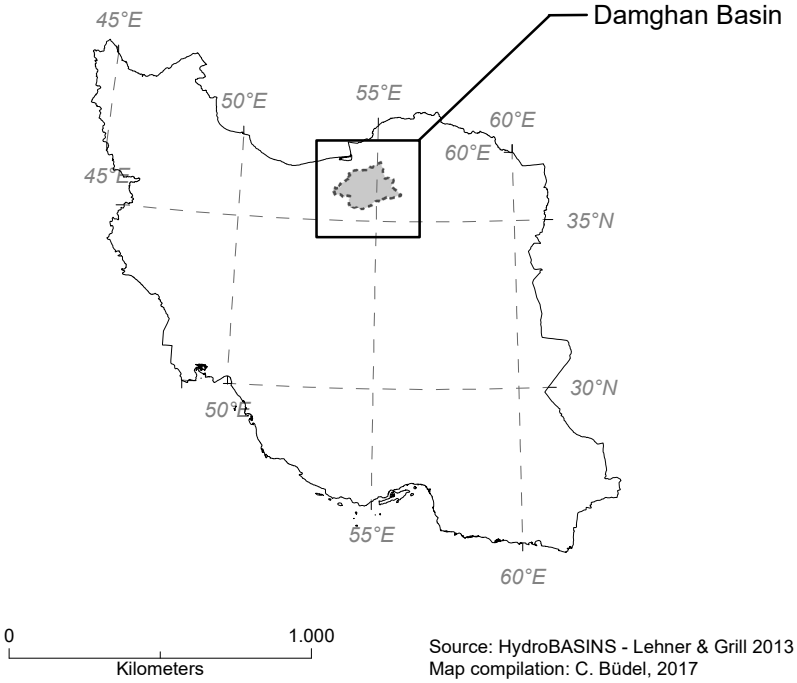

Initial literature work pointed to morphogenetic low activity inside the Basin of Damghan during middle to late Holocene (e.g. Krinsley 1970). Nevertheless, a first exemplary quantification of past deposition intensity in Damghan was achieved, by estimating the amount of sedimentation at the famous ancient city 'Tepe

Figure 1.1.2: Relationship of morphogenetic proxy data and significance of different geoarchives.

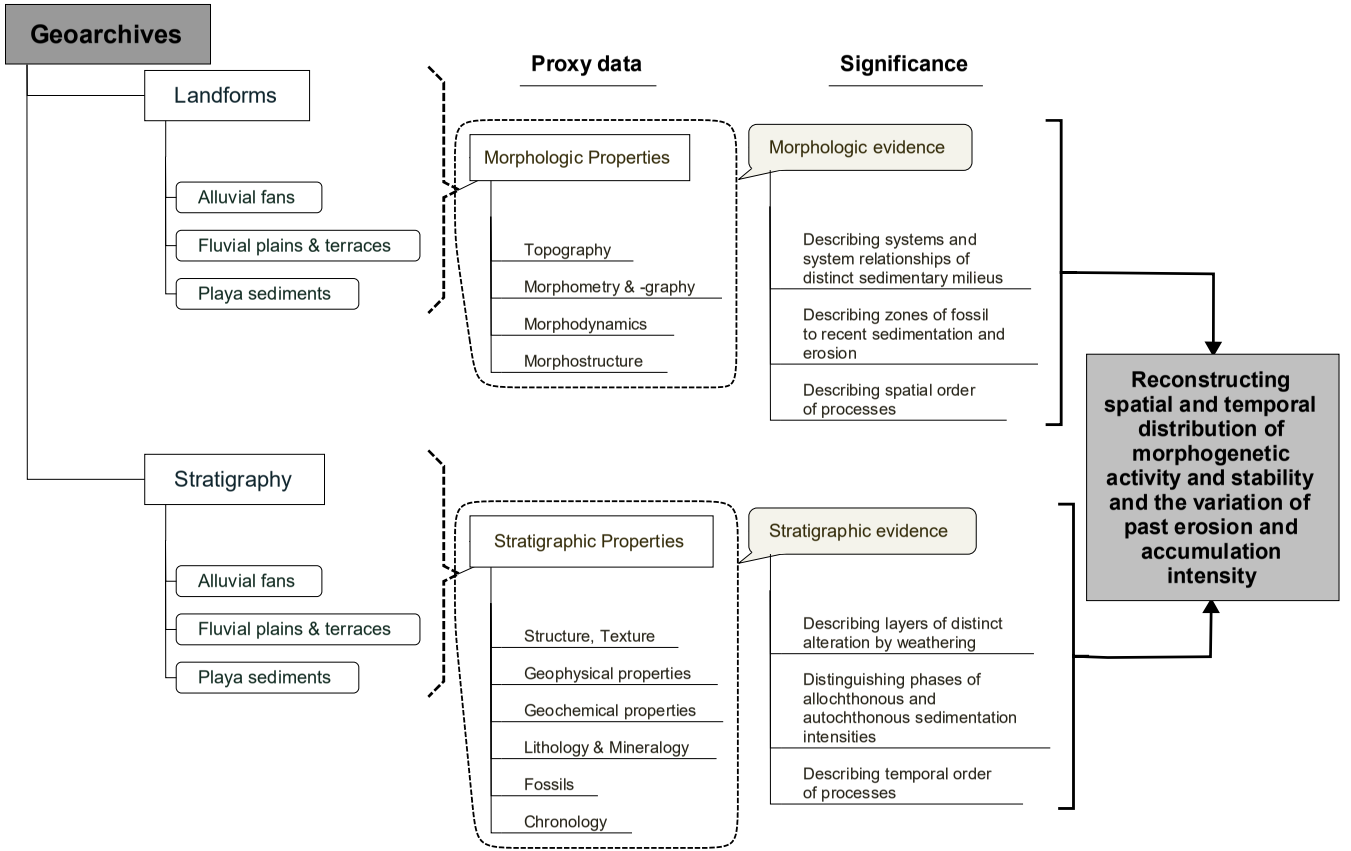

Source: Own illustration

Hissar'. The former citizens populated the place, which is located close to the modern city of Damghan, between 7 000 and 4 000 years ago. During scientific excavations in the early 20th century, the archaeologists observed 5 m of sediments. These sediments accumulated since about the onset of the settlement and formed the mound (general chronology from archeological findings, Schmidt 1937; ^{14}C-age from Costantini & Dyson, JR. 1990). This situation results in a linear sedimentation rate of 0.87 mm yr^{-1} for the period between 3 800 cal. BCE and 1937 CE. In addition to that observation, predominant morphological processes are evident in recent to fossil high-energy debris lobes forming big alluvial fans and aprons. Hence the hypotheses is appropriated, which says that dominating alluvial apron morphology, which is depending on extreme events capable of transporting high amounts of coarse grained gravels, should be related to significant variation of sediment stratigraphy in the playa. This leads to our scientific approach aiming at a validation of the previously mentioned hypothesis, in conjunction with a discovering and classification of potential geoarchives and their geomorphologic relationships. It includes the following questions: (1) where are promising geoarchives, (2) what types of archives are these and (3) how can they be thoroughly analyzed?

In particular, this approach covers a comprehensive localization and classification of differing alluvial apron, fluvial plain and playa sediment morphogenesis. A second step incorporates the investigation, sampling and laboratory analysis of sediments from classified and mapped areas of differing morphological processes and structures. The final comparison of geomorphologic and stratigraphic properties of the landforms with their physical and chemical properties reveals morphodynamic relationships between geoarchives in the basin (Fig. 1.1.2). Completing this, a first task is to compile a synopsis of frequently occurring interpretation difficulties, such as: dating options, a high impact of secondary processes reworking alluvial sediment covers (e.g. Haas et al. 2014), the spatial and temporal variability of surface abandonment, the high age differences of sediment bodies with comparable origin, multiple processes genesis, or the variability of high energy events. The consideration of these aspects requires a comprehensive geomorphological classification, which also enables a classification and analyzation of geoarchive-relationships between alluvial fans, fluvial terraces and plains and the playa.

1.2 Important aspects of geomorphologic research in Iran

1.2.1 A brief typology of playa, playa lake and sabkha

An appropriate first classification can be made for playa or salt pan and the endorheic or terminal basin. The salt pan is typically situated at the subjacent end of a descending sediment cascade. This means a series of slope fluvial and fluvial systems, which connect the mountain ranges where intensive weathering takes

place with a continental basin. The basin can be closed or open for further drainage, but the development of salt pans is a common observation in terminal or endorheic basins. Here the collected water may typically form episodical or ephemeral lakes (Schäfer 2005). The variability of warm arid to semi-arid climates controls the hydrologic balance in these systems, as well as evaporite precipitation, with typical carbonates (e.g. calcium carbonate, dolomite), sulfates (e.g. gypsum), and chlorides (e.g. Halite) (Stow 2008).

Several local expressions can be found for this type of terminal lake, or terminal basin, all with more or less ambiguous meaning. Among these are the North African *"schott"*, the North American *"playa"*, the Arabian *"sabkha"* and the Persian *"kavir"* (cf. Briere 2000; Chivas 2007; Schäfer 2005).

In contrary to the previously described continental sabkha-type, the so called *"coastal sabkhas"* are related to a basically littoral morphogenesis, which is represented by a marine chemical and mineral composition (Briere 2000).

Brier submits an attempt of a nomenclatorial consolidation of the terms, whereby he classifies into three basic related landform types (Briere 2000; cf. Chivas 2007):

- *Playa:* intracontinental basin with negative water balance for at least half of the year. The basin is dried out about >75 % of the year and typically evaporites precipitate during this period.

- *Playa Lake:* transitional form from playa to lake. Essentially, an ephemeral lake at its conversion to a playa-hypersaline-milieu. The basin is weather dried out for >75 % of the year, nor is it filled with water for more than 75 % of the year.

- *Sabkha:* flat basin, which is bound to shallow, marginal-marine localities. It is also characterized by increased gypsum contents, or frequent gypsum layers, which precipitated in succession of flooding with marine water, and together with an according solution of halite evaporites.

A diverging classification refers to Handford (1981), who defined *"sabkha"*, *"interdune sabkha"* and *"playa"* as the leading terms among these landforms. He worked out the typical composition of process phenomena for each landform and thus determines (1) marine-, (2) fluvial-lacustrine-, and (3) aeolian-dominated sabkha-types. These morphodynamic models can be classified and displayed in a triangle diagram, where Handford allocated examples of recent sabkha systems (Fig. 1.2.1; Handford 1981).

In this study the term "playa" is used as suggested by Handford, without a further distinction of playa and playa lake, as recommended by Brier.

The geochemical, and hydrochemical characteristics of playas and playa lakes are thoroughly investigated during various studies and the typical geomorphological inventory of their associated basins is described as followed (cf. Eugster & Hardie 1978; Eugster 1980; Chivas 2007):

Figure 1.2.1: Three distinct areas of process and structure in context of the playa-sabkha-terminology. The dominating process controls sediment type, internal geomorphology and facies distribution within the basin. Note, that the Sabzevar Playa, representing a typical central Iranian "kavir", is allocated to the fluvial-lacustrine dominated playa system.

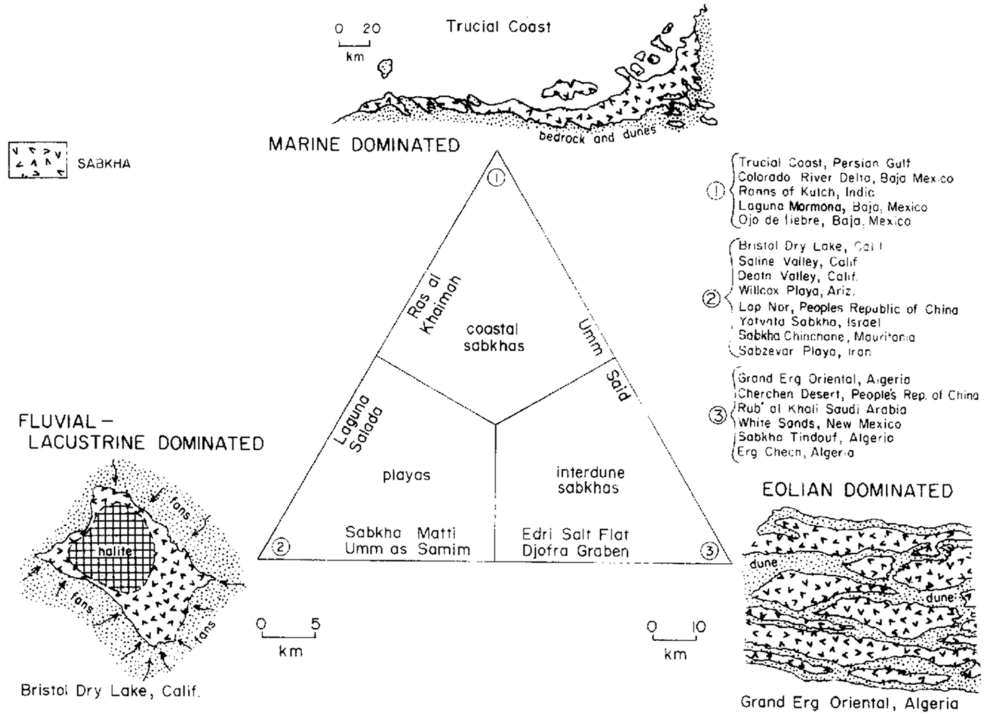

Source: Handford 1981: Fig. 1

1. *alluvial fan / bajada*
   - alluvial gravel and debris flow lobes; sandy-silty matrix

2. *sand flat / sand-silt fluvial plain*
   - distal sand and gravel related to sheet floods and rill erosion, with progressed clast abrasion
   - dune fields and aeolian sand accumulation

3. *(dry) mud flat / silty-clay flat*
   - ephemeral to episodical flooding with precipitation of evaporites
   - vesicular structures, "*puffy ground*", vertisols

4. *saline (wet) mudflat / clay flat*
   - ground water wells and precipitation of evaporites
   - abundant development polygonal structures and desiccation cracks

5. *ephemeral salt crust; (optional to 4.)*
   - extensive salt crust with polygonal structures and halite pressure ridges

6. *perennial / ephemeral salt lake; salt pan*
   - extensive salt precipitation, controlled by brine chemistry

7. *perennial / ephemeral fluvial plain (optional, between 2. and 3.)*
   - lateral fluvial transport of allochthonous stream sediments

8. *perennial / ephemeral springs*
   - precipitation of calcareous tufa / sinter
   - accumulation of sedimentary tufa

This study focusses on the morphodynamic of fluvial and slope-fluvial systems and on the development of lacustrine and playa to playa-lake sediments.

1.2.2 A summary of climate and lake level change in Iran

The investigation of lakes and lake level change naturally focused on northern and northeastern areas of Iran. Thereby, tracing the climatic gradient of temperature, precipitation and evaporation, which are primarily controlling Irans humidity (Kottek et al. 2006). Therefore, thoroughly investigated lake sediments in Iran are mainly located in areas, with currently warm temperate and snow climates (Fig. 1.2.2, Dsa and Csa climates). Hence, these areas bear a high potential for more humid conditions during past climate variability. Damghan Playa is situated in BSk and to a minor degree BWh climate – hot, and in elevated areas cold arid desert and steppe climates. This bears an increased risk for flooding and droughts and an accordingly decreased geoarchive potential.

The statistically derived climatic groups from Modarres (Modarres & Sarhadi 2011; Modarres et al. 2016) display a climate gradient, which is based on observational data (Fig. 1.2.3). This gives an additional climatic categorization for the basins incorporating the most prominent palaeoecological records, found and investigated in Iran. The Groups are defined as followed Modarres et al. 2016:

- G1: Arid and semiarid central Iranian highlands
- G2: Highland margins of central Iran (moister and colder)
- G3: Northwestern cold regions of Iran
- G4: Zagros Mountain lowlands
- G5, G7: Zagros Mountain ranges (precipitation: G7>G5)
- G6, G8: Mediterranean Caspian Sea margins (precipitation: G8>G6)

Paleoecologic studies derive information from palustrine/lacustrine and marine deposits from the Near East and western Asia. They suggest roughly Mediterranean climate behavior in Iran during Pleistocene and Holocene times. High level Rossby Waves partly controlled by the North Atlantic Oscillation propel cyclones that bring highest rainfall in winter and spring times. The second mechanism affecting Iranian climate evolution is the Indian Monsoon (cf. Staubwasser & Weiss 2006). Signals from different geoarchives suggest a strong monsoonal influence during early-mid

Figure 1.2.2: Current Köppen-Geiger climate classification of Iran. Additionally, to the area of interest (AOI=Damghan Basin), extensively investigated palaeoecologic records from closed basins are displayed. The AOI in Damghan Basin totally belongs to the BSk – cold arid steppe climate, while the basin of lake Urmia is currently covered by climatic classes from snow and warm temperate climate areas (Kottek et al. 2006).

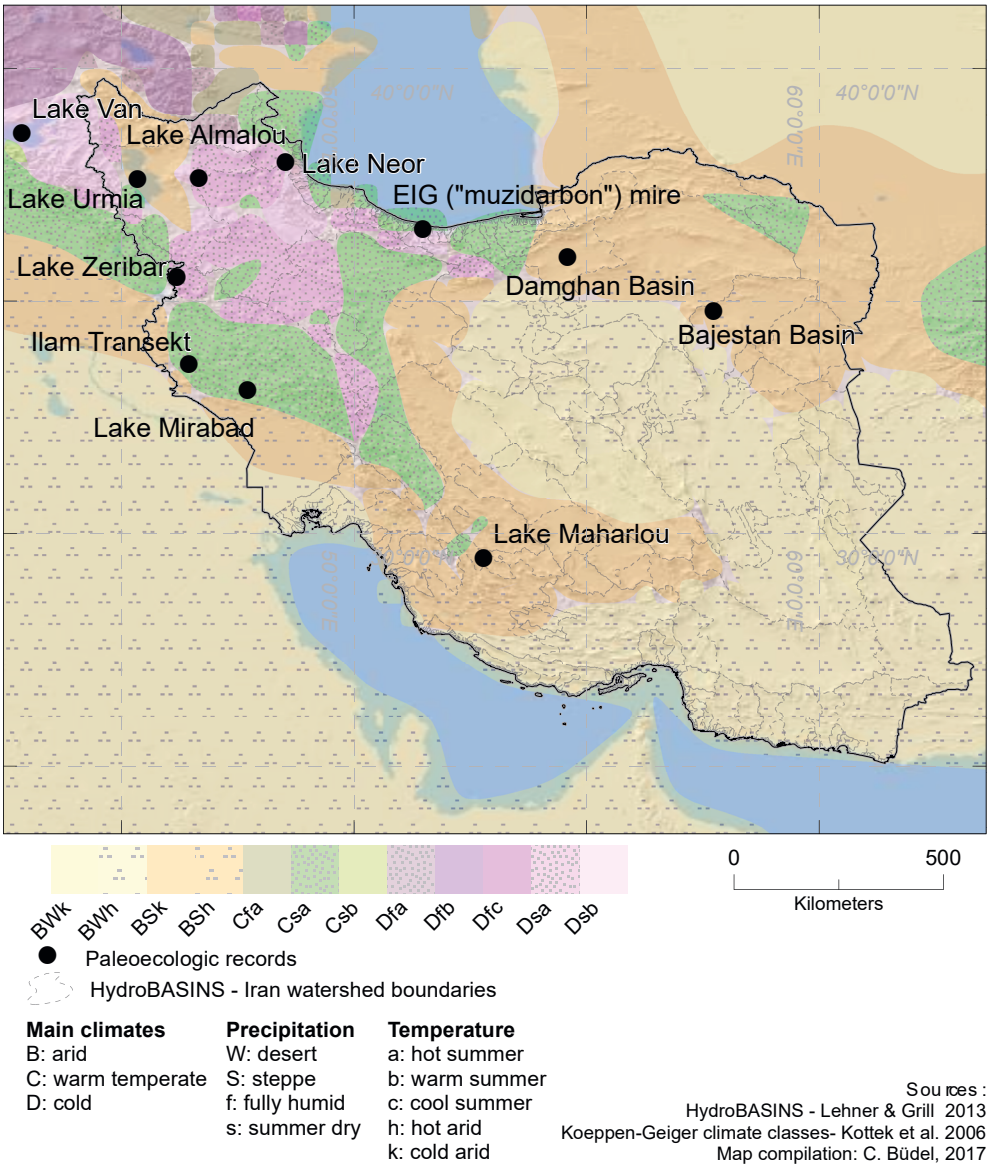

Holocene. For that period summer rainfalls are considered which supported generally moister conditions throughout Iran (Regard et al. 2006; Kober et al. 2013). For the time after this phase of lake level high stands, studies frequently describe one or

Figure 1.2.3: Climatic Groups statistically derived from observational data from synoptic weather stations (Modarres & Sarhadi 2011; Modarres et al. 2016) and extensively investigated paleoecologic records from closed basins in and close to Iran. For the AOI in Damghan Basin and similar basins within G1, potentials for detailed paleoecologic record are supposed to be comparably poor.

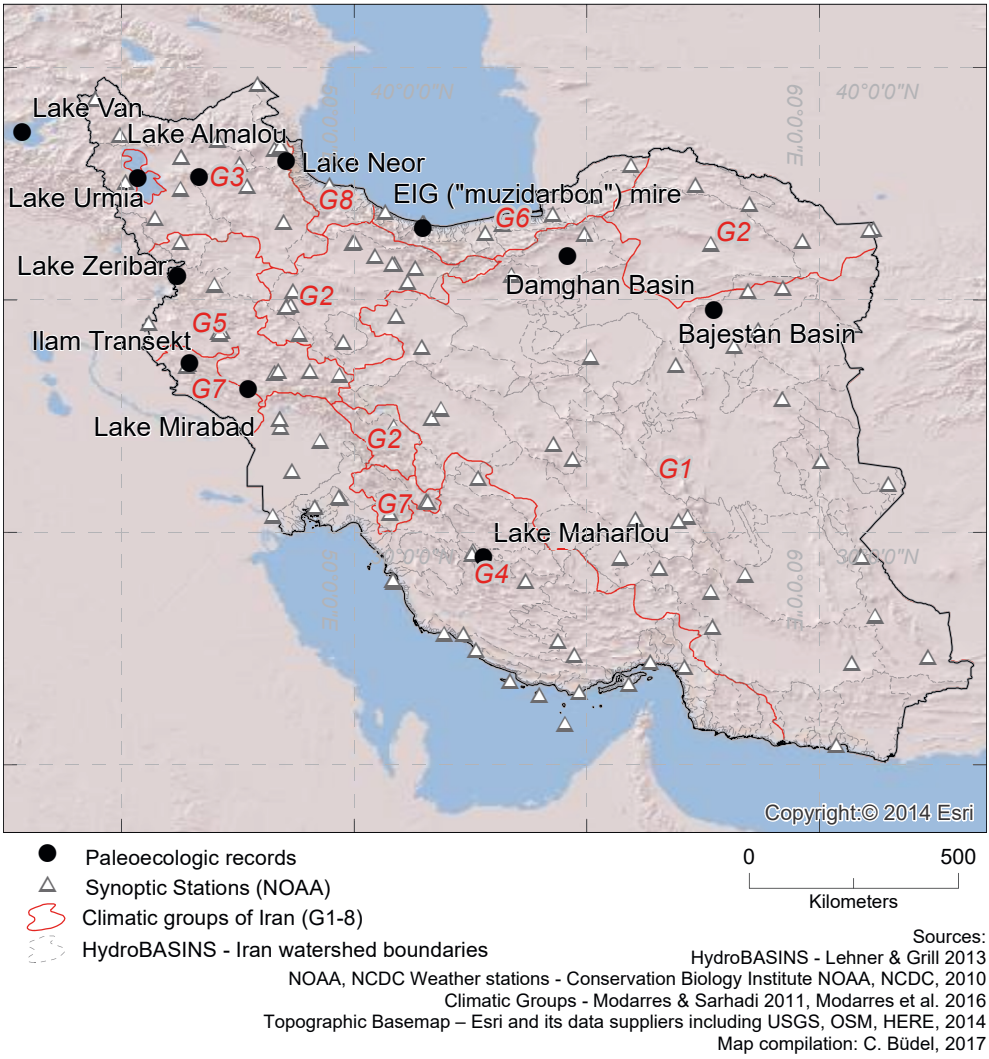

two major drought events between 9-4 ka. They alternate with stable conditions in between, followed by prevailing drier conditions up to present times (Wasylikowa et al. 2006; Stevens et al. 2006). The last climatic changes which controlled landscape development in a global scale, and that had also been measured in sediments from Iran was the Medieval Climate Anomaly (MCA) and Little Ice Age (LIA) (cf. Ramezani et al. 2008; Finné et al. 2011).

Figure 1.2.4: Indications of past periods of varying humidity as derived from lake sediments in Northwestern Iran and Southeast Turkey. A pronounced late Pleistocene to early Holocene decrease in humidity can be observed in the long-time archives of Lake Zeribar and Lake Van between 10 500 – 12 800 years ago. A second drought is interpreted from the sediments of the Lakes Van, Urmia, Neor and Zeribar. The pronounced decrease of humidity dates between ~ 9 000 and 10 000 years ago. While Lake Mirabad is not significant during this two events, it's sediments, together with others, reveal a depression in humidity from 7 000 to 5 000 years ago and supposedly in subsequence to MCA and LIA.
References: Wick et al. 2003, Çağatay et al. 2014 – Lake Van; Bottema 1986 – Lake Urmia; Wasylikowa et al. 2006, Djamali et al. 2009a – Lake Almalou; Sharifi et al. 2015 – Lake Neor; Djamali et al. 2008 – Lake Zeribar; Griffiths et al. 2001, Stevens et al. 2006 – Lake Mirabad; Djamali et al. 2009b – Lake Maharlou; Lisiecki & Raymo 2005 – Benthic $\delta^{18}O$.

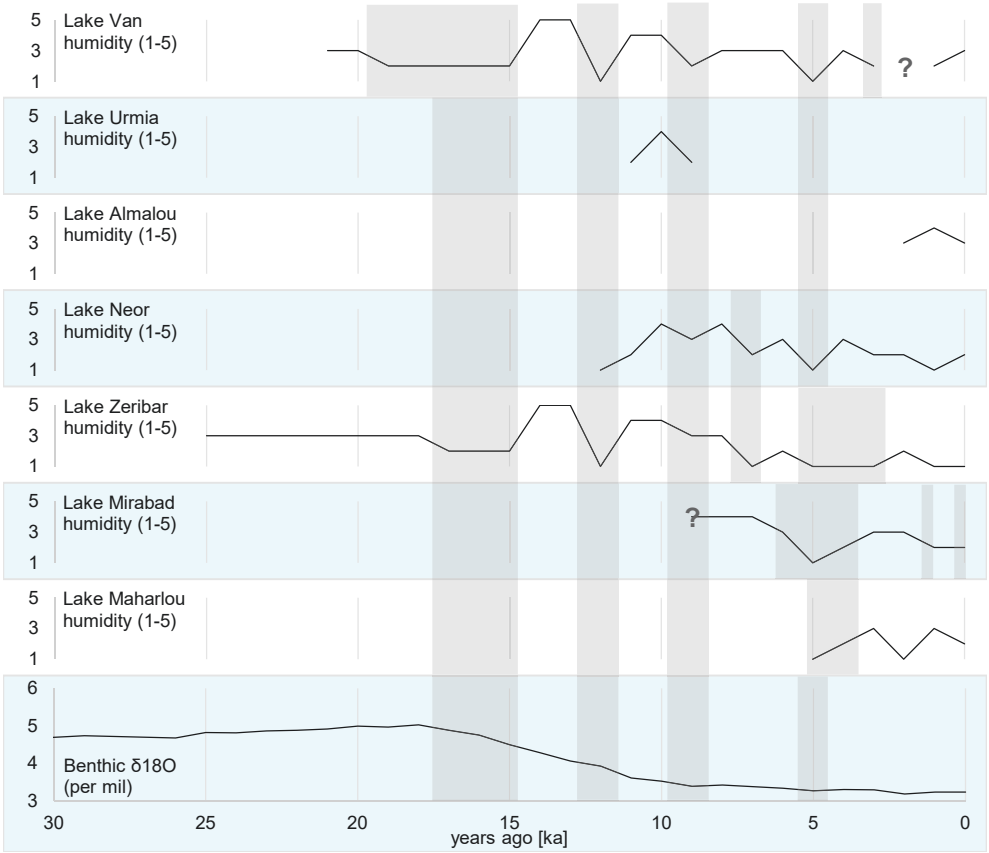

Source: Own illustration

Together with the frequently altered pattern of climate zones, lake levels adapted to the variable humidity in Iran (Fig. 1.2.4). A first post-Pleistocene severe drought coincident with a significant lake level retreat has been correlated to the Younger Dryas Event. This period lasted from maximal 12 800 years ago on to at least 10 500 years ago, with a significant shift in general climatic conditions, as was derived from palaeoecological multi-proxy analysis from Lake Van and Lake Zeribar (Wasylikowa et al. 2006; Wick et al. 2003; Çağatay et al. 2014). A second pronounced lake level retreat can be inferred from the lake sediments as perceived in the studies about Lake

Urmia (north-west Iran; Bottema 1986), Lake Zeribar (west Iran; Wasylikowa et al. 2006) and Lake Van (south-east Turkey; Çağatay et al. 2014). Lake level retreat is measured with an onset at about 9 900 - 9 800 cal. yr. BP for Lake Urmia and Lake Van, and at least 7 800 cal. yr. BP at Lake Zeribar. Also Walker & Fattahi (2011) infer from datings of eastern Iranian alluvial fan abandonments, river terracing and lake deposition a synthesis of lake level high stands in Iran up to ~9 000 and ~7 000 years ago. The character and impact of the third drought event varies considerably and its signal is indistinct. A pronounced lake level fall was dated between 4 500 - 3 800 cal. yr. BP at Lake Zeribar (Wasylikowa et al. 2006) and peripheral desiccation with gypsum precipitation was dated between 6 505 - 4 048 cal. yr. BP at Lake Mirabad (Griffiths et al. 2001). Also at Lake Van dry conditions were identified using mulit-proxy analysis and were dated to 5 400 and 3 800 cal, yr. BP (Çağatay et al. 2014). Detailed evidence for youngest droughts were inferred from $\delta^{18}O$-peaks from ostracods in Lake Mirabad sediments and were dated to 1 500 and 500 cal. yr. BP, and thus they are correlating with MCA and LIA (Stevens et al. 2006).

1.3 Regional Setting and study sites

1.3.1 Damghan Basin

The investigation area covers the central part of Damghan Basin and incorporates all landforms of a typical basin and range sequence. The cities Semnan and Shahroud in the northeastern part of Iran mark the lateral extent of the basin while

Picture 1.3.1: View to northern Alborz slope from south of the young alluvial fans S03-B. The fine sediments terrace clearly divides older from younger fan generations (Picture: C. Büdel, 2010).

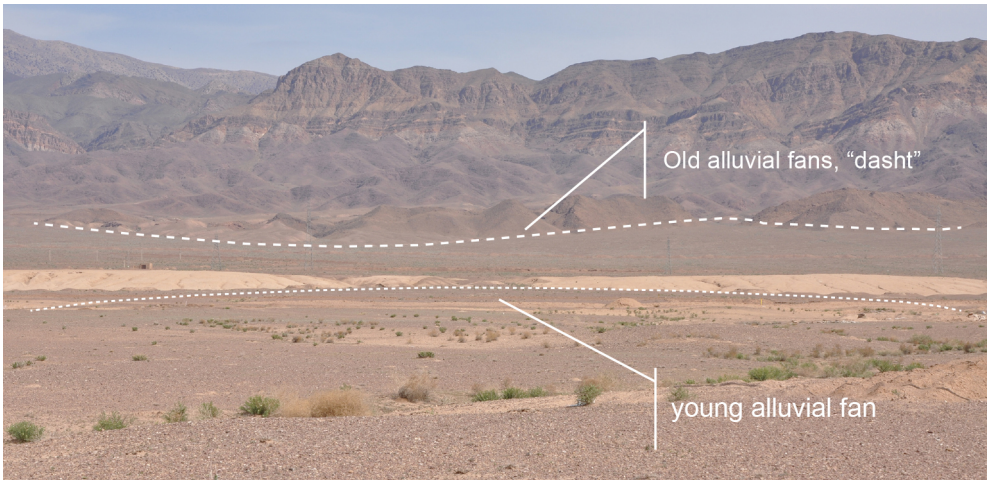

Source: Own photograph

Figure 1.3.1: (A) The overview shows a Landsat 8 scene which reveals main landscapes of the basin. The alluvial apron sample sites including the coring site B04-A within the Playa are also shown. (B) The same scene in large scale shows the alluvial apron with the playa lake sediment line and the sections.

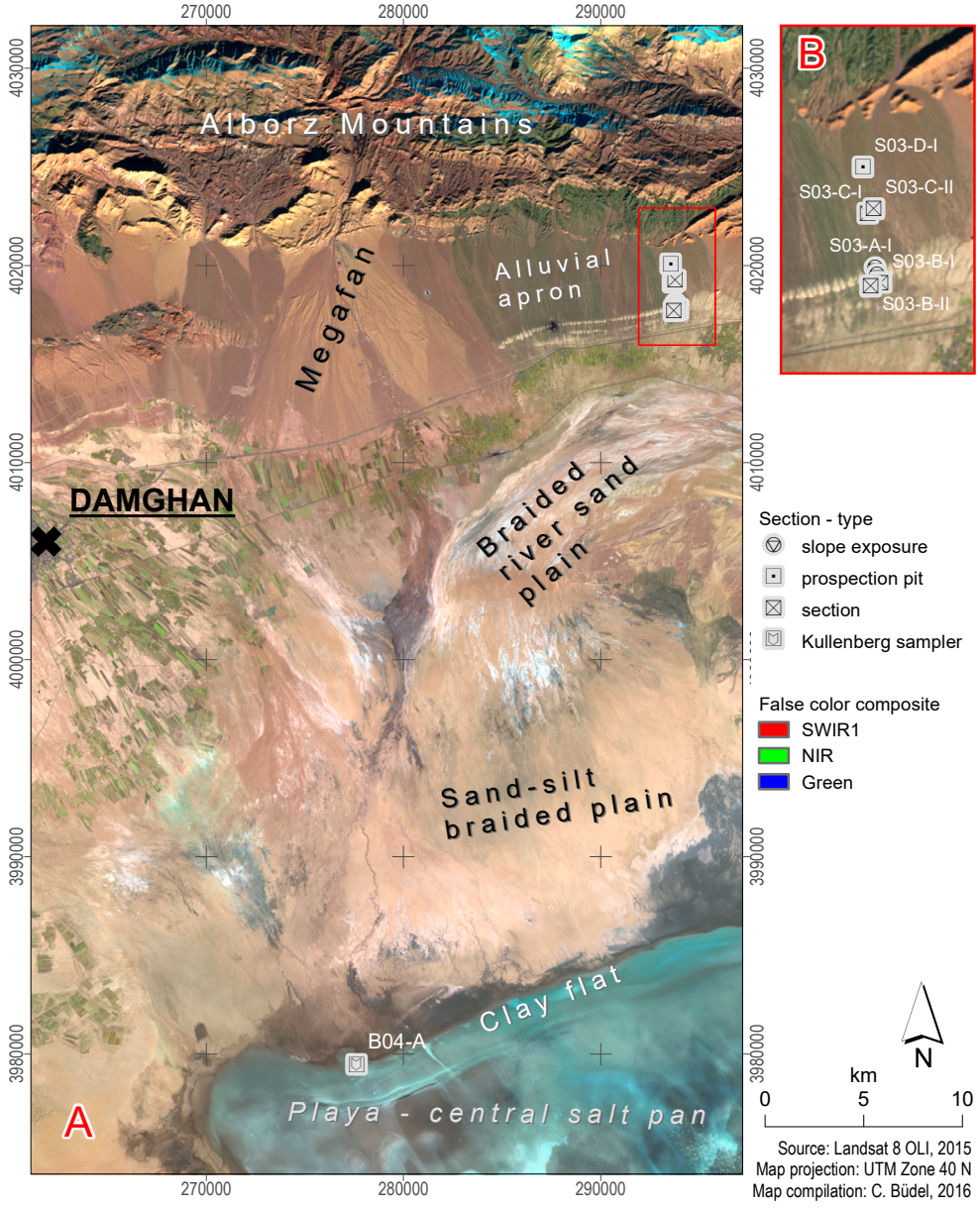

the Alborz Mountains limit its northern range. The mountains are stepwise sloping down southwards to the basin of the Great Kavir and the Damghan Basin forms a step at an altitude of about 1 050 m a.s.l. The central depression, which is also called Kavir "Haj Aligholi" or "Chah-e-Jam" (eng. "Damghan Kavir"), forms the final part of a local basin and range sequence and is occupied by a vast playa saltpan. The saltpan is surrounded by a clayflat with wet and dry zonation, where groundwater variability and pouring controls the periodically varying extent of the wet clay flat zone. With a sharp border it changes to a vast sand-silt braided plain where the ephemeral streams from the mountain ranges terminate periodically or episodically. Valley slopes are flanking the streams where these are passing mountainous area or have incised alluvial fans. The alluvial fans cover footslopes and plains and form generations of alluvial aprons with different age and elevation (Pic. 1.3.1). The braided river plains are linking sediment transport from alluvial aprons and footslopes to the central sink of the playa (cf. Fig. 1.3.1).

Where quaternary sediments are not covering the older rock formations, these are prone to weathering (cf. chap 3.1.2; Appendix II). The predominant rock formations are of Cambrian to Devonian origin all over the smaller and closer watersheds of the alluvial apron at Alborz Mountain's southern slopes. These formations were quickly eroded and form inner-mountainous basins alongside the major synclinal structures, which are dividing Central Alborz into roughly east west striking units. Thereby, the big watersheds of the central Alborz mainly incorporate Triassic-Jurassic rocks of Shemshak and Lar formation.

As observed in the field, fluvial and alluvial, and to a minor part aeolian surface materials of the quaternary units bear soils with a varying degree of development. This degree commonly coincides with the regional climatic gradients of the basin. Typical calcisols, frequently with argillic horizon and gligai-structure predominantly cover the sand-silt braided plain. Foremost in the southern part of the basin where mean temperature is higher and evaporation is more intense Solonchaks widely replace the Calcisols. In these areas, surface run-off and periodically occurring water concentration in riverbeds and channels alter the soil development to Regosol and Fluvisol. While the moderate tilting of alluvial fans and aprons preferably conducts the development of desert pavements, younger alluvial fan surfaces show Leptosols, with poorly weathered gravels. Longer exposure time, increased precipitation and higher moisture in soils of older fan surfaces and also in the valleys of the Alborz Mountains enables the development of Cambisols or well developed Fluvisols (all descriptions according to FAO 2012).

The basins local climate shows a substantial north-south gradient (Hijmans et al. 2005; Fig 1.3.2). The mean annual precipitation decreases from its maximum of about 400 mm at the peaks of the Alborz Mountains to 61 mm in the lowlands. The central Kavir receives even less rainfall throughout the year. Cyclones from northwestern directions are blocked by the Alborz Mountains. This causes a lee-ward position effect in Damghan Basin and explains the gradient of local climate. An abrupt decrease of precipitation from 150 mm in the space of the northern footslopes at height of the City of Damghan to 61 mm south from this line (Krinsley 1970).

Figure 1.3.2: The climate gradient in Damghan Basin is a lee-ward-effect of the Alborz Mountains (Data: WorldClim, Hijmans et al. 2005; Hillshade: ASTER GDEM).

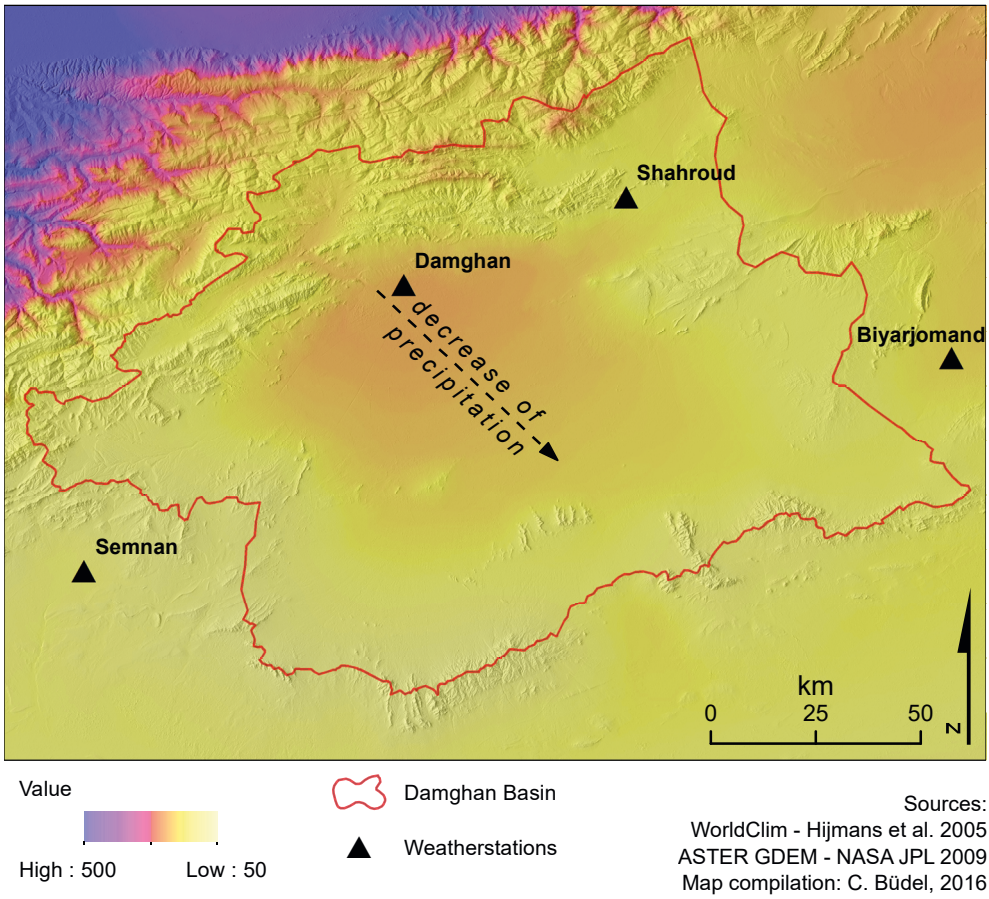

Most recent measurements meanwhile show generally higher rainfall in a wider space from the City of Damghan (Hijmans et al. 2005; Fig. 1.3.3). Observational data from local weather stations (I.R. of Iran Meteorological Organization (IRIMO) 2015) show a trend for higher mean annual temperatures since the documentation started. This development is complemented by decreasing rates of precipitation since about 1990, which leads to intensified aridity in the region and high surface run-off with a risk of sheet-floods and debris flows, reworking older surfaces. This recent observation is the continuation of a changeable weather development during the youngest climatic period, with overall increasing aridity remarkably disturbed by Medieval Climate Anomaly (MCA) and Little Ice Age (LIA) (cf. Ramezani et al. 2008; Finné et al. 2011).

Figure 1.3.3: Monthly averages and annual trends calculated from observational data (2002-2014) from Damghan City weather station represent the typical winter rainfalls and the summer temperature maximum and show their specific values at this locality.

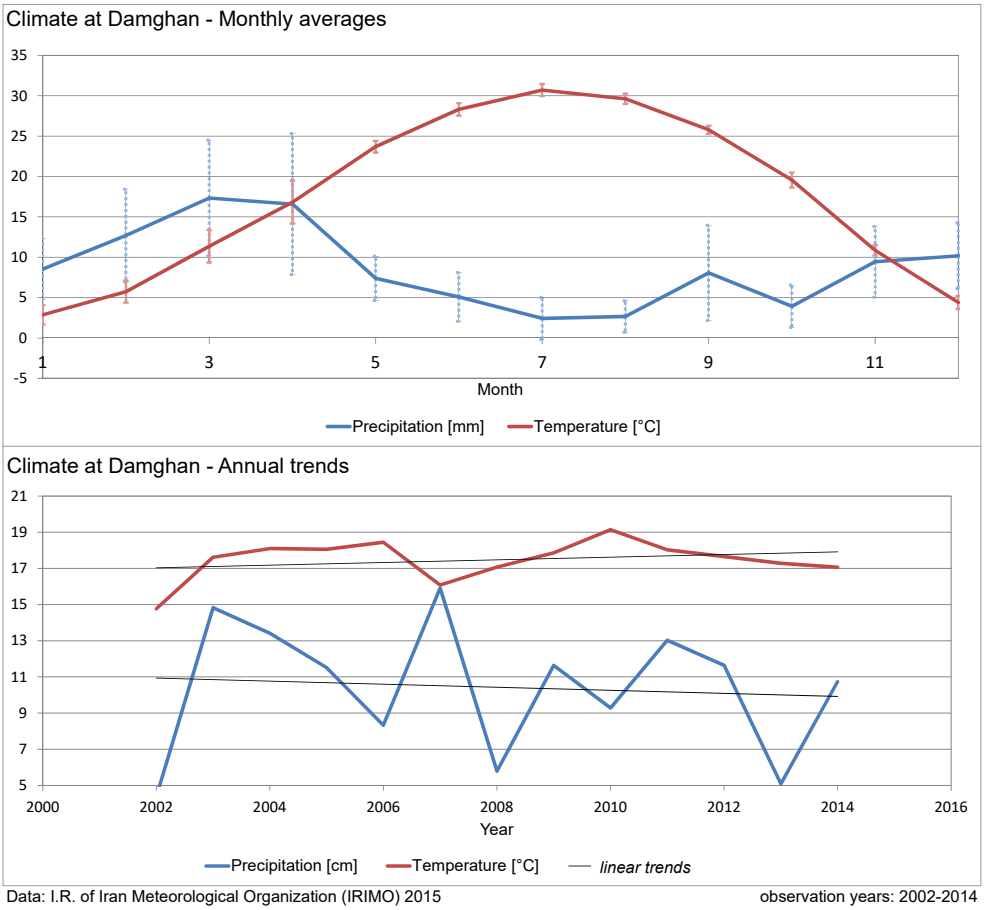

Data: I.R. of Iran Meteorological Organization (IRIMO) 2015 observation years: 2002-2014

Source: Own illustration

Hollingsworth et al. (2010) recently studied the tectonic activity within the basin. They focused on the neotectonic activity of the important Damghan Fault. This left-lateral fault is part of the Astaneh Fault system and cuts the northern alluvial fans and aprons in the study area. Its last known major activity may have been the catastrophic Qumis Earthquake in 856 A.D., since when the risk for a new earthquake has increased rapidly (Hollingsworth et al. 2010). Therefore the study also discussed methods for monitoring the fault's activity.

1.3.2 Study Sites

The Study sites are located on representative sediment surfaces of alluvial, fluvial and lacustrine genesis (Fig. 1.3.1.). These sediments are connected through a sed-

iment cascade from the Alborz Mountain's footslope, through the alluvial aprons and fluvial plains, and finally down to the central sink in the playa. The course of the sediments defines a transect which was designated for detailed geomorphological mapping, in an agreement with the Geological Survey of Iran. The observed landforms within the transect were considered to provide good representativity for the dominant basin wide geomorphology and quaternary geology. Three intercalating alluvial fans of the alluvial apron were subdivided to proximal, medial and distal reaches. This supported systematic ground truth fieldwork and the identification of key surfaces and sediments of the local geomorphological system. The smaller fans along Alborz Mountain's footslope form an alluvial apron and prograde 3-4 km towards the basin center. Megafans, each with 15-16 km mean diameter are flanking the apron at each side. In the proximal reaches of the alluvial apron, the fan heads open through narrow outlets into their watersheds. The watersheds, which connect the mountain ranges with the sediments of the study sites cover an area of 11.4 km². The rock formations within this sediment source area incorporate Cambrian, Ordovician and Devonian, quartz sandstones or sandstones and dolomites or limestones, with slates, marls and shale (Tab. 1.3.1).

Table 1.3.1: Coverage of the 11.4 km² large catchment, lithology, and age of geological formations within the combined watersheds of the investigated alluvial apron sequence; mapped from Landsat 7 ETM Multispectral scenes and the 1:100 000 Geological Map (Vaziri & Majidifard 2000, Aghanabati 1994, Aghanabati 2004).

Area	Unit - Formation	Lithology	Age
38 %	$€_l$ - Lalun Formation	Purple quartz sandstone with slate	Lower/Early Cambrian
20 %	$€_{m2-5}$ - Mila Formation	Dark grey dolomite, yellow shale and marl	Upper/Late Cambrian
13 %	$€_{bt}$ - Barut Formation	Alternation of cherty dolomite, limestone and slate	Lower/Early Cambrian
11 %	$€_z$ - Zagun Formation	Alternations of purple quartz sandstone and slate	Lower/Early Cambrian
9 %	$€_{m1}$ - Mila Formation	White, thick bedded quartzite and sandstone	Middle Cambrian
4 %	O1 - Lashkarak Formation	Sandstones and shales	Lower/Early Ordovician
2 %	$€_s$ - Soltanieh Formation	Light, massive cherty dolomite and shale, with stromatolite	Lower/Early Cambrian
1 %	Dj_3 - Jirud Formation	Limestones and shales	Upper/Late Devonian

Source: Own table

In its distal reaches, deposits of the alluvial apron interleave with the fine sediments of an elongated terrace-shaped landform. Krinsley (1970) defined this as a remnant of a former undated lake level high stand. Today, this supposed lake or playa silts and sands are deeply incised, and at least two generations of young, small alluvial fans (about 300-400 m mean diameter) accumulated and now cover the older alluvium directly below the terrace. The supposed playa sediments as well as the young alluvial fan generations were also designated for sample sites. In their vicinity, the footslope runs out into the sandy-silty floodplain of the Shahrud River. This is a periodically draining river, which passes the eastern mega fan and alluvial apron and

connects them with the sediment basin of the central playa over a distance of today 30 kilometers. The central playa divides into an unregularly shaped, dry mud flat with an extent of 800 to 2 500 m, a wide (> 4 000 m) saline clay flat and finally the central salt crust. This study site is highly affected by the salt dynamics of periodical flooding and subsequent desiccation and thus, active geomorphological processes and structures, such as salt crusting and efflorescence soil cover occupy huge areas. Due to limited access on the muddy surface, only the salt crust was selected as a site for detailed studies.

2 Material and Methods

2.1 Geomorphological mapping and remote sensing

The completion of the Quaternary stratigraphy of the investigation area was one of the primary goals of the mapping project. Therefore, new map units were invented, that could describe the quaternary stratigraphy and which followed the map unit standards of Geological Survey of Iran (GSI). Moreover, a geomorphological base-map was demanded, which is capable for distinguishing morphometric properties and morphogenesis of the Quaternary map units.

For Damghan Basin, it was found that several geoscientific mapping projects were accomplished, before. Scientist from the GSI prepared the geological maps 1 : 100 000 "Shahrud" (Vaziri & Majidifard 2000), and 1 : 250 000 "Gorgan" (Shahrabi 1991). These maps provide basic data about the general geological setting of the study area. In addition, Hollingsworth et al. (2010) and Rizza et al. (2011) studied the tectonic activity of the Astaneh Fault and also incorporated some geological mapping, recently.

The optimal integration of established expert knowledge with modern remote sensing data and powerful software tools within a Geographic Information System (GIS), as it was discussed by Gustavsson et al. (2006; 2008), is the fundamental requirement of the mapping system in this study. Both, pre-existing geological maps from GSI, as well as the detailed geomorphological mapping, conducted within this project, provides the required expert knowledge. A geomorphological-analytical geodatabase structure enables the optimal integration of our expert knowledge with topographic base data, remote sensing data and GIS-tools for data exploration. Comparable software mapping environments were developed and tested, e.g. by Gustavsson and Seijmonsbergen in Sweden and Austria (Gustavsson & Kolstrup 2009; Seijmonsbergen 2013).

2.1.1 Geomorphological database and mapping standards

The Geographic Information System was developed for storing and operating feature classes and symbol standards of the German GMK25 detailed geomorphologic mapping system (latest version "GMK5" in Leser, Stäblein 1985). The GMK25 system perfectly provides the basic structure for a geomorphological geodatabase due to its inherent layer structure and the coded symbol categories. Furthermore, it allows for the successful integration of map features from older analog maps for wider application (cf. Gustavsson et al. 2008). Overall, it provides principals for a geodatabase design including the functionality of describing and storing data on geomorphologic system element classes in the three essential categories: form, material and process (Fig. 2.1.1). Consequently, relationships between geomorphic system elements could directly be implemented in the geodatabase using reliable standard GIS tools for describing relationship classes and topology rules. Hence, the

geodatabase enabled investigating map unit characteristics and relationships with geoprocessing tools from SAGA GIS and ArcGIS (ESRI) software and evaluating stratigraphic information for the mapped sediment units and their stratigraphic or sequence-stratigraphic order.

The database is separated into two base-data geodatabases containing (1) the base imagery (e.g. remote sensing imagery) and (2) processed base data in raster and vector file format (e.g. land surface parameters). A third, operational mapping, geodatabase incorporates (3) structure and concepts of the mapping project and stores all mapped features in vector file format (e.g. valley polylines). The vector features are classified and stored according to the standard categorization of geomorphological system elements into form, material and processes. Accordingly, feature classes for geomorphological system synthesis were implemented (Fig. 2.1.1):

- morphometry & morphography (form)
- morphostructure (material)
- morphodynamics & morphogenesis (process)
- geomorphology (system synthesis)

The feature geometries are employed in the geodatabases vector files and depend on the geometry of the landforms, or map unit they describe (cf. Leser & Stäblein 1985; Tab. 2.1.1).

Table 2.1.1: Overview of main data entries stored in the mapping projects geodatabase.

Geometry	Coded Values (selection)	Category
Empiric data (monochrome)		
Point	Singular / minor landforms / roughness	Morphometry & Morphography
Polyline	Steps / curvature / valleys / linear structures	Morphometry & Morphography
Polygon	Areas of minor landforms and roughness	Morphometry & Morphography
Annotation	Strike / dip / bedding	Geomorphostructure
Polyline	Contacts / key beds / faults	Geomorphostructure
Polygon	Material / rocks	Geomorphostructure
Point	Traces of processes	Morphodynamics & Morphogenesis
Polyline	Lines of processes	Morphodynamics & Morphogenesis
Polygon	Areas of processes	Morphodynamics & Morphogenesis
Interpretation (colored)		
Annotation	Interpretative Annotations	Geomorphology
Polyline	System contacts / changes of process / structure	Geomorphology
Polygon	Areas of process and structure	Geomorphology

Source: Own table

There are also external folders included for the data import, exchange and external processing, as well as for data outputs and map layout projects, including all necessary layer files for map symbology standards. The symbology and color expression of geological and geomorphological classes follows GMK5-legend standards (Leser & Stäblein 1985).

The mapping standards are correspondingly described in the domain archive database, which is a collection of tables storing the coded values of all map elements. These coded database entries are taken from mapping standards for geomorphological and geological classification as provided in Leser & Stäblein 1985, Ad-Hoc-Arbeitsgruppe Geologie 2002, Federal Geographic Data Committee 2006, and USGS

Table 2.1.2: Coded values for new geomorphological classes, which were added to the GMK5-legend standard values.

Feature Class	Vector Type	Code	Description
System Contacts; Changes of process/structure	polyline	1317	system contact / change of process & structure
System Contacts; Changes of process/structure	polyline	13171	system contact - location accurate
System Contacts; Changes of process/structure	polyline	13172	system contact - location approximate
System Contacts; Changes of process/structure	polyline	13173	system contact - location inferred
System Contacts; Changes of process/structure	polyline	13174	system contact - location concealed
System Contacts; Changes of process/structure	polyline	13175	gradational system contact
System Contacts; Changes of process/structure	polyline	13176	gradational system contact, inferred
System Contacts; Changes of process/structure	polyline	13177	change of process - location accurate
System Contacts; Changes of process/structure	polyline	13178	change of process - location approximate
System Contacts; Changes of process/structure	polyline	13179	change of process - location inferred
System Contacts; Changes of process/structure	polyline	13180	change of process - location concealed
System Contacts; Changes of process/structure	polyline	13181	gradational change of process
System Contacts; Changes of process/structure	polyline	13182	gradational change of process, inferred
System Contacts; Changes of process/structure	polyline	13183	change of structure - location accurate
System Contacts; Changes of process/structure	polyline	13184	change of structure - location approximate
System Contacts; Changes of process/structure	polyline	13185	change of structure - location inferred
System Contacts; Changes of process/structure	polyline	13186	change of structure - location concealed
System Contacts; Changes of process/structure	polyline	13187	gradational change of structure
System Contacts; Changes of process/structure	polyline	13188	gradational change of structure, inferred
Area of process and structure	polygon	13815	fluvial, area of Holocene alluvial fan activity and alluvial plains
Substrate / Lithology	polygon	8125	desert pavement
Areas of Process	polygon	12191	formation of evaporates

Source: Own table

National Cooperative Geologic Mapping Program (NCGMP) 2011. In addition to and based on these standards new values for geomorphological classification were developed to allow an analytical combination of geological and geomorphological map units and to enhance the map expression (Tab. 2.1.2).

Attribute standards for geomorphological classification and map unit description were also defined in the domain archive; here, string based coded values determine geological and geomorphological properties (Fig. 2.1.1). The properties for map unit description defined in the domains read as follows:

- *Actuality:* This quality allows the assumption of simple age constellations of geomorphic phenomena within recent to fossil ages. Such rough estimations can already be made in the field, e.g. when studying known formations with connected landforms, and they are important for the initital organization of geomorphologic observations. It is not an additional indicator for activity, that is conventionally symbolized in the color code of morphodynamic feature classes (red = active / black = inactive, cf. Leser & Stäblein 1985). However, it has proven to be useful also for geomorphological risk assessment (cf. Schneevoigt et al. 2008).

- *Confidence:* This is an established property of map elements in geological maps (cf. Ad-Hoc-Arbeitsgruppe Geologie 2002, Federal Geographic Data Committee 2006) but has yet not been introduced in geomorphological maps. The distinction of empiric fact and interpretational feature of geomorphological maps is intensively discussed, and an additional indication of confidence and un-confidence of interpretational evidence within geomorphological maps has been demanded (Jansen 2007).

- *Temporal and spatial variability:* Recent landforms are quickly reshaping and transforming, due to ongoing morphological processes. Therefore, a distinction can be made, between formative and non-formative events, which occur within the specific landform (Brunsden 2006). Direction, frequency and magnitude of formative events are crucial for the interpretation of the landform genesis. An estimation of temporal and spatial continuity or variability of landforms is also an integral quality of several thematic maps, or e.g. hydro-geographic map elements in conventional topographic maps. The temporal and spatial variability was therefore integrated in the geomorphological map unit description (cf. Brunsden 1993; Brunsden 1996).

- *Unconformity:* This is the strongest and most descriptive stratigraphic evidence for morphogenetic and lithologic (dis-)continuity and standard in stratigraphic description (cf. Ad-Hoc-Arbeitsgruppe Geologie 2002; Nichols 2009).

- *Sediment budget and type of erosion:* Geomorphological map systems frequently pronounce hydrographic features, for the purpose of better orientation, as well as for the important description of water distribution as the primary medium of landform shaping. Moreover, classes of sediment budget and erosional fea-

tures are valuable for sediment body's, which are constituting the landscape and were integrated into the mapping system (cf. Demek & Gellert 1976; Leser et al. 1975).

Figure 2.1.1: The geodatabase concept of the Quaternary mapping project in Damghan, comprises the domain archive and the three central geodatabases. Two geodatabases for raster and vector base and process datasets, and one for the actual vector mapping content. Reference in the scheme to be read as follows: * Leser & Stäblein 1985, ** Ad-Hoc-Arbeitsgruppe Geologie 2002, Federal Geographic Data Committee 2006, *** USGS National Cooperative Geologic Mapping Program (NCGMP) 2011.

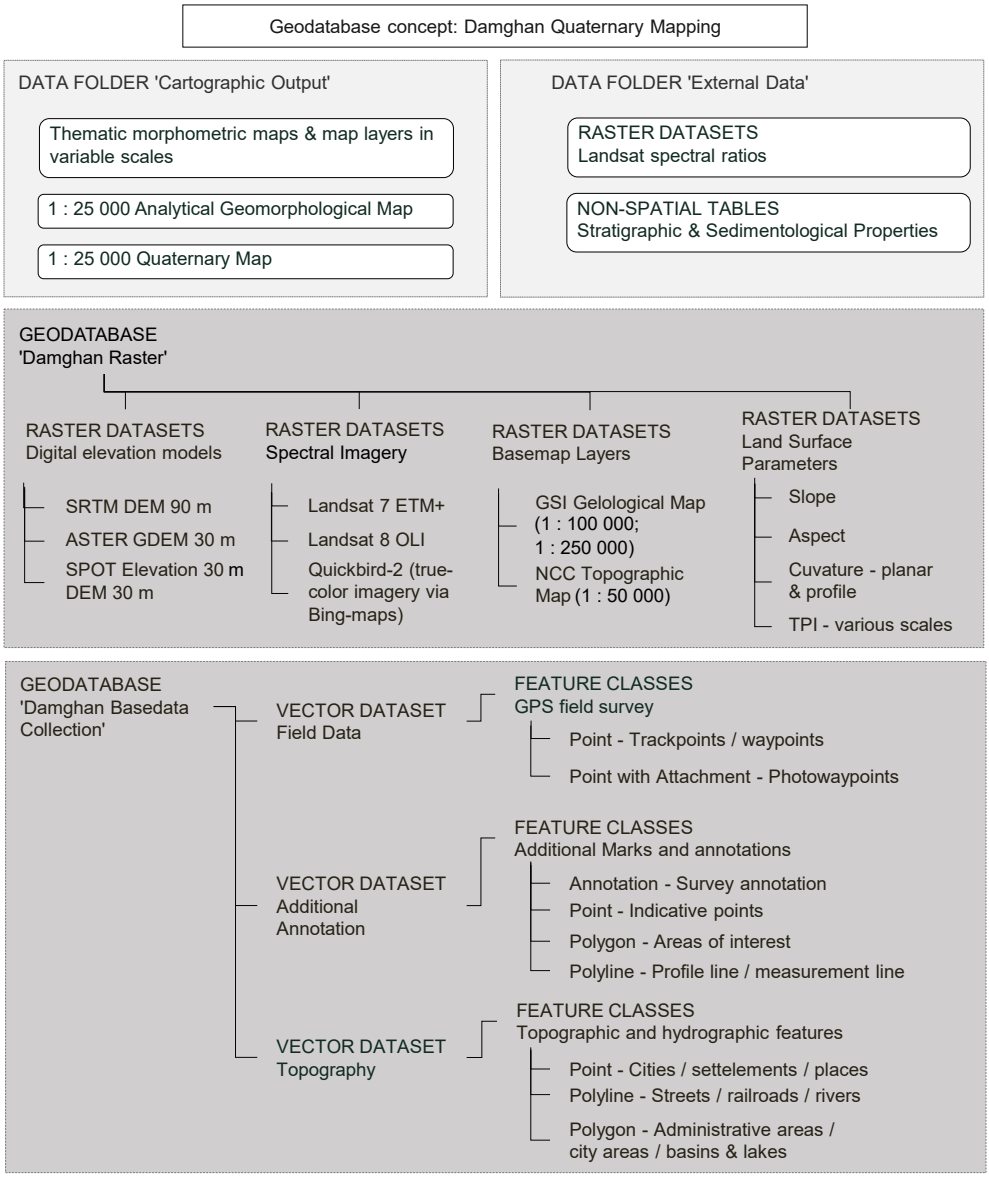

Continuation of Figure 2.1.1

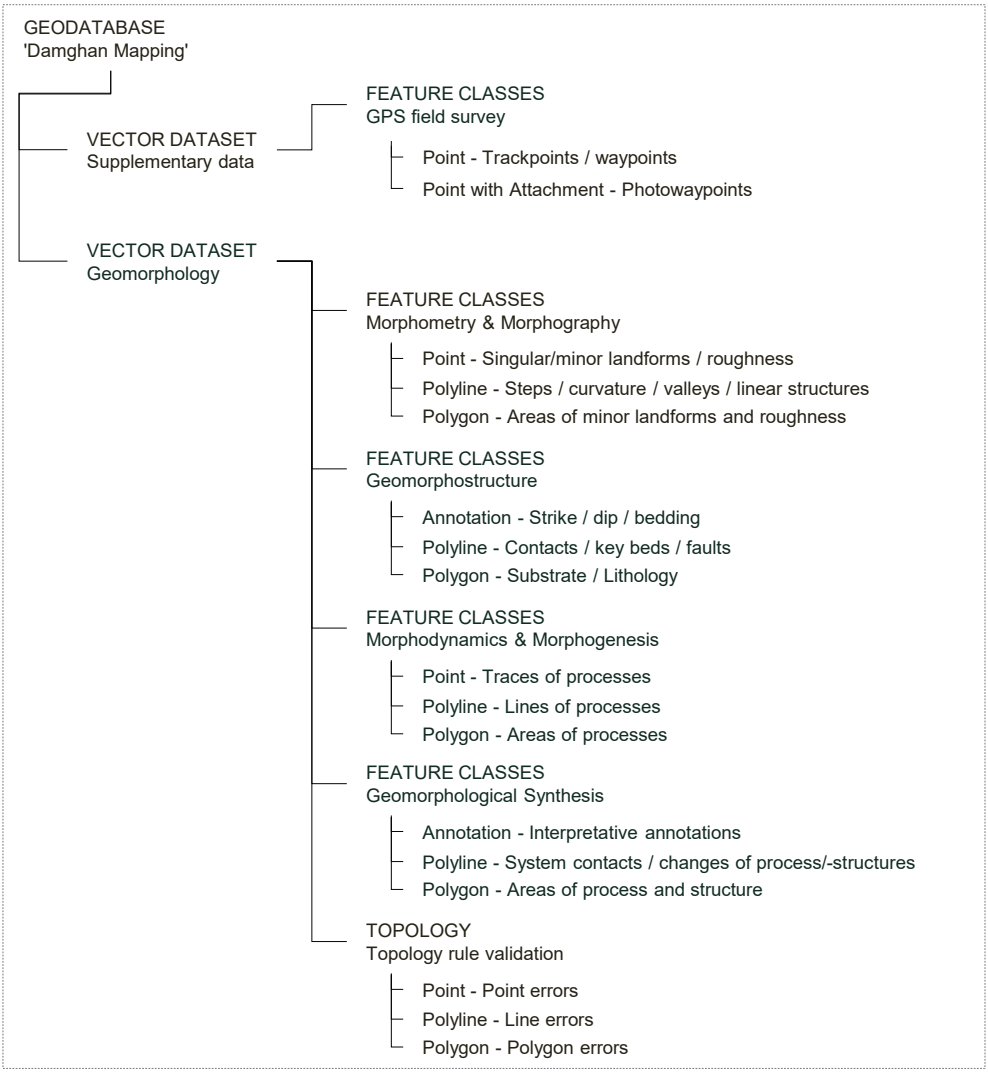

2.1.2 Base data and data analyses

The basemaps, used for the general mapping were Geological maps from GSI in scale 1 : 250 000 and 1 : 100 000. In addition, the standard 1 : 50 000 topographic maps from the Surficial Survey of Iran (NCC) were applied. The vectorising of quaternary surfaces was preferably based on spectral ratios and indices, derived from remote sensing images. These values were calculated from Landsat 7 ETM+ scenes, Landsat 8 OLI archives and Quickbird-2 true-color composites (Tab. 2.1.3; Fig. 2.1.2). The spectral indices were interpreted as signals of their near subsurface material components and hence gave an estimation of the representability of sample data

Continuation of Figure 2.1.1

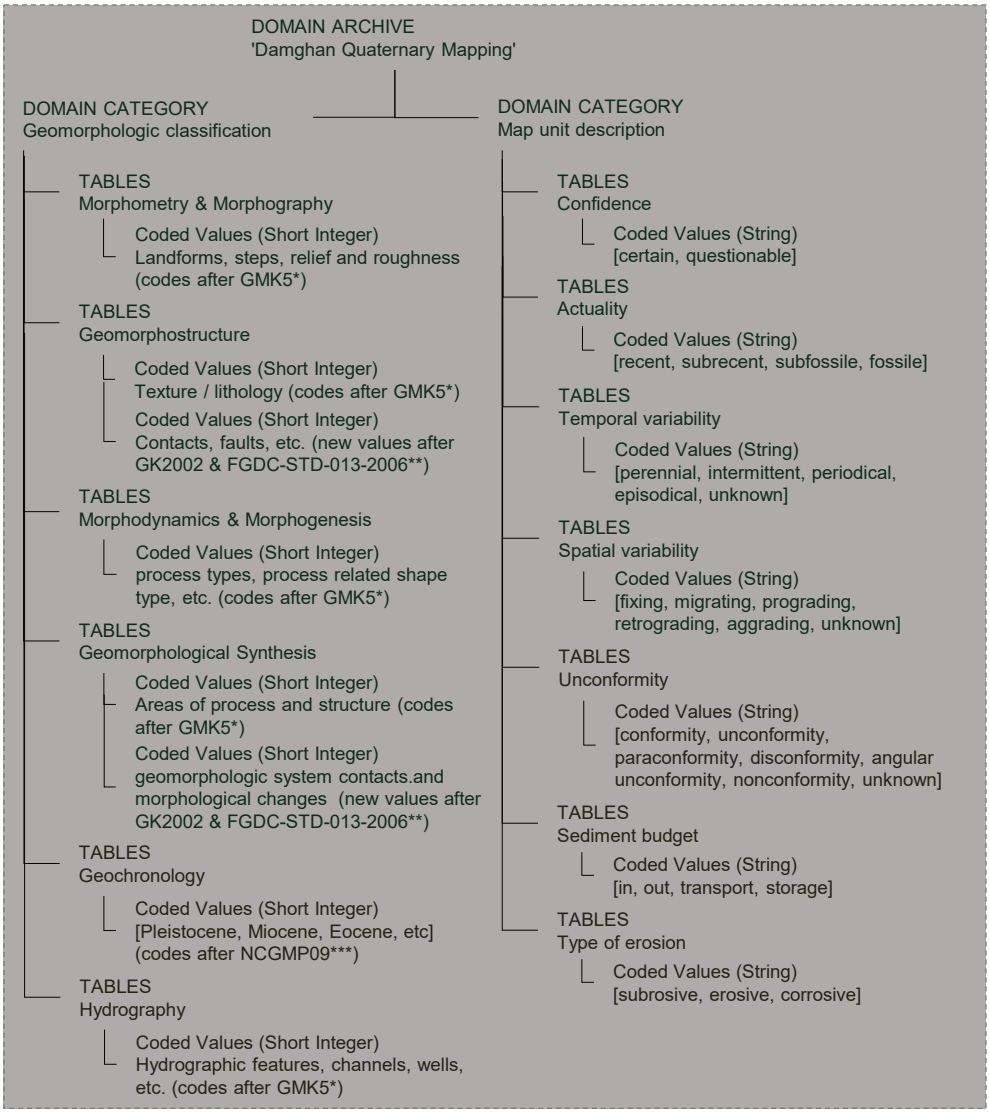

Source: Own illustration

from the particular sections. The spectral data from Landsat 7 imagery helped to better distinguish different ages and provenance of alluvial sediments and surfaces, although it was not suitable for mapping morphometric features.

The meso- and macroscale geomorphologic assessment was performed on morphometric derivates of ASTER GDEM and SRTM DEM and, for more precise measurements, a SPOT Elevation 30 DEM was processed (Tab. 2.1.2). The SRTM digital elevation model, which was developed by CGIAR-CSI, is based on version 1 of the original SRTM DEM. Its data voids were filled by the use of special multiple

Table 2.1.3: Overview of remote sensing data used in the project.

Mission	Resolution (panchromatic)	Acquisition / Version	Bands	Source
SRTM DEM	90 m / 3 arc-seconds	02/2000 (NASA V3, CGIAR-CSI V4)	-	NASA JPL 2013 Reuter et al. 2007
ASTER GDEM	30 m / 1 arc-second	2000-2008 (V1) 2000-2010 (V2)	-	NASA JPL 2009
SPOT Elevation 30	20 m	n.a.	-	Airbus Defence and Space 2005
Landsat 7 ETM+	30 (15) m	03-04/2010	0.450 – 0.515 µm (blue) 0.525 – 0.605 µm (green) 0.630 – 0.690 µm (red) 0.775 – 0.900 µm (NIR) 1.550 – 1.750 µm (SWIR 1) 2.090 – 2.350 µm (SWIR 2)	NASA Goddard Space Flight Centre 2016
Landsat 8 OLI	30 (15) m	01-08/2015	0.433 – 0.453 µm (aerosol) 0.450 – 0.515 µm (blue) 0.525 – 0.600 µm (green) 0.630 – 0.680 µm (red) 0.845 – 0.885 µm (NIR) 1.560 – 1.660 µm (SWIR 1) 2.100 – 2.300 µm (SWIR 2)	U.S. Geological Survey 2016
Quickbird-2 Color (via Bing-Maps)	2.4 (0.6) m	10/2011 - Bing-Maps Access	0.430 – 0.545 µm (blue) 0.466 – 0.620 µm (green) 0.590 – 0.710 µm (red)	USGS National Cooperative Geologic Mapping Program (NCGMP) 2011

Source: Own table

interpolation methods (Reuter et al. 2007). The most recent SRTM DEM (NASA version 3) was available later in course of the project and provided void filling by use of ASTER GDEM V2 transfer data (NASA JPL 2013). Accordingly, this data source is not independent of ASTER GDEM, which is of importance when evaluating land surface parameters (LSP, cf. Olaya 2009) calculated from both datasets. The ASTER GDEM and the SRTM DEM both show rough surfaces in flat areas, like it is the case within most of the Damghan Basin landscapes, and therefore both reveal high uncertainties on according landforms. In order to improve the quality of the DEM modelling an additional digital elevation model was acquired from Airbus Defence and Space. The received Elevation 30 DEM is primarily based on stereoscopic DEM extraction from SPOT imagery Airbus Defence and Space 2005. The main morphometric mapping and processing was done using this data, because of its slightly higher resolution (20 meter) and the good relative vertical precision regarding local relief changes.

Spectral data processing

In Damghan area spectral properties were analyzed before by Ehsani and Alavi Panah using Landsat 7 ETM+ data (2002, in Alavi Panah et al. 2008). They applied an Optimum Index Factor (OIF) to color composites of the Damghan Playa and they found that, for discriminating salt crusts and silty clayey soils, the color composite of ETM+ bands 6-4-2 in RGB performs best (Alavi Panah et al. 2008). The shortwave-infrared (SWIR 1 & 2: 1.55 - 1.75 μm & 2.09 - 2.35 μm) and near-infrared (NIR: 0.76 - 0.9 μm) bands were sensitive for lithological changes (cf. Demek 1982; Busche & Siefker 2004; Robinson et al. 2007) and provided specific differentiation of alluvial surfaces, as quantified with Landsat 8 OLI data in Figure 3.2.5. The Landsat 8 OLI spectra of red (Red: 0.64 - 0.67), green (Green: 0.53 - 0.59) and blue (Blue: 0.45 - 0.51) visible light were used to derive a proxy for soil salinity. The mineral ratios were calculated in ENVI 5.2 and ArcGIS 10.2 using the Landsat 8 OLI-sensor band-combinations. Previously, the data was prepared applying the radiometric calibration in ENVI. Here, the top of atmosphere reflectance (TOA) and the spectral radiance was calculated using the ENVI 5.2 standard tools. All necessary parameters were provided by the Landsat 8 OLI metadata file (MTL-file). This radiometric calibration transforms the digital numbers of the OLI L1 product file into the physical data of spectral radiance and top of atmosphere reflectance. The transformation is done, by correcting the digital numbers with individual light-diffraction and shifting values of the sensor bands, as documented in the MTL-file (U.S. Geological Survey 2016).

The following spectral ratios were calculated and used in the project:

$$(1) \qquad \text{Clay Minerals Ratio} = \frac{\text{SWIR 1}}{\text{SWIR 2}}$$

The clay minerals ratio is used as a proxy for surface weathering (Drury 2001). The reflection at clay-minerals rich sediments and rocks highly affects this ratio. Areas, that are covered by homogenous bedrock, rich in feldspar and mica, are particularly suitable for detecting surfaces with high rates of clay mineral growth and weathering (Okrusch & Matthes 2010).

$$(2) \qquad \text{Ferrous Minerals Ratio} = \frac{\text{SWIR 1}}{\text{NIR}}$$

The ferrous minerals ratio described by Drury (2001) provides sensitivity for iron content in minerals. This relationship is particularly suited to distinguish alluvial fans by means of base rock variability within their individual watersheds. This requires a varying amount of iron-bearing minerals, which optimally affects the SWIR 1 / NIR quotient. This facilitates the reliable delineation of distinct alluvial fans within a *bahada*, or as part of an alluvial apron in a geomorphological map. Of further importance is the higher content of iron bearing minerals in increasingly weathered sediments, which can affect the ferrous minerals ratio. In this context, hematite and goethite can be regarded as major index minerals for weathering activity (Scheffer et al. 2010).

$$(3) \qquad \text{Salinity Indes} = \frac{\text{Red} \times \text{Green}}{\text{Blue}}$$

The index quotation (3) was used as a proxy for soil salinity (Abbas & Khan 2007). It sets the Blue-value, which showed sensitivity to the soil salinity in comparable studies from Iran and Pakistan (Abbas & Khan 2007; Taghizadeh Mehrjardi et al. 2008), in ratio to the product of Red and Green values. The square root of the product of Red and Green values was first successfully applied as a salinity index by Douaoui et al. 2006 and is also used in recent studies (Allbed & Kumar 2013; Azabdaftari & Sunar 2016). Douaoui et al. observed that in areas with high levels of surface salt, the salinity is considerably underestimated, but shows gut correlation to field measurements.

All ratios are difficult to be interpreted (Drury 2001), due to the chaotic and disturbed reflectance from desert pavements. The ratios are part of the spectral enhancement in the mapping concept (Fig. 2.1.2)

Processing of digital elevation models (DEM)

The DEM data was filtered using the standard lowpass filter of ESRI ArcGIS and an advanced Non-local means filter from Ullmann (c.f. Ullmann 2015; Ullmann et al. 2017), which is an adapted filtering, better capable of preserving relief structures. Small depressions or sinks occurred with high frequency in the investigated digital elevation models, due to signal noise and errors in measurements, primarily in slightly tilted and flat smooth areas (slope: < 6°). All DEM data was filtered and subsequently processed, using data fill-routines from ArcGIS toolboxes, in order to enable proper geomorphologic and hydromorphic modeling.

The land-surfaces parameters were then calculated using SAGA GIS and ArcGIS geoprocessing tools. The derivate processing included the calculation of the following parameters (cf. Olaya 2009):

- Local parameters: *slope, aspect, curvature, hillshade, hypsometric areas/lines*
- Regional parameters: *Topographic Position Index (TPI) of variable sizes*
- Regional hydrographic parameters: *watersheds, streams*

The geomorphological features were analyzed and extracted manually, based on the LSPs. An operative mapping scale of 1 : 10 000 was set, and all landforms with a spatial extent > 100 m were dissolved (according GMK5-legend standards in Leser & Stäblein 1985). The slope areas were classified according to the slope classes of GMK5. The planar curvature thresholds for ridges and other exposed linear landforms were determined using a threshold of 0.6 and by synoptic correlation with spectral data. Only linear landforms were mapped in contrast to the traditional representation of curvature lines within the GMK5-legend. This explicitly excludes curvature lines within smooth, continuous landforms like slopes, which were criticized as a misleading element of geomorphological maps (cf. commentary by Leser in Jansen 2007).

The TPI based classification of Weiss (Fattahi et al. 2006; Reu et al. 2013) was applied for a better understanding of the landscapes morphometry. The approach classifies discrete slope positions derived from the standard deviation of topographic position indices from a large and a small observation window. These processing identifies geomorphological changes based on the relief variability automatically and guides the detailed manual mapping. In addition, it provides better integrity of geomorphometric map elements.

The described DEM investigations are represented in the morphometric assessment and the map element vectorization in the mapping concept (Fig. 2.1.2).

Field mapping, data analysis and ground truth field work

The analysis and interpretation of system contacts and of geomorphic systems, leads to a valid determination of areas of geomorphological process and structure. It must be the result of data exploration and conclusion and synthesis of all mapping efforts. The mapping in this project integrated the already described processing of geomorphological and geological variables; these were vectorized and classified in advance, and validated and supplemented later in the field (Fig. 2.1.2: field mapping).

It is of importance to identify and describe formative events and processes, which predominantly shaped the landform. Therefore, the fieldwork included the investigation of near sub-surface stratigraphic properties, e.g. structure and texture, color and lithology (Chap. 2.2.2). Together with the in-situ measurements of morphologic landform properties, this systematic approach ensured a complete acquisition of stratigraphic and morphologic evidence. The initially developed geodatabase also provides all required mapping and symbology standards for the field mapping (Chap. 2.1.1). All geomorphologic and stratigraphic properties are described according to specific geomorphological mapping system standards (Stäblein 1978; Leser & Stäblein 1985) and to international standards (Demek & Gellert 1976; Leser 1977; Stow 2008; Lisle et al. 2011; Tucker 2011). The organization and strategy of mapping fieldwork considered limited area access and outcrop availability. Hence, check points for ground truth field work and mapping traverses were selected close to roads and smooth alluvial fan and terrace ridges, suitable for driving. In addition, geologic and geomorphologic exposures were selected for individual mapping operations (Demek & Gellert 1976; Lisle et al. 2011).

Figure 2.1.2: The concept chart of geomorphological mapping and multi-method GIS analysis, as it was applied in the Damghan mapping project. The implementation of adequate scale properties and valuable cartographic restrictions are of paramount importance for all input parameters and data processing outputs. The topological evaluation of map elements assesses map element properties and relationships.

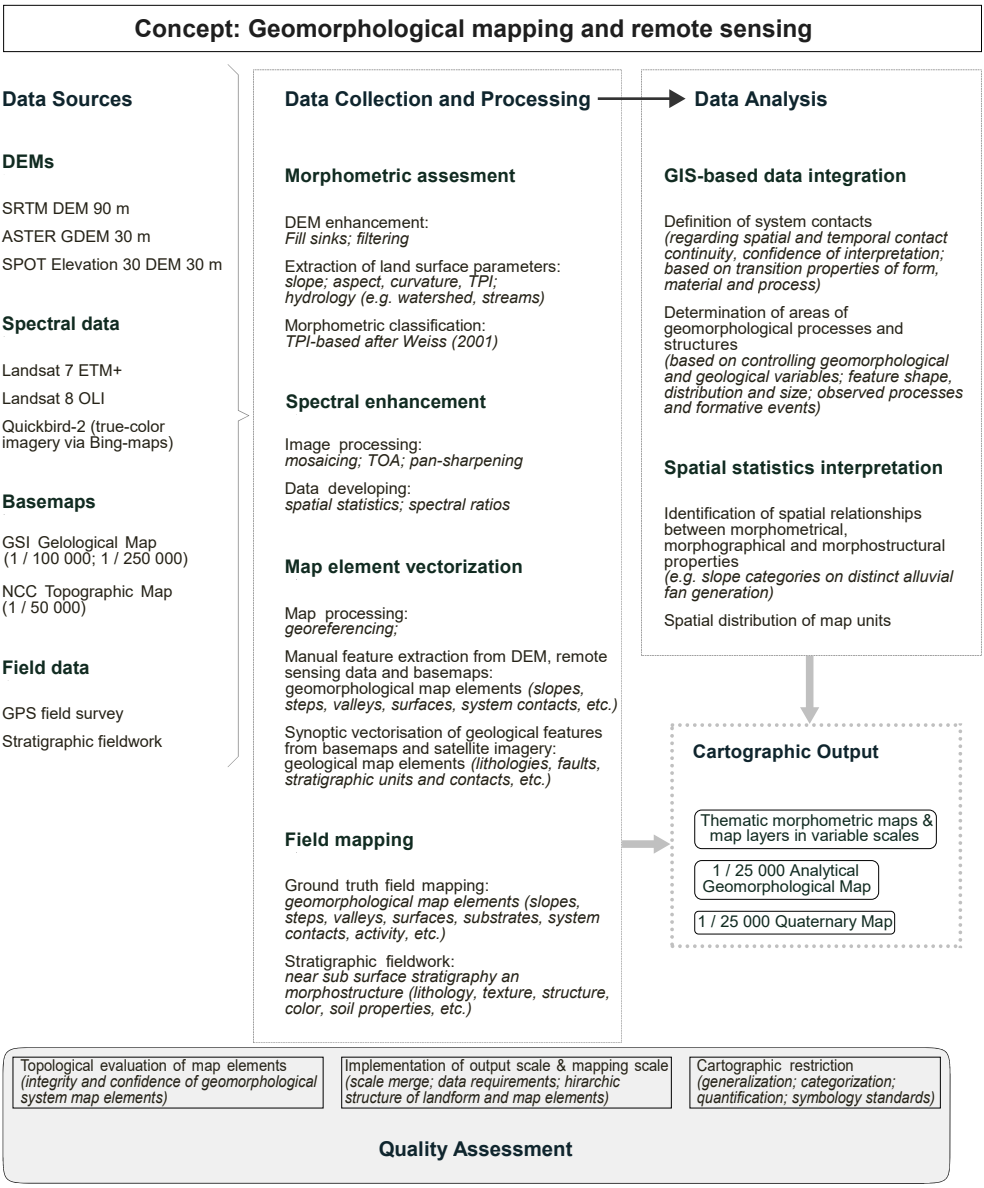

Source: Own illustration

The ground truth field work was conducted along with in-situ measurements of morphologic features and stratigraphic properties in 56 days, during several field campaigns from November 2009 to November 2012.

For the definition and determination of system contacts and areas of process and structure, all data from digital data processing and field mapping is imported to feature classes and non-spatial tables, as provided by the GIS-environment. Also laboratory data (Chap. 2.3) and sediment ages (Chap. 2.4) were joined for validating specific theories. The confidence of interpretational map elements was primarily estimated for areas of process and structure.

2.2 Specific mapping and stratigraphic field work

2.2.1 Ground penetrating radar survey

For getting a first idea of subsurface layering measurements with Ground Penetrating Radar (GPR) was carried out. The information about vertical and lateral expansion of the sediments, as well as magnitude and frequency of their related geomorphologic events, should also be gained.

The GPR was applied because of its good performance during measurements on alluvial cones and debris cones in the Alps (e.g. Schrott & Sass 2008) and due to the general advantage of its extended reach and fast measuring rates – even in quaternary sediments (Smith & Jol 1995). The system uses the specific dielectric attributes of underground materials by actively emitting electromagnetic beams into the ground and measuring the expansion time through the alternating layers from emitting to receiving antenna. The vertical resolution and the measurement depth are depending on the antenna frequency and the relative permittivity of the passed material (Milsom 2003; Jol 2009).

The material properties must be well-known for the conversion of measured travel times to absolute depth values. The specific values controlling travel times are the relative permittivity ε_r and the electric conductivity (σ Sm^{-1} – unit: Siemens / meter). The relative permittivity is expressed as the ratio between the material specific permittivity and the permittivity of vacuum (4).

$$\text{relative Permitivity } [\varepsilon_r] = \frac{\text{material Permitivity } [\varepsilon]}{\text{vacuum Permitivity } [\varepsilon_0]} \quad (4)$$

Therefore, a GPR signal from fine sediments (e.g. lacustrine deposits) will strongly be affected and largely absorbed by high water and clay contents. In quaternary sediments antenna frequency and signal penetration depth will be straight proportional and a 50-MHz-antenna can penetrate the sediments to nearly 50 m, if there are optimal conditions present (Smith & Jol 1995; Milsom 2003).

Sites for GPR measurements had been selected regarding the geomorphologic system of the alluvial apron. Therefore, the entire sediment cascade from the fan-head at the mountain range down to the fan-toe and flood plains transition could be

Figure 2.2.1: (A) Ground penetrating radar survey was carried out on proximal, medial and distal sections of the alluvial apron. (B) Overview of the situation of the alluvial apron.

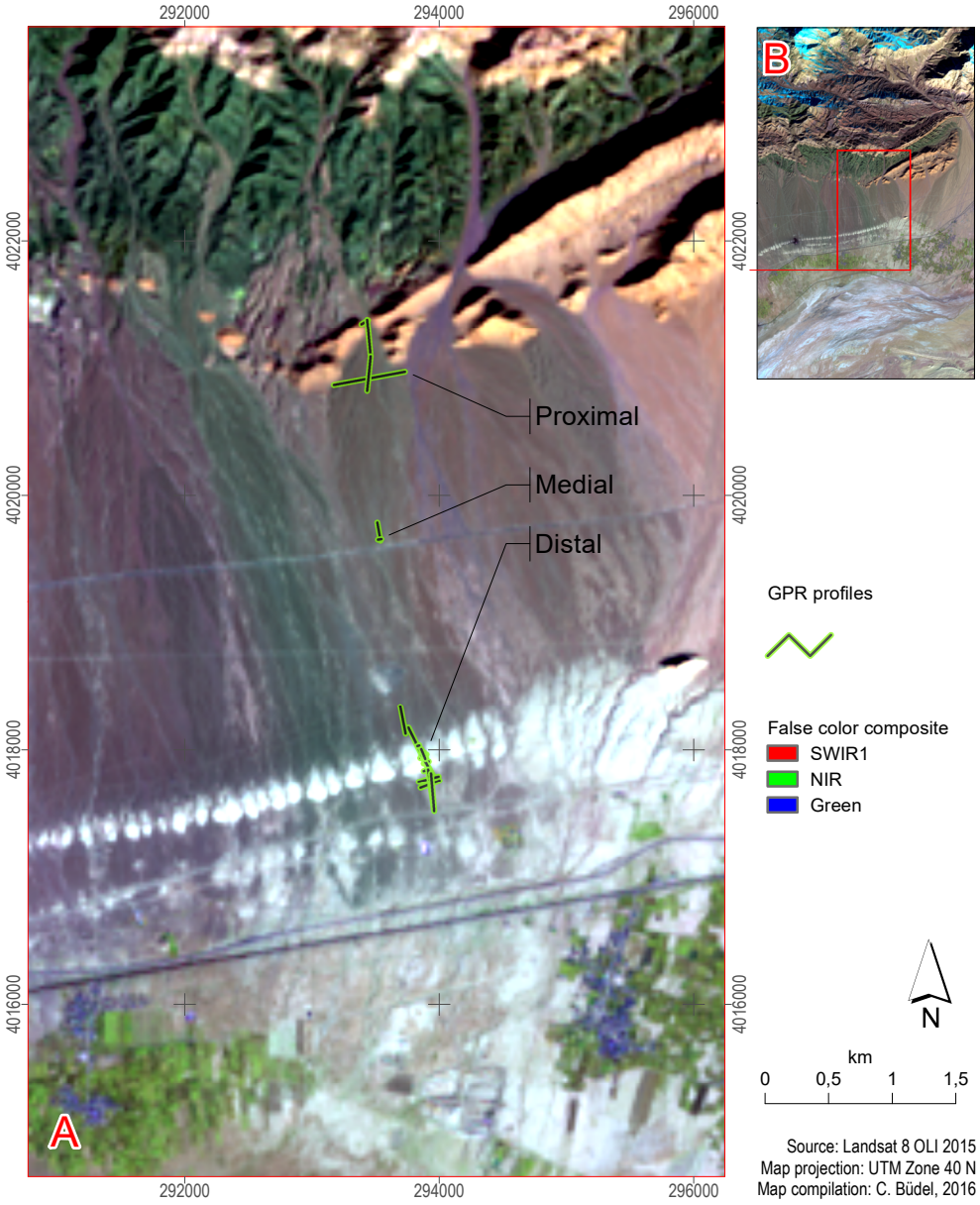

investigated within significant geomorphologic areas. Te measurements were done at three sites in proximal, medial and distal sections of the apron (Fig. 2.2.1).

Over 100 measurements in a standard common-offset, single fold configuration (Jol 2009) were conducted during six days in the year 2010, without any complica-

tion, for instance due to whether or system failure. Antennas used had fixed frequencies of 25, 50, 100, 200 and 250 MHz and two of the high frequency antennas provided shielding equipment for preventing from ray disturbances. All antennas and the processing unit are part of Geosystems Malâ Ramac GPR and were provided by GSI.

The main use was made of the 50-MHz-antenna due to the aim of detecting major changes in depositional milieu, plus eventually measuring the transition to bedrock. Additional measurements with 100, 200 and 250-MHz-antenna had been performed, in order to identify changes in near surface layering at the fine-sediment outcrop at Damghan Fault.

The profile lines and according relief information were marked and measured manually in the field.

The post processing was standardized for all measurements with one individual antenna-frequency. The calculation and the filtering was performed using ReflexW v4.5 software (K. J. Sandmeier 1998-2007). The following set of filters provided comprehensive results together with a good comparability and was applied to all datasets:

1. Move starttime
2. Energy decay
3. Subtract-DC-shift
4. *Subtract mean (dewow)*
5. *Gain function*
6. Background removal
7. *Topographic migration*
8. Correct 3D-topography

Filters in *cursive* letters were only applied if necessary.

2.2.2 Stratigraphic field work and section analysis

For the completion of the mapping fieldwork (Chap. 2.1.2) the main quaternary surfaces were selected (Fig.1.3.1; Fig. 3.2.6). Here, representative and detailed study sections were prepared and detailed investigations on slope exposures and trenches took place. The analysis includes a documentation by photographs, sketches and field description, and the field classification of stratigraphic units. The field description comprises established methods for analyzing pedogenetic features and sedimentary structures, texture classes, lithology, color (Munsell Color 2009), bio- and hydromorphic features and evaporation for every single sediment and soil unit (Ad-hoc-AG Boden 2005; FAO 2006; Stow 2008). Subsequently, the soil characteristics were interpreted and classified in terms of international standards (IUSS Working Group WRB 2007; IUSS Working Group WRB 2015).

The core sampling was carried out using a modified, manually driven Kullenberg piston core sampler. The piston technique makes this device suitable for sam-

pling undisturbed cores in wet sediments, using a vacuum effect for trapping the sediments within a PVC liner tube (PVC = polyvinyl chloride). Therefore, in one single sampling action, the device captures ramming cores with a length of up to two meters and a diameter of 63 mm. Two primary locations for core sampling were determined, depending on the accessibility and on the expected sediment thickness. The best access was provided from southwest, where the province road 81 passes and a gravel road to the playa branches off. A gravel dam was constructed for previous exploration drillings, which starts at the location where the gravel road approaches the playa. It enables vehicles to securely cross the wet clay flat and pass on to the solid salt crust and the dam could still be used during this project. Krinsley (1970) already found that the playa surface is tilted to southwest, from 1 094 to 1 050 m a.s.l. and with an inclination of about 2 m / km. Therefore, the maximum sediment thickness is supposed to be located in the southwestern margins of the playa. Nevertheless, the primarily designated site for core sampling was not the central playa. This is due to the prevailing conditions of maximal evaporation and salt-dynamics, leading to massive salts, impenetrably for both: allochthonous sediments and specialized core samplers. Thus, the sampling sites were placed at the northern and southern margin of the central playa salt crust (Fig. 3.3.2). This decision also facilitates a comparison of two different cores, with systematically diverging sediment origins and properties.

All cores were stored in their PVC liner tubes and sent to Germany for laboratory analysis. A working half and an archive half was determined, when splitting the core into two halves in the laboratory. The working half provides the sediments for sampling, for the preparation of thin sections and for detailed description, while the archive half is reserved for scanning and non-invasive methods and for archiving. The archive cores were scanned with a multi-sensor core logger (Geotek MSCL-XZ) at the Institute of Geology and Mineralogy at the University of Cologne. The MSCL-scans provide high resolution line-scan imagery (Geotek GEOSCAN IV 3 x 2048 CCD line-scan camera, with standard Nikon lens mount) with calibrated quantifiable RGB-images. The calibration was performed in the factory, as well as in the laboratory using a standard photographic 18 % grey card. Additionally, a vacuum X-ray fluorescence spectrometer (Innov-X Alpha XRF) provided semi-quantitative measurements of detectable elements (Ca, Ti, Cr, Mn, Fe, Co, Ni, Cu, Zn, As, Se, Rb, Sr, Mo, Ag, Cd, Sn, Sb, Ba, Hg, Pb) with a scanning interval of 5 mm. The device was calibrated in the factory, and for standardization a reference peace of stainless steel is used (cf. Rothwell & Rack 2006).

The initial core description (ICD) and sampling of the working cores took place at the Institute of Geographical Sciences at the Freie Universität Berlin and complies established standards stratigraphic core description and core logging (cf. Kamp et al. 2001; Schnurrenberger et al. 2003). The core description includes the compilation of a detailed section of the cores and core layers (core log), which already assigns the macroscopic physical and chemical layer properties – e.g. distribution of key elements like Fe and Ca, color spectra, and indicators for soil development.

2.3 Analyzing geophysical and geochemical properties

The sampling of the alluvial sections followed the geometry of the individual layers. An equidistant sampling in 20 cm steps was carried out, where no layering was noticeable. The sampling of the cores implemented a 10 cm equidistant dimension, with additional sampling, where the layering featured apparent structures. All samples were prepared for archiving, laboratory analyzes (overview in Tab. 2.3.1) and dating (Chap. 2.4).

The initial treatment for all sample was air dry sieving to < 1 mm and < 2 mm and the separation of representative aliquots. A number of aliquots was weighed, homogenized and ground with a vibrating achat cup mill and the gravimetric water content was measured after the drying of aliquots at 105 °C. The measurements of pH-value and electric conductivity, as well as the granulometric analyses required air-dried, un-ground aliquots. For the analysis of easily soluble salt contents, pH-values, and for aqueous extraction of salts measured with ion-chromatography, these aliquots were agitated in corresponding amounts of distilled water (*aqua dest.*) (Blume et al. 2010). In order to determine the mineral composition, measurements with an X-ray powder diffraction (XRD) analyzer (RIGAKU Miniflex 600) were performed on air-dried but ground aliquots.

A Beckmann-Coulter LS13320 PIDS laser diffraction particle size analyzer was used for the determination of grain sizes between <1 mm and >0.04 µm (cf. Stanley-Wood 2005). To reduce coagulation of the particles for the laser-measurements, all aliquots were washed, and 100 ml of bi-distilled water was added. Due to the lack of organic material within the samples, treatment with H_2O_2 was omitted. Allochthonous carbonates presumably constitute a high amount of total detritus in the investigated sediments and therefore an HCl-solution of inorganic carbonates was not intended, in order to preserve the more important allochthonous carbonate content. Hence, a treatment with 0.5 g $Na_4P_2O_7$ (sodium diphosphate) was applied and a 5 min ultrasonic bath directly before the measurement prevented the particles from coagulation. The optical model used in this study for calculating the grainsize distribution is based on the Fraunhofer diffraction theory (FD). This theory describes the diffraction caused by the interaction of light and, in comparison to the wavelength, relative large particles. For the measurement of sediments of predominant small grain sizes, the Lorenz-Mie theory (Mie) should be preferred. This theory better describes the particle-light-interactions of relative small particles (de Boer et al. 1987). Due to the small geometry of clay particles, Mie and FD both have problems when measuring clays. While Mie considers several variables, FD needs less information about optical properties of the grains. Therefore, FD more reliably measures non-spherical – consequently diffracting – clay particles from clay minerals (Kerry et al. 2009; Park et al. 2014). All calculations for statistical grain size parameters were performed using the GRADISTAT software package (Blott & Pye 2001), and they are based solely on the grain sizes derived from the laser-measurements.

The analyses of major and minor element content required acidic dilution and ground and oven dried (105 °C) powdered samples.

The acid dilution was performed using *aqua regia* extraction and a standardized microwave heating sequence (for details see Vogel et al. 2015: Supplementary data). Subsequently, major elements (Ca, Fe, K, Mg, Mn, Na, P, S, Sr) and minor elements (Cd, Cr, Cu, Pb, Ni, and Zn) were determined with an inductively coupled plasma optical emission spectrometer (ICP-OES Perkin Elmer Optima 2100DV) on the base of DIN EN 13346 (Anonymous, 2001). The certified reference material (LGC6156) was used for quality control and to calibrate the element signal values.

For a quantitative determination of Al, Si and Ti the oven dried (105 °C) and powdered samples were measured with a portable energy-dispersive X-ray fluorescence (p-ED-XRF) analyzer (Thermo Scientific NITON XL3t). The calibration data for p-ED-XRF analysis was provided by frequent quality control measurements of certified materials from standard reference no. NCS DC 73387 and NCS DC 73389 with recovery values of 102-112 % (Al_2O_3), 100-104 % (SiO_2), and 98-105 % (Ti).

Also the total inorganic carbon (TIC) was determined using a Woesthoff Carmhograph C16 analyzer by solubilizing carbon with hot phosphoric acid (H_3PO_4). The subsequent fixation of the evolved CO_2 was attained in 1 mol NaOH solution and the quantification was done by measuring the conductivity. All measurements were calibrated with a calcite standard ($CaCO_3$ 12.01 ± 0.14 %; RSD < 2 %). A LECO TrueSpec Macro CHN+S Analyzer was used to determine total carbon (TC), total nitrogen (TN) and sulfur contents.

Table 2.3.1: List of applied laboratory analysis.

Parameter	Method	Reference
Grain-size determination (> 2mm; < 2mm to > 1 mm)	Manually operated sieving	(Blume et al. 2005)
Grain-size determination (< 1mm to > 0.04 µm)	Beckmann-Coulter LS13320 PIDS laser diffraction particle size analyzer	(Stanley-Wood 2005)
Electric conductivity	10 g of soil in 25 ml bi-destilled water	(Blume et al. 2005)
pH	10 g of soil in 25 ml bi-destilled water	DIN ISO 10390 (2005); (Vogel et al. 2015)
TC, TN, (TOC)	Combustion with subsequent IR-detection; LECO TruSpec CHN	(Blume et al. 2005)
TIC, (TOC)	Acid extraction with subsequent conductivity measurement; Woesthoff Carmhograph C16	(Blume et al. 2005)
Major elements (Ca, Fe, K, Mg, Mn, Na, P, S, Sr)	Aqua regia extraction / ICP-OES Perkin Elmer Optima 2100DV	DIN EN 13346 (Anonymous 2001); (Vogel et al. 2015)
Minor elements (Cd, Cr, Cu, Pb, Ni, and Zn)	Aqua regia extraction / ICP-OES Perkin Elmer Optima 2100DV	DIN EN 13346 (Anonymous 2001); (Vogel et al. 2015)
Specific Elements (Al, Si and Ti)	portable energy-dispersive X-ray fluorescence / p-ED-XRF Thermo Scientific NITON XL3t	(Tucker 2011)
Mineral composition	X-ray-powder diffraction/RIGAKU Miniflex 600	(Tucker 2011)
Easy soluable salts	Auqa dest. extraction with subsequent ion-chromatography measurement	(Blume et al. 2005)

Source: Own table

The weathering intensity was calculated using the well-established "chemical index of alteration" (CIA), developed by Nesbitt and Young. It reveals the removal of calcium, sodium and potassium from feldspars during weathering and brings their moles in proportion to alumina – formula (5) (Nesbitt & Young 1982; Li & Yang 2010).

$$\text{CIA} = \frac{Al_2O_3}{(Al_2O_3 + CaO^{**} + Na_2O + K_2O)} \times 100 \quad (5)$$

For this CaO** (the amount of CaO in the silicate fraction and in calcium carbonates) was determined by subtracting apatite and dolomite related CaO, which was estimated based on the contents of P_2O_5 and MgO (McLennan 1993). Due to the semiarid milieu of sedimentation, syn- and post-sedimentary precipitation of Ca and Na in carbonate and halite is expected. This, together with the bedrock formed by limestone and dolomite, makes a valid extraction of CaO in silicate fraction almost impossible and the calculated corrections bear considerable level of uncertainty. In consequence of the high evaporation potential of the soils, Na_2O was not used to substitute high CaO values as suggested by McLennan (1993). Therefore, the CIA values in this study were underestimated and affected by short term salinity changes. Though, relative changes are still sensitive for pedogenic variability and can be interpreted in terms of relative age estimation (Buggle et al. 2011).

The CIA calculation as well as the analysis and presentation of element correlation and element ratios, together with all statistical descriptions were implemented in Microsoft Excel.

2.4 Dating and establishing a valid chronostratigraphy

All investigated sediments were expected to hold very little amount of organic matter. Additionally, the research question focused on the morphodynamic correlation of different sediment bodies, which were formed by temporally and spatially connected processes. Therefore, the chronostratigraphy was based on datings derived from the measurements of mineral luminescence. This method was proven to be suitable for dating sedimentation ages from a variety of sedimentational environments (Singhvi & Porat 2008), also in Iran. Among these studies were datable sedimentations from complex geoarchives like alluvial fans and fluvial to lacustrine milieus (e.g. Walker & Fattahi 2011; Shanahan et al. 2013). Furthermore, e.g. Fattahi et al. (2006) measured OSL for successfully describing fault slip-rates in Iran (Fattahi et al. 2006).

The optically stimulated luminescence (OSL) was measured due to the sediments quartz rich mineral composition in the investigated sections. This OSL is emitted from quartz crystals (in this case) when they are exposed to light or heat. The luminescence signal has accumulated before by the naturally occurring radioactivity from surrounding minerals in a sediment, which is concealed from sunlight and

which remains with normal temperatures. This amount of absorbed energy per mass of mineral (1 J kg^{-1} = 1 Gy (Gray)) is called palaeodose or equivalent dose (D_e). The amount of energy which is emitted per mass of mineral over a certain time to the exposed sample (Gy a^{-1}) is called dose rate. The environmental dose rate comprises internal, external and cosmic dose rate components. The internal and the external dose rates are derived from potassium-isotopes (^{40}K), as well as from isotopes of the uranium ($^{238}U/^{235}U$) and thorium (^{232}Th) decay chains. The age (a) of a sample is the duration time since when the sample was concealed from sunlight and heat, and it is determined by calculating the ratio of palaeodose and dose rate (Preusser et al. 2008; Wintle 2008):

$$\text{Luminescence age [a]} = \frac{\text{Palaeodose [Gy]}}{\text{Dose rate [Gy } a^{-1}]} \quad (6)$$

The luminescence measurements for equivalent dose determination (D_e) of the samples from Damghan were performed at the luminescence laboratories at the University of Bayreuth and at the Justus-Liebig-University in Gießen. For D_e determination a Risø luminescence reader DA-15 (Bayreuth) and a Lexsyg luminescence reader from Freiberg Instruments (Gießen; cf. Lomax et al. 2014) were used.

For the study in Damghan, samples were taken from key stratigraphic layers, which provided an adequate amount of small grain sizes (sand to silt). The samples were prepared at night, as block sample of hardened fine sediments, or as bulk samples from loose materials. A sufficient amount of material of the surrounding layers was also taken for the determination of the environmental dose rate. The sampling focused on the generations of alluvial fan surfaces, which were previously identified during mapping works, as well as on the fine sediment terrace, which is described above. At least two samples were taken from every section, which allows distinguishing active surface layers of reworked alluvial sediments from the subsurface main sediment body.

From each sample the quartz coarse-grain fraction (90 - 200 μm) was extracted and small aliquots were used to detect insufficient bleaching (Fuchs & Wagner 2003). The determination of the equivalent dose followed an adapted single aliquot regenerative protocol (SAR) after Murray and Wintle (Murray & Wintle 2000). Up to 24 aliquots were measured for D_e determination. The dose rates were calculated using a combination of α-counting and ICP-OES. For details about laboratory procedures refer to Fuchs et al. 2015.

The bleaching of the alluvial fan sediments was insufficient due to an increased amount of deposits from high energy events like debris flows and sheet wash. Hence, sand size fraction of quartz minerals was abundant, but for all samples from Damghan Basin a strong to very strong scatter of the equivalent dose was measured. This is a common observation when dealing with these types of sediments, and there are several techniques for deriving a minimum equivalent dose. All techniques depend on the statistical distribution of D_e-values in a typical insufficiently bleached sample (cf. Fuchs & Lang 2009). However, due to the large scatter of D_e-values and an unclear positive skewness, only maximum values were calculated for all samples, and therefore only maximum ages could be derived.

3 Results and Synthesis

3.1 Quaternary mapping and map unit description

3.1.1 Map sheets overview

All five map sheets together cover the area between the central playa with its lowest point at 1 051 m a.s.l. up to the watersheds in Alborz Mountains with the highest peaks at 2 460 m a.s.l. Each single map has an extent of 11.2 x 13.9 km and a scale of 1 : 25 000. Map sheets are named and numbered following the sheet division of the standard geological map 1 : 25 000, of the Geological Survey of Iran. Prepared maps are named as followed from north-west to south-east, and all maps are attached (Appendix I):

- *Sheet 6962IV-SW "Geomorphological map of Shahrak-e-Mehmandust"*
- *Sheet 6962IV-SE "Geomorphological map of Kalateh-Molla"*
- *Sheet 6962III-NW "Geomorphological map of Mehmandust"*
- *Sheet 6962III-NE "Geomorphological map of Pariabad"*
- *Sheet 6962III-SE "Geomorphological map of Kavir-e-Haj Aligholi"*

Sheet 6962IV-SW "Geomorphological map of Shahrak-e-Mehmandust" is situated 20 km east to the City of Damghan, and motorway and railroad between Semnan and Mashad cross the map sheet in the south-eastern corner. The sheet is two parted, in a northern half covering west to east oriented Alborz mountain ranges with antecedent drainage valleys and the southern half with the megafan of Mehmandust in the west and the adjacent alluvial apron constituting the footslope to the east. Additionally, the mountain ranges are disconnected by a structural basin 2 x 6 km big, which has developed alongside the Dehmolla Syncline, and by the valley of the mega fans watershed which broadens up to a width of over 3 km. The mega fan is 8.5 km wide and 10 km long and the central part is lifted by faulting. The fan's apex is at an altitude of 1 476 m a.s.l. and the toe's average altitude is at about 1 110 m a.s.l. The alluvial apron is separated from the mega fan by a sharp border marked in a considerable change in level. The apron is 6 km long and continues after about 5 km over the map sheets border. Its toe holds an altitude of about 1 120 m a.s.l., and apices are located at altitudes between 1 400 and 1 500 m a.s.l.

The footslope continues to map *Sheet 6962III-NW "Geomorphological map of Mehmandust"*, where the transitional zone from footslope to fluvial plain is covered by the agricultural lands of the village of Mehmandust. From the east the drainage way of Shahrud River enters the area and the south-west corner shows the recent fluvial plain of Damghan drainage ways. In the southern part of the map fluvial terraces are mapped. Their morphological situation does not completely follow the rules of fluvial morphodynamics, but shows clear alteration by neo-tectonic activity. This has lifted the fluvial plain sediments about 2 - 4 decimeters so that they form a slightly higher level where incision can affect sediments and aeolian deposits can prevail on the surfaces.

The continuation of the alluvial apron represents the central part of the north-eastern-most map *Sheet 6962IV-SE "Geomorphological map of Kalateh-Molla"*, and it is covering the whole distance between the sheet borders, with comparable length and vertical extents. At the eastern end of the alluvial apron it is replaced by the thicker sediment body of another mega fan. Mountain ranges in the north feature small valleys less than 100 m wide and in the eastern part the orientation of the ranges changes from an overall west-east direction to a southwest-northeast striking, with 63° and a parallel drainage system. The southern part of the map is occupied by settlements and anthropogenous land surfaces sitting on top of alluvial footslope sediments. They merge into the fluvial plain which has been formed by floods of Shahroud River from reworked alluvial fan material.

The perennial but spatial unstable system border of footslope and fluvial plain processes marks the northern end of *Sheet 6962III-NE "Geomorphological map of Pariabad"*. Here, fluvial terraces and a recent fluvial plain of Shahrud River are mapped. They are directed around emerging gypsiferous marls and conglomerates from M^r - Upper Red Formation, which are eroded and hence surrounded by small alluvial fans, 500 - 1000 m in diameter. The denudational zone of M^r transfers to fluvial terraces continuing in a wide arc to the west *Sheet* border. They are affected by tectonic activity and have already been described for *Sheet 6962III-NW*.

The fluvial plains shift from sandy-silty fluvial plains to loamy fluvial plains already north to the map *Sheet 6962III-SE "Geomorphological map of Kavir-e-Haj Aligholi"*. The plains in this map can merely be distinguished by differing lithological origins and by the distinct presence of evaporation at their surfaces. The southern part of the map describes the sequence of dry mud flat and wet, saline clay flat, which are surrounding the massive halite crust of the central playa. Dry mud flat forms a belt of 500 - 3000 meters in width and the saline clay flat has the same form with 3 500 - 4000 meters. The transition into and between this zones is not sharp and follows a migrating zigzag-line.

The diversity of map elements increases from playa to mountain ranges, while average size of mapped features decreases. Fragmentation of quaternary landforms has its maximum close to the active depositional lobes and at the distal ends of the alluvial fans, where most recent landform development takes place and forms of different activity phases are well contrasting to each other. There is an overall shift from erosional and denudational forms in the mountain ranges in maps 6962IV, over denudated old alluvial surfaces interchanging with areas of active alluvial fan deposition on the footslopes (maps 6962IV), to zones of sediment accumulation and storage in the central depression (maps 6962III). This general order is disturbed where neo-tectonic activity changes topography. Thus, inherent morphodynamics can still affect the landforms, while transition and uplift at faults also becomes morphologically evident (maps 6962III-NW & -NE). The maps describe geomorphological features which group in five categories, as written before (Chap. 2.1):

(1) Geomorphodynamics and Geomorphogenesis
(2) Geomorphography & Geomorphometry
(3) Geomorphostructure
(4) Changes of geomorphic structures and processes
(5) Areas of geomorphic structures and processes

From these analytical map elements, a stratigraphic synthesis was derived by putting the areas and contacts of geomorphic structures and processes into stratigraphic and chrono-stratigraphic order with known geological formations. Thus, new quaternary map units were defined to compile a complete stratigraphic description for the whole mapping project.

3.1.2 Stratigraphic description of map units

The stratigraphic description follows the legend in the Stratigraphic Overview Map (Appendix II). Focus of mapping was laid on a sound explanation of quaternary features in the area, while older formations are derived from the Geological map of Shahrud, 1 : 100 000 (Vaziri & Majidifard 2000) and Gorgan and is based on previous studies (e.g. Aghanabati 1994). These geological map units had been updated by detailed remapping of contacts and faults in satellite images.

3.1.2.1 Precambrian

- $P€_{br}$ – Bayandor Formation (6962IV-SE)

The Bayandor formation originally discovered and introduced by Stöcklin et al. (1964) in Bayandor Mountains nearby Zanjan has almost 498 m thickness (Stöcklin et al. 1964). It consists of alternations of purple sandstone shale and silt with micaceous shale and silty sandstone and brownish dolomites with evidences of stromatolite. Thickness varies spatially due to faulting and deformation. While some researchers limited occurrence of this formation to Zanjan area and Azerbaijan, there are also reports from Damghan, Firouzkooh and Damavand area. Hamdi (1985) introduced Bayandor as Jurasic-Cretaceous but the research by Ghavidel (1985) based on palynology states that Late Riphean is the age of this formation (Aghanabati 1994).

3.1.2.2 Cambrian

- $€_s$ – Soltanieh Formation (6962IV-SE)

The formation consists of massive dolomite with an alteration of black shale. The dolomites are scarp-forming and stromatolite-bearing (Collenia spec.) The intercalated Chapoghlu Shale seems to be the oldest known fossilized organic matter in North Iran (Berberian 1974). The studies by Stöcklin, Salehi and others have shown that the upper part of Soltanieh Formation belongs to lower Cambrian. Lasemi (2000) has divided Sultanieh Formation to two main carbonate sequences. Hamdi (1989) claimed that the boundary of Precambrian-Cambrian goes through Soltanieh Formation (Hamdi 1989). There are some indications of mineral resources in Soltanieh Formation in Damghan area. Especially fluorine, zinc, Pb and barium, and identified as F-rich MVT (Mississippi Valley Type) deposit by Rostami Paydar (2002, in Aghanabati 1994).

- $€_{bt}$ – Barut Formation (6962IV-SE)

Barut Formation with approximately 711 m thickness, including sandstone and shale with dolomite intercalations, has been introduced in Zanjan area and is

extending also to the east of Tehran, Shahmirzad and other localities with different thickness and little lithologic components (Aghanabati 1994). The formation is apparent for its regular alteration of mainly purple shales with thin layers of dolomite and limestone (Berberian 1974).

- $€_z$ – Zagun Formation (6962IV-SE; 6962IV-SW)

Zagun Formation consists of reddish to purple fine grained clastic materials including foliated slaty shale, siltstone and sandstone. This formation shows smoother outcrops in comparison with Barut Formation as a result of lithology, and there are some indications of evaporites and mud cracks that appear like forms from meandering rivers (Berberian 1974; Lasemi 1990, in Aghanabati 1994).

- $€_l$ – Lalun Formation (6962IV-SE; 6962IV-SW)

Lalun Formation basically consists of reddish sandstone with some shale horizons and has variable thickness (400 - 600 meters). The white arkose which is covering the reddish sandstones are not considered any more as part of this formation. The fossil indicators in this formation are limited to Cruziana (Aghanabati 1994).

- $€m_1$, $€m_{2-5}$ – Mila Formation (6962IV-SE; 6962IV-SW)

The Mila Formation originally discovered and introduced by Rothner et al. (1963) in Mila Kouh of Damghan area. It has a thickness of 585 m and is divided to five members. The sequence of dark grey dolomite, yellow shale and marl is topped by the white quartzite of €m1 (Aghanabati 1994). Youngest studies divide traditional Mila Formation into Fasham Formation, the Deh-Sufiyan Formation and the Deh-Molla Formation. Hence the new Mila Formation is constituted by these Formations and the lower Ordovician Lashkarak Formation (Geyer et al. 2014).

3.1.2.3 Ordovician

- O1 – Lashkarak Formation (6962IV-SE; 6962IV-SW)

Lashkarak Formation with about 175 m thickness at its type locality was introduced by Gansser & Huber (1962) in the east of Kalardasht and north of Taleghan (Gansser & Huber 1962). It has been divided to 3 units including shale and sand stone with dolomite intercalations, Limestone and an alternation of shale and sandstone with lime. Based on paleontological evidences (Michelinoceras sp., Orthoceras sp.) Lashkarak Formation is referred to lower-middle Ordovician (Aghanabati 1994).

3.1.2.4 Devonian

- Dj_{1-3} – Jirud Formation (6962IV-SE; 6962IV-SW)

The history of lower and middle Devonian is not totally clear yet, but it is known that the general Caledonian Geologic Event had huge impact on it. Basic magmatic activities including intrusion and extrusion are also refered to this event, especially the syenites of Julfa and Marand area (Aghanabati 1383). Lower Devonian continental deposits are consisting of reddish sandstones with dolomite intercalations and locally gypsum horizons, particularly in eastern Alborz and Central Iran. The

reddish sediments also named Padeha Formation that has no clear variation in the lithology of Damghan area. Jirud Formation is known very well in central Alborz, especially for its phosphate deposits in clastic sediments (Aghanabati 1994).

3.1.2.5 Triassic

- TR_{e1-2} – Elika Formation (6962IV-SE; 6962IV-SW)

Lower to Middle Triassic deposits in Iran are very similar to Alpian Triassic facies in Europe. The deposits generally have marine facies while upper Triassic deposits originate from organic material and show considerably different facies. The upper part consists of dolomite and dolomitic limestone while the lower parts incorporate platy to shaly limestone and variable marly conglomerates (Berberian 1974). The boundary between these two major facies bears evidences of magmatic activity, faulting and folding referred to early Cimmerian event. Lower-Middle Triassic consists of a carbonate sequence and was introduced as Elika Formation. The base of formation consists of laminated lime and marly limestone with dolomitic intercalations. The lower part of the formation is called "Vermiculated limestone" due to inherent verm-indications (Aghanabati 1994).

3.1.2.6 Jurassic

- J_{s2-3} – Shemshak Formation (6962IV-SE; 6962IV-SW)

Shemshak Formation or Shemshak Group varies in lithology in different localities but generally consists of clastic sediments partly with organic horizons. There are considerable coal horizons as a result of alpidic orogenesis and a shift from shallow water to lagunal-fluviatile sedimentation (Berberian 1974). This makes the Shemshak Formation interesting in economic geology aspects.

- J_l, J_d – Lar Formation (6962IV-SW)

Lar Formation (Upper Jurassic) consists of gray massive fine grained limestone. Because of the lithologic composition of Lar Formation, it has high relief in contrast with other units. Lar Formation is fossil-bearing and can be ordered into Upper Jurassic (Aghanabati 1994).

3.1.2.7 Miocene

- M^r – Upper Red Formation (6962III-NE)

The most common, wide spread formation from Miocene is Upper Red Formation, which is basically consisting of salt-bearing reddish marl sandstone and conglomerate with several evaporite horizons. The salts concentrate in the lower part of the sequence and the gypsum horizons in the upper part (Aghanabati 1994).

3.1.2.8 Neogen

- Ng^c – ? F. (6962IV-SE ; 6962IV-SW)

Neogene conglomerate in Iran covers intramontainous basins widely from Central Iran to Alborz. There is no paleontological evidence to provide a proper age of the

sediments, but there are some dating results from volcanic rocks, associated with the Neogene sediments. There are also some relations to salt diapirs in Semnan area (Aghanabati 1994). Prominent formation in this unit is the Hezardareh Formation which covers the Pliocene and early Quaternary period. It is the lowest alluvial formation in North Iran and comprises conglomerates, with sandstones and mudstone. In contrast to younger alluvides it shows a conformal or transitional contact to footwall Upper Red Formation (Berberian 1974; Stöcklin 1971).

3.1.2.9 Quaternary

Focus of the study was laid on Quaternary map units. The following paragraphs are a brief outline of more detailed descriptions within chapter 3.2, 3.3 and 3.4.

- $Q^{ap}1$-5 – Eroded Alluvial Fans and Aprons (6962IV-SE; 6962IV-SW)

Alteration of alluvial fan surfaces is the key to distinguish their chronostratigraphic position. This hypothesis was approved when mapping and classifying the alluvial gravels on alluvial apron and fans in the mapping area. The ages of the different surfaces and their chronostratigraphic order in the periods of MIS 3, MIS 2, early MIS 1, Atlantic and Subatlantic are derived from 14 OSL ages (sampled and measured in this project – Chapter 3.4) and their relationships with the sequence-stratigraphy of alluvial apron and floodplain that was revealed by geomorphological mapping. In addition to that $Q^{ap}5$ can be correlated with a progradation of the Hezardareh Formation, which is repeatedly described for North Iran and which originates in Pliocene period (Rieben 1955; Rieben 1966; cf. Chap. 3.1.2.8).

Figure 3.1.1 gives an impression of the initial surface description as observed in the field and when mapping from aerial images. Distinct patterns of surface roughness and dissection indicate the map units' distribution. All units are covered by desert pavement, while its different age generations can be inferred to a certain degree by color and thickness of desert varnish. Also the shape of channels and slopes is a strong indication for landform generations.

- $Q^{al}0$-1 – Recent to Subrecent Alluvial Fan Accumulation (6962IV-SE; 6962IV-SW; 6962III-NE; 6962III-NW)

Alluvial Fan Accumulation could be distinguished in two main areas. The first are the active areas of the big alluvial apron and the megafan. Within this areas surface gravels are eroded, reworked and deposited periodically in high energy flood event during springtime gravels are eroded at the mountains slopes and deposited in debris flow lobes inside the incised fan channels or even spread below the intersection point of the active fan lobe. The second area for this formation is the zone where much smaller young alluvial fans are prograding into the floodplain of preflooders and playa. They had been investigated in detail in sheet 6962IV-SE and show coarse grains sizes and high gravel contents in comparison to surrounding fine sediments. Layers with high values of sulphur correspond to increased Sr-Values. This signalizes generally autochthonous gypsum development in brines, which cannot be explained completely here, but may indicate lake level high stands or flooding-dry-

Figure 3.1.1: Field characteristics and optical differentiation of eroded alluvial fan surfaces 1 to 5 (aerial view: Bing Maps Aerial – Microsoft Corporation and its data suppliers 2011); field pictures: C. Büdel 2011).

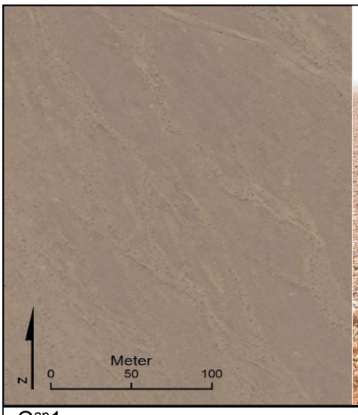

- Desert pavement (yermic horizon)
- calcic horizon
- fossil B-Horizon, moderately cemented (calcic-gypsic)
- remote sensing optical properties: scattered surfaces divided by wide, saucer-shaped rills and active channels; < 100 cm deep

$Q^{ap}1$

- Developed desert pavement (yermic horizon)
- Thick, partly weathered calcic horizon
- fossil B-Horizon, moderately cemented (gypsic-petrogypsic)
- remote sensing optical properties: autochthonous dissection in shallow, saucer-shaped rills; < 100 cm deep

$Q^{ap}2$

no ground truth possible!

- desert pavement
- remote sensing optical properties: autochthonous dissection in narrow, v-shaped rills; > 100 cm shallow

$Q^{ap}3$

Continued on the next page.

Continuation of Fig. 3.1.1

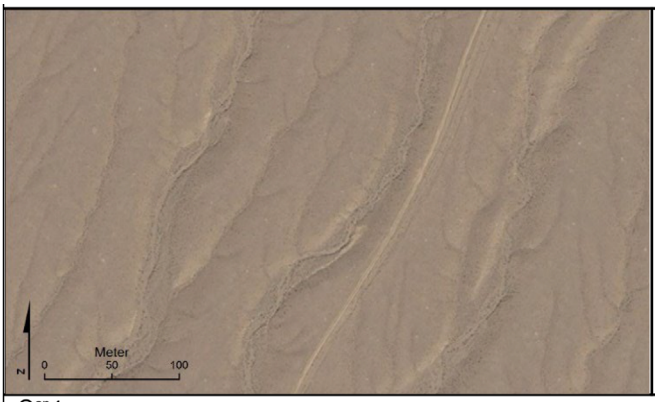

no ground truth possible!

- desert pavement
- remote sensing optical properties: autochthonous dissection in wide, saucer-, and v-shaped rills; > 100 cm deep

$Q^{ap}4$

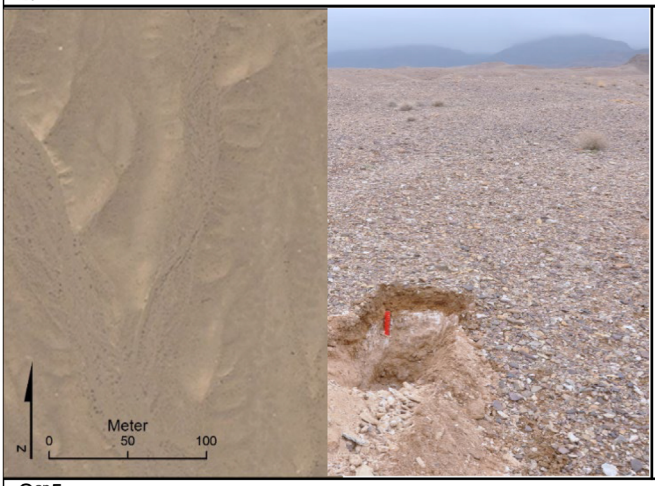

- Developed desert pavement (yermic horizon)
- gypsum crystals > 14 cm
- Gypsum crust thickness > 40 cm (thick gypsic horizon)
- remote sensing optical properties: autochthonous dissection in wide, saucer-shaped rills and valleys; > 200 cm deep

$Q^{ap}5$

Source: Own illustration

ing-events. Subrecently deposited surfaces are characterized by considerably higher Mg- and Al-concentrations, together with more layers with autochthonous gypsum precipitation and generally finer grain sizes.

- $Q^{f}0\text{-}1$ – Recent to Subrecent Fluvial Terraces and Floodplains (6962IV-SE; 6962IV-SW; 6962III-NE; 6962III-NW; 6962III-SE)

Fluvial activity can be observed throughout the whole mapping area. It is distinguished from alluvial fan activity by the lack of forces of mass movement and by their channel-dependent flow structures. Hence, incised channels in old surfaces of the alluvial apron were mapped as fluvial landforms. Lithology of these sediments does not differ from those of the alluvial fans, but the terrace bodies show signs of imbrication, trough cross bedding and sorting more continuously than the more turbulent alluvial fan deposits with signs of high energy flow events.

- P^{er} – Eroded Lake and Playa Sediments (6962IV-SE; 6962IV-SW)

Intensive studies had been conducted to reveal the nature of these sediments (cf. Chap. 3.3). Physical and chemical analyses show a dominance of loamy to sandy silts, coincide with layers of sand and gravel. Sulfate values are increased within the first three meters of sediment, while calcium-carbonate is high throughout the whole profile. Increased iron-values correspond to high input of courser grained sediments as it is with peaks of Ca-values, too.

- P^{df} – Playa, dry mud flat (6962III-SE)

The dry mud flat of the playa is set up by high flood clays and loams which deposit during episodically to periodically occurring flooding events. Lacustrine clays are intercalated with fluvial silty and sandy loams which are supplied by receiving waters of the surrounding river systems periodically.

- P^{sf} – Playa, saline clay flat (6962III-SE)

The saline clay flat is dominated by periodically occurring ground water influx, which controls salinity and evaporite precipitation in this area. The sediments are typically wet during long periods and imped access to the central salt pan. Their physical and chemical setup is presumed to be altered by ground water dynamics, which could not yet be investigated.

- P^{l} – Central Playa (6962III-SE)

Two test sites and three core sampling locations had been established to investigate the central playa with its solid salt crust (cf. Chap. 3.3). The Team found, that the alternation of salt crust and intercalated loam occurs down to a depth of 3.4 meters. The sedimentological description together with laboratory element analyses shows saline conditions in this first three meters coincide with general coarser grain sizes. The next three meters are made up by homogenous partly laminated deposits, rich of clay and silt and with a decreased content of sulphur and halite. Regular peaks of sulfate and calcium within this unit presumably indicate post-sedimentary precipitation of gypsum. The homogenous sediment unit is followed by layers clearly set up in three major phases of up-fining sediments. Higher Al and Mg contents following this sedimentation phases suggest a considerable amount of syn-sedimentary clay mineral enrichment.

- A^{a} – Anthropogenic accumulation (6962IV-SE; 6962IV-SW; 6962III-NE; 6962III-NW)

Al over the mapping area, human activity is a factor. The area was intensively used since pre-Islamic times when it was settled in Atlantic period and agricultural use and gardens occupied the zone surrounding the playa early. Furrowing irrigation and cattle-keeping needed infrastructure and for its construction brick yards exploited the clay sediments. Today housing and traffic occupies wide areas, in which surface materials are intensively reworked and accumulated (Schmidt 1937; Costantini, Dyson, JR. 1990).

3.1.3 Characteristics and spatial distribution of map elements

As previously described (Chap 2.1) the mapping area represents a transect, which is extending from the Alborz mountain range to the basins central depression. Therefore, geomorphologic characteristics of the landforms can not only be described by their geometry and landform genesis, but also by their spatial distribution and topologic relationship. This is primarily valid for the quaternary map elements which are still located in spatial relation, or even as active or passive element of their depositional systems. Areas under control of active fluvial and slope fluvial processes cover 43 % of the mapping area ($Q^{f}0$ and $Q^{al}0$ in Tab. 3.1.1). These are followed up by the areas of active orogenesis and denudation – subsumed here as "geological units" – with a total of about 20.3 %, and then by the mostly concealed, reshaped anthropogenic areas with 8.9 %. The Basin is represented by dry mud (P^{df}) and saline clay flat (P^{sf}), which are accommodating the central salt pan (P^{l}), together covering a surface percentage of 6.7 % of the mapping area.

Table 3.1.1: Total area and area percentage of all mapping units, with focus on the quaternary units.

	km²	Percent
Mapped totals	771,9	100
Sum of geological units	157,0	20,34
$Q^{ap}5$	12,8	1,66
$Q^{ap}4$	39,7	5,14
$Q^{ap}3$	11,0	1,43
$Q^{ap}2$	3,4	0,44
$Q^{ap}1$	41,6	5,39
$Q^{al}1$	2,9	0,38
$Q^{al}0$	86,0	11,14
$Q^{f}1$	45,8	5,94
$Q^{f}0$	246,0	31,86
P^{er}	5,6	0,73
P^{df}	24,8	3,22
P^{sf}	26,2	3,40
P^{l}	0,3	0,04
A^{a}	68,6	8,89

Source: Own table

The distribution of the stratigraphic map units regarding their elevation and slope, reveals increasing steepness, which correlates with higher elevation (Tab. 3.1.2). Furthermore, the majority of the area of anthropogenic accumulation (A^{a}) is located at the same altitudes than the most of the areas of recent and active slope-fluvial activities ($Q^{al}0$). This demonstrates the morphological risk the majority of settlements is exposed to, and it emphasizes the big efforts the villagers

afford to build protective dams and channels. The classes $Q^{ap}1$-4 do not significantly occupy diverging slope sections, despite the circumstance that they fairly concentrate on distinct altitudes. This supports the theory of generations, or cycles of morphologically equal alluvial sedimentation phases, which are differentiated primarily by time and not by the type of their formative processes. Class $Q^{al}0$ represents areas of recent to sub recent alluvial fan accumulation. Hence, it appears in high altitude, proximal alluvial fan sections, where transportation and temporal storage of sediments in incised fan head trenches was mapped. The surfaces of the $Q^{al}0$ alluvium are deposited within the 4°-7° slope category, which represents proximal deposition, with frequent torrential coarse clast transport and debris flows. Essentially $Q^{ap}2$ and $Q^{ap}5$ were mapped in this steep alluvial fan areas, while the surfaces of $Q^{ap}4$, 3 and 1 feature more gentle slopes of 2°-4°. This is not solely depending on formative processes but also on the grade of surface preservation, which again depends on slope erosion and on the reworking of alluvial fan surfaces, as a function of flood power and sediment supply during proximally controlled progradation. Logically, $Q^{al}1$, which is correlated with lake level retreat, could have only been observed in lower altitudes, where distal alluvial fan dissection takes place (cf. Harvey 2012).

Table 3.1.2: Quaternary map units' zonal histograms for elevation- and slope-classes. Classification of elevation follows the natural breaks classificator by Jenks used in ESRI ArcMap (Smith et al. 2015) and for slope classification standards from German GMK 25 mapping system were used Leser & Stäblein 1985.

Elevation [m a.s.l.]	Geol (Sum)	$Q^{ap}5$	$Q^{ap}4$	$Q^{ap}3$	$Q^{ap}2$	$Q^{ap}1$	$Q^{al}1$	$Q^{al}0$	$Q^{f}1$	$Q^{f}0$	P^{er}	P^{df}	P^{sf}
1.050 - 1.075	3	0	0	0	0	0	47	13	41	75	0	100	100
1.075 - 1.150	14	0	6	6	1	18	53	54	59	23	66	0	0
1.150 - 1.215	0	0	22	1	7	38	0	18	0	0	34	0	0
1.215 - 1.350	1	16	59	60	88	40	0	11	0	0	0	0	0
1.350 - 1.625	25	64	14	34	4	3	0	4	0	2	0	0	0
1.625 - 1.765	19	19	0	0	0	0	0	0	0	0	0	0	0
1.765 - 2.040	26	0	0	0	0	0	0	0	0	0	0	0	0
2.040 - 2.180	6	0	0	0	0	0	0	0	0	0	0	0	0
2.180 - 2.455	5	0	0	0	0	0	0	0	0	0	0	0	0
% - Sum	100	100	100	100	100	100	100	100	100	100	100	100	100

Slope [deg.]	Geol (Sum)	Qap5	Qap4	Qap3	Qap2	Qap1	Qal1	Qal0	Qf1	Qf0	Per	Pdf	Psf
0 - 0,5	1	0	1	1	1	2	18	10	19	18	4	10	18
0,5 - 2	11	3	27	16	10	28	55	54	69	60	53	62	62
2 - 4	7	14	46	49	33	47	23	27	11	17	38	24	16
4 - 7	7	40	22	32	40	20	3	8	1	2	5	2	1
7 - 11	13	27	3	2	9	1	0	0	0	1	0	0	0
11 - 15	13	8	0	0	3	0	0	0	0	0	0	0	0
15 - 35	43	8	0	0	3	0	0	0	0	0	0	0	0
35 - 60	4	0	0	0	0	0	0	0	0	0	0	0	0
> 60	2	0	0	0	1	1	0	1	0	1	0	2	3
% - Sum	100	100	100	100	100	100	100	100	100	100	100	100	100

Source: Own table

Figure 3.1.2: Overview map of the generalised geomorphostructural map units in the mapping project. The majority of the units are the basic geological map elements placed in a geomorphologic context.

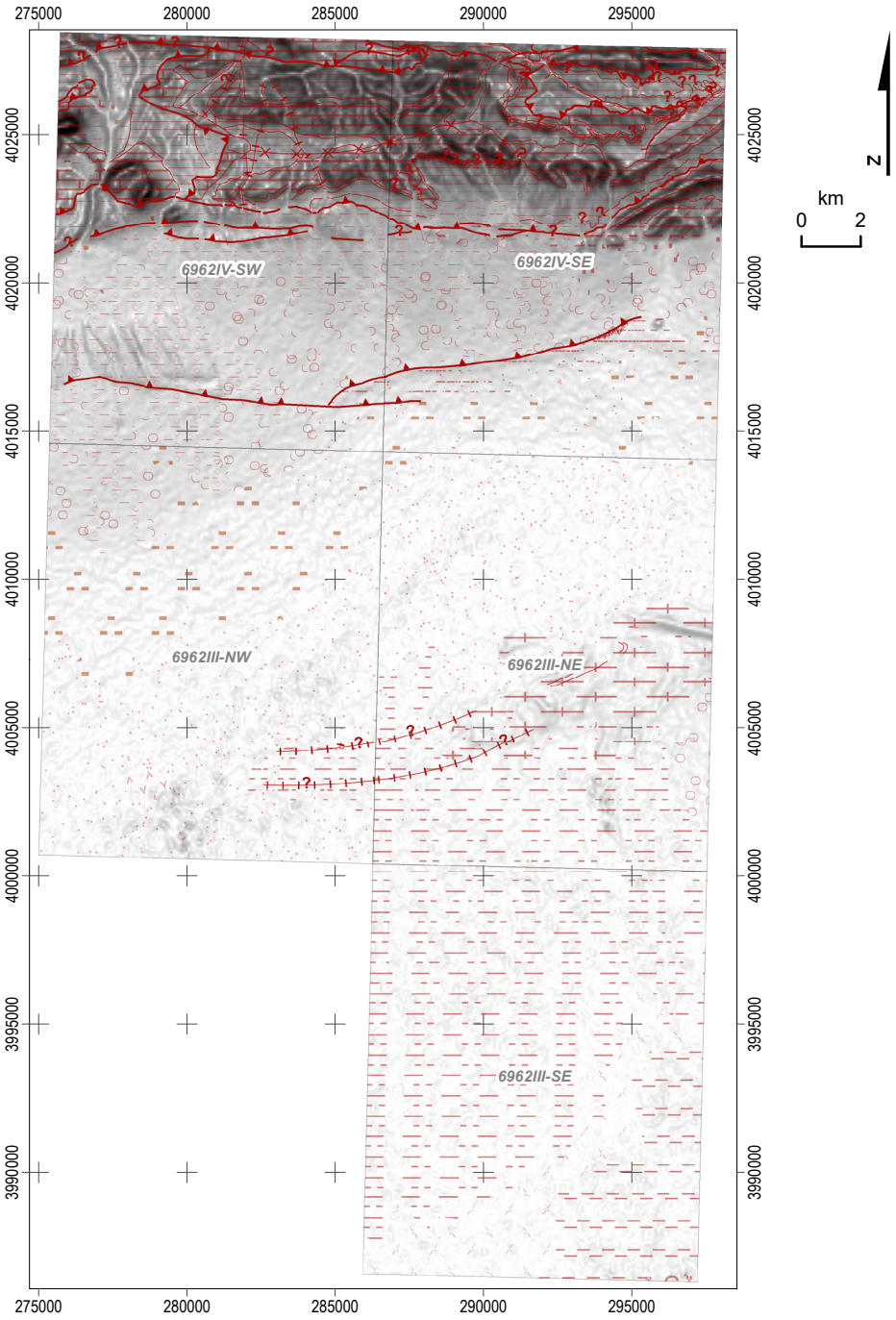

Continuation of Fig. 3.1.2

Geomorphostructure

- contact
- gradational contact
- syncline
- fault
- thrust fault

- anthropogenic accumulation
- halite
- sandstone
- quartzite
- limestone
- dolomite
- shale
- marlstone
- effusive, extrusive rocks
- conglomerate
- clay
- loam
- silty loam
- sand
- grit
- gravels
- debris

- Map Sheets

SRTM derived slope

Source: SRTM DEM - NASA JPL 2013
Map Projection: UTM Zone 40N
Map compilation: C. Büdel, 2016

Figure 3.1.3: Relationship between alluvial surface ages and the morphometry of their bounding slopes. Maps show steps up to 1 m high (A), steps and steep slopes of 1-5 m height (B), steep slopes and cliffs higher than 5 m (C) and flat slopes 5-20 m high (D).

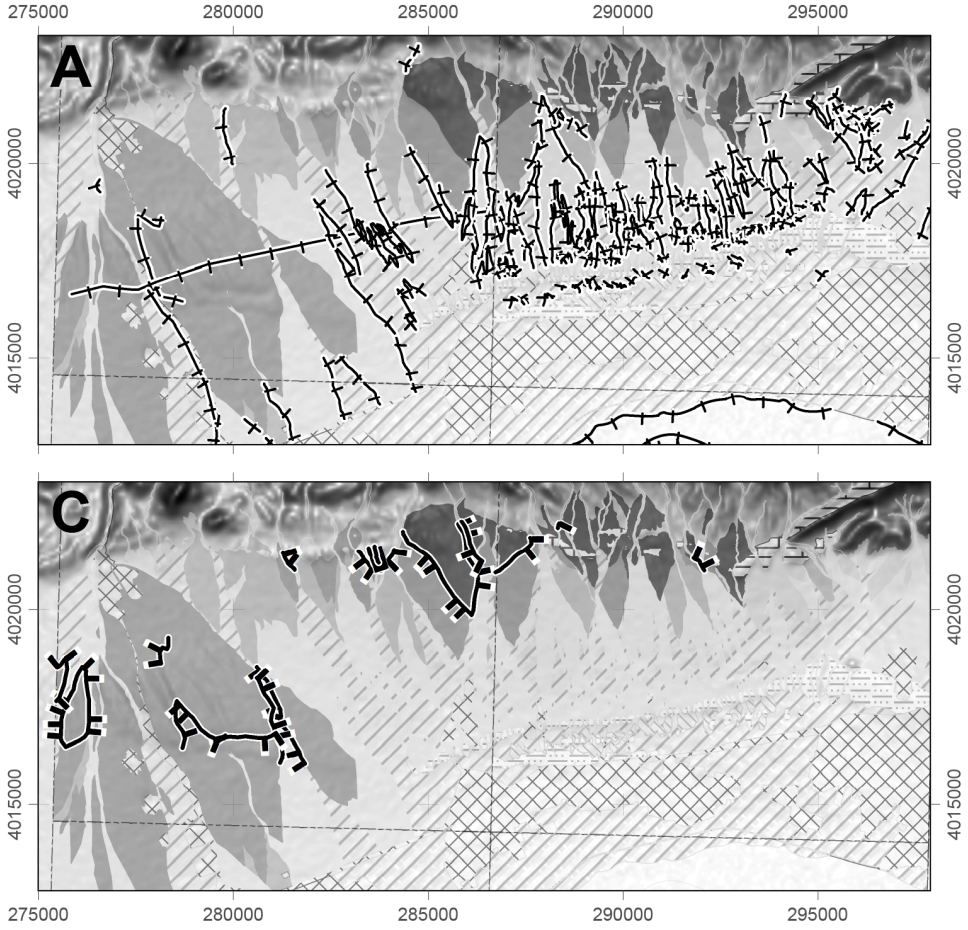

Steps and Steep slopes

- step: h: 0-1m, w: 1-5m
- step: h: 1-5m, w: 1-5m
- steep slope: h: 1-5m, w: 5-10m
- steep slope: h: 5-20m, w: 5-10m
- slope: h: 5-20m, w: >10m
- cliff: h: >20m, w: 5-10m

Chrono-Stratigraphic Units

- Aa - Anthropogenic accumulation
- Ebt - Cherty dolomite, limestone
- Qf0 - Fluvial Terraces and Floodplains
- Per - Eroded Lake and Playa Deposits
- Qal0 - Recent Alluvial Fan Sediments

Continuation of Fig. 3.1.3

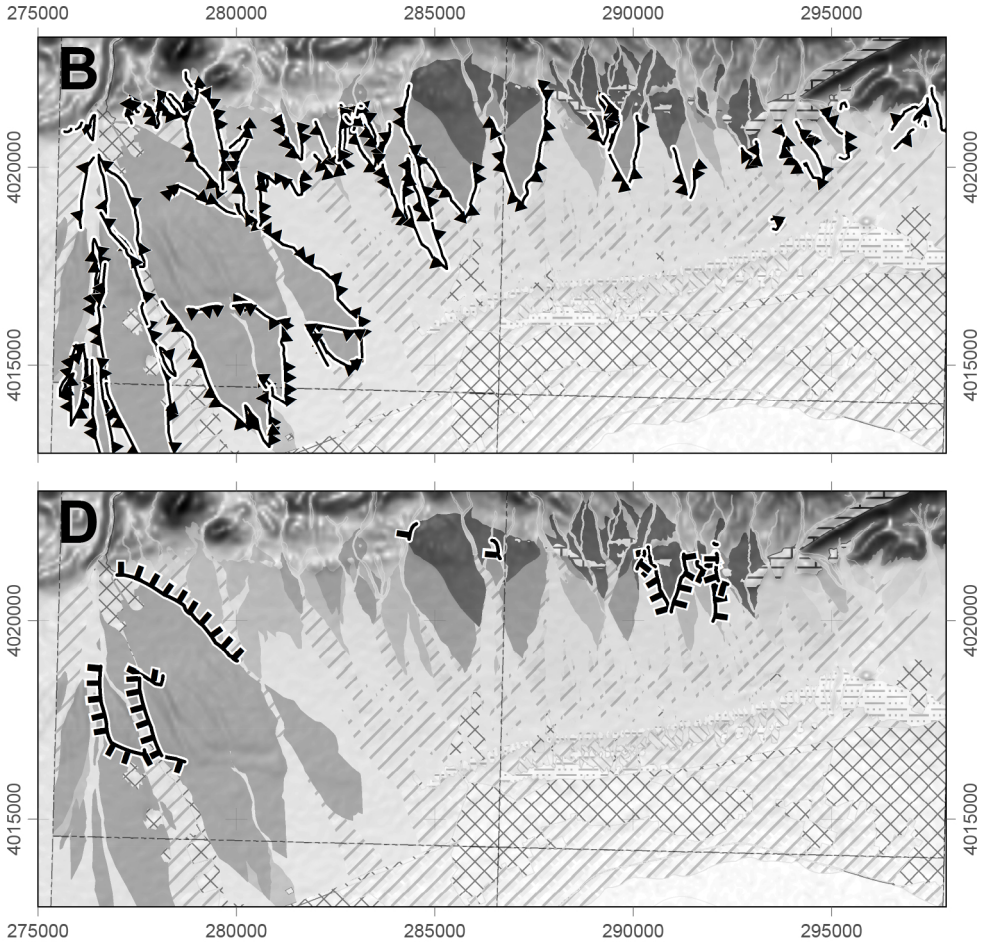

Source: Own illustration

Figure 3.1.4: Overview map of geomorphodynamic map elements in the mapping project. The map shows the major active morphodynamics on quaternary surfaces, which are not already revealed by the areas of structure and process. The activity was identified in multi-temporal remote sensing data or directly and indirectly observed in the field.

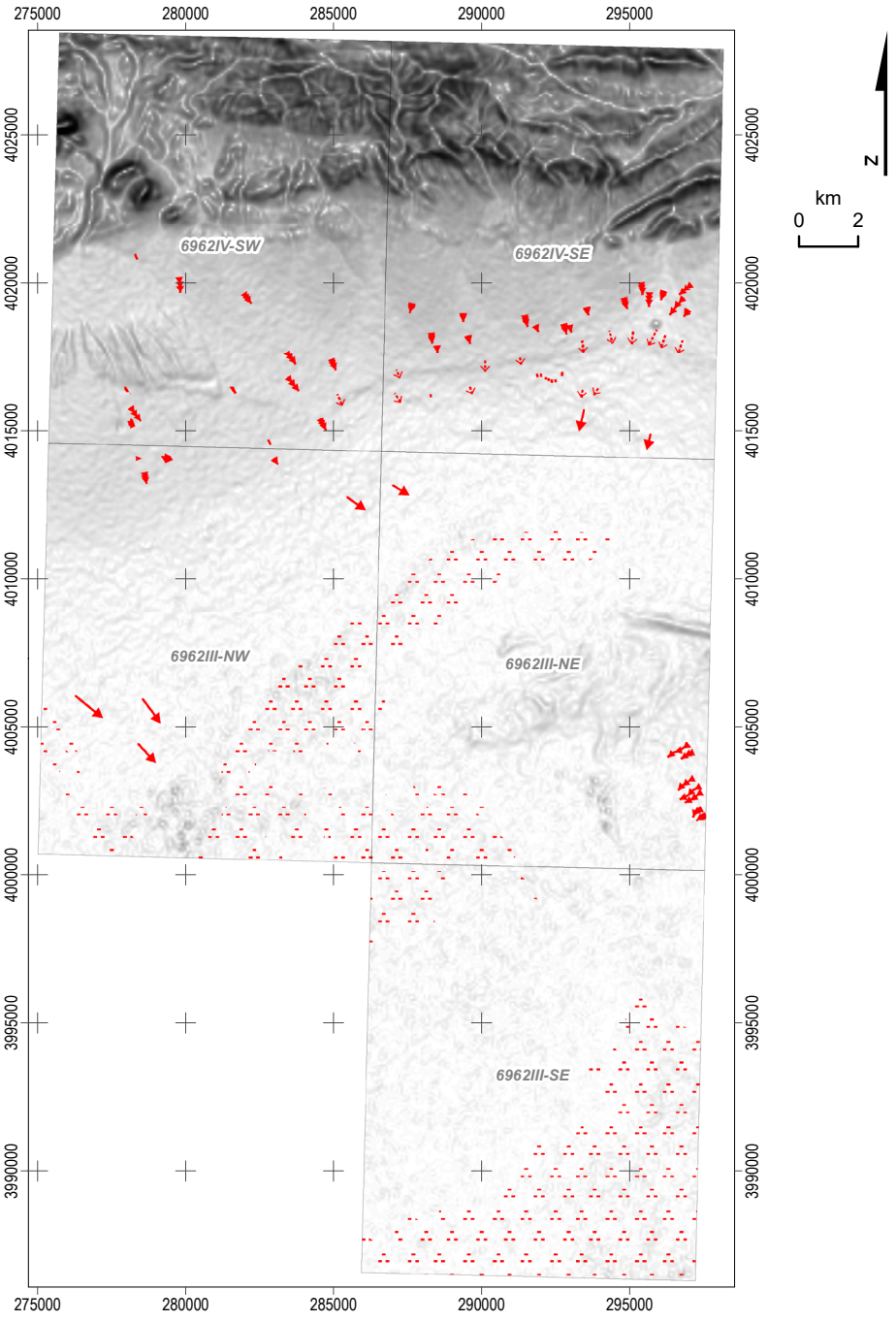

Continuation of Fig. 3.1.4

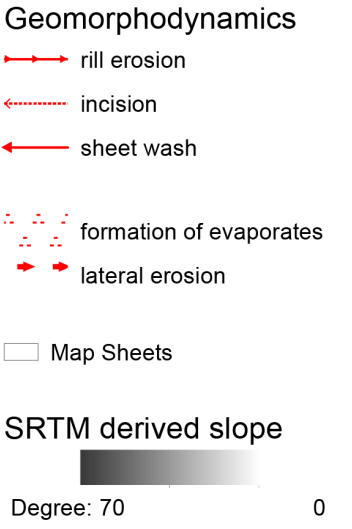

Distribution of morphostructural features

Morphostructural features in the mapping project which were not related to quaternary systems have been vectorized from the 1 : 100 000 geological map of Shahrud (Vaziri & Majidifard 2000). The spatial properties of linear map units like contacts and faults, and the extent stratigraphic units were updated using remote sensing imagery, while quaternary surface lithology was classified based on field observation and aerial imagery. Therefore, structural information is still ambiguous in the maps, by means of faults and lithologic contacts which are precisely mapped in mountain ranges, but more and more inferred under quaternary sediments towards the basins center. Here, the lithology is dominated by loose sediments, broadly classified by their major texture class. A prominent feature is the left-lateral Damghan fault between 4 015 000 and 4 020 000 northing (cf. Chap. 1.3.1), which is defined as a branch of the Astaneh fault system, and which is mapped coincide with the fine sediment terrace at the distal alluvial apron.

Between 4 005 000 and 4 010 000 northing, the fluvial plain is structured by a line of slightly elevated fluvial surfaces which is continued by broadly west to east oriented hogback ridges of Miocene marls, in the eastern connection to the fluvial plain. Therefore, a correlation of surface elevation and preservation and tectonic activity in extension of the hogback line is concluded.

Distribution of morphographic and morphometric features

The idea of identifying older surface generations by the characteristics of their enclosing slopes (cf. Schmidt 2009), was related to the discovery of distinct quaternary surface generations in Damghan Basin. Hence, during the morphometrical mapping all slopes were classified, according to GMK5 symbology classes, which has already proven valid for morhogenetically significant slope classes. The spatial relation of slope class polylines and alluvial apron surface polygon boundaries partly represents the relative age model of the quaternary surface generations, as they were determined in the field (Tab. 3.1.3). The Table displays, that e.g. 46 % of all mapped steps are related to the youngest inactive Quaternary surface. The common presumption of a direct correlation of landform size and landform duration can also be observed in the data, which shows increasing slope sizes associated primarily with older surfaces (Tab. 3.1.3; Fig. 3.1.3).

Table 3.1.3: The mapped steps and slopes and the percentage of their connection to distinct alluvial fan and apron surfaces. Principally, the slopes are in contact with at least two surfaces and thus each percentage value represents the contact quantity of one distinct slope and step type with one distinct surface generation.

Mapped landforms (line features)		Map unit properties (% of all features)					
Morphography	Morphometry	Qap1	Qap2	Qap3	Qap4	Qap5	*all Features*
flat slopes	h: 5-20 m w: >10 m	49	0	10	51	100	*27.3*
steep slopes & cliffs	h: 5-20 m & >20 m w: 5-10 m	53	0	2	92	29	*27.7*
step & steep slopes	h: 1-5 m w: 1-5 m & 5-10 m	63	9	34	45	4	*150.3*
steps	h: 0-1 m w: 1-5 m	46	2	9	5	0	*345.7*
all steps and slopes (length in km)		*282.3*	*22.5*	*83.6*	*125.5*	*41.8*	

Source: Own table

Distribution of morphodynamic features

The determination of geomorhologic map units is based on the identification of the type of formative events, that formed a certain landform. This is described in the map units of 'areas of process and structure'. Additional morphodynamic observations about geomorphological processes, mainly direct and indirect observations of active processes, were mapped as specific morphodynamic map units (Fig. 3.1.4) and symbolized in red color (Appendix I). Focus was put again on quaternary map units, particularly on processes which have an additional or apparent effect on the map units. Thus, active rill erosion was primarily mapped, not on abandoned alluvial apron surface generations, where dissection is integral part of overall denudation, but on areas of recent alluvial fan and apron sedimentation. Here, rill erosion typically takes place at distal alluvial apron sections, and within the active depositional lobe. Hence, it represents secondary process of surface material reworking. Sheet wash was identified as secondary process in the transition from slope-fluvial to flu-

vial dominated surfaces and primarily observed in areas where recent slope-fluvial sedimentation of fine sediments took place. Also, aeolian processes of deflation and sand-silt cover accumulation were observed, but the sporadic occurring accumulation patches showed very weak development and were to sparse for valid mapping. Contrary to this, deflation on desert pavements and the occurrence of ventifacts is ubiquitous on older surfaces and therefore not specifically mapped. Finally, evaporation, more precisely the formation of surface evaporites shows clear characteristics in both, the the field and in spectral signals from remote sensing and, thus, could be reliably mapped.

3.2 Description of alluvial apron geomorphology and surface stratigraphy

3.2.1 Prospectional mapping results and findings from stratigraphic fieldwork

The geomorphology of alluvial apron and interleaved fluvial plains in Damghan Basin is dominated by alluvial fan surfaces each with distinct morphodynamic activity, age and cover material. The morphometric variance of surface boundaries, for instance size and morphometry of steps and slopes between surfaces, and spectral surface characteristics led to a chronostratigraphic classification of the map units into two distinct divisions of active alluvial fans and five rather inactive classes of eroded fan surfaces. The sediments were presumed to be of Quaternary age, and precise measurements validating this presumption are provided in Chapter 3.4.

GPR-Prospection – The lateral and vertical extent of Quaternary sediments

All GPR (Ground penetrating radar) measurements bore the challenge that detailed sediment layering was almost un-detectable. This may be a result of the matrix dominated, fine grained structure of the sediments and the interfingered gravel lenses in the distal profiles. The signal scattering and absorption largely prevented valid measurements and the identification of a solid reflector.

Despite these complications the radargrams showed few considerable reflections within the fine sediments, located at the alluvial apron's distal end (Fig. 3.2.1), which are presented below. The overall signal properties of the alluvium showed little variation. From the comparison of radar signals from different antennas and the known layering in the excavated profiles an overall medium velocity of 0.11 m/ns was determined. It comprises combined velocities of sandy-silty layers and of clast rich alluvial debris layers, which are closely interleaved, and was applied to all radargrams.

Longitudinal (A-A') and cross (B-B'2) profile measurements with the 200-MHz-antenna at the distal end of the alluvial apron (Figure 3.2.2) showed considerable sediment structures of the fine sediments. In longitudinal direction, there was no reflector in greater depth detected, but a strong reflector could be measured in about

100 cm depth, at higher elevated sections. It shows a rough, heterogeneous, surface clearly contrasting the smooth signal in hanging layers. Between 60 and 135 m profile distance this reflector sinks down to over 200 cm depth, and is then replaced in the 0-60 m profile section by a less tilted reflector. The 60 m distance mark coincides with the apex of the alluvial fan, which has developed below the fine sediments. Hence, the reflector in the 0-60 m section can be regarded as individual alluvial fan deposits.

The cross profile reveals a distinct, grainy radar texture in several channel fill like forms at the very top of the channel bottoms, with a depth of maximal 60 cm. Below this the rough reflector surface in 100 cm depth from the channel bottom can be observed as described before. Again its extent is limited to the channel floor. Two additional reflectors appear in the radargram, at a total depth of mainly 600 and 700 cm. The reflectors are whether parallel to the relief nor horizontal, but are sloping in

Figure 3.2.1: Overview of the GPR-profiles described in this study.

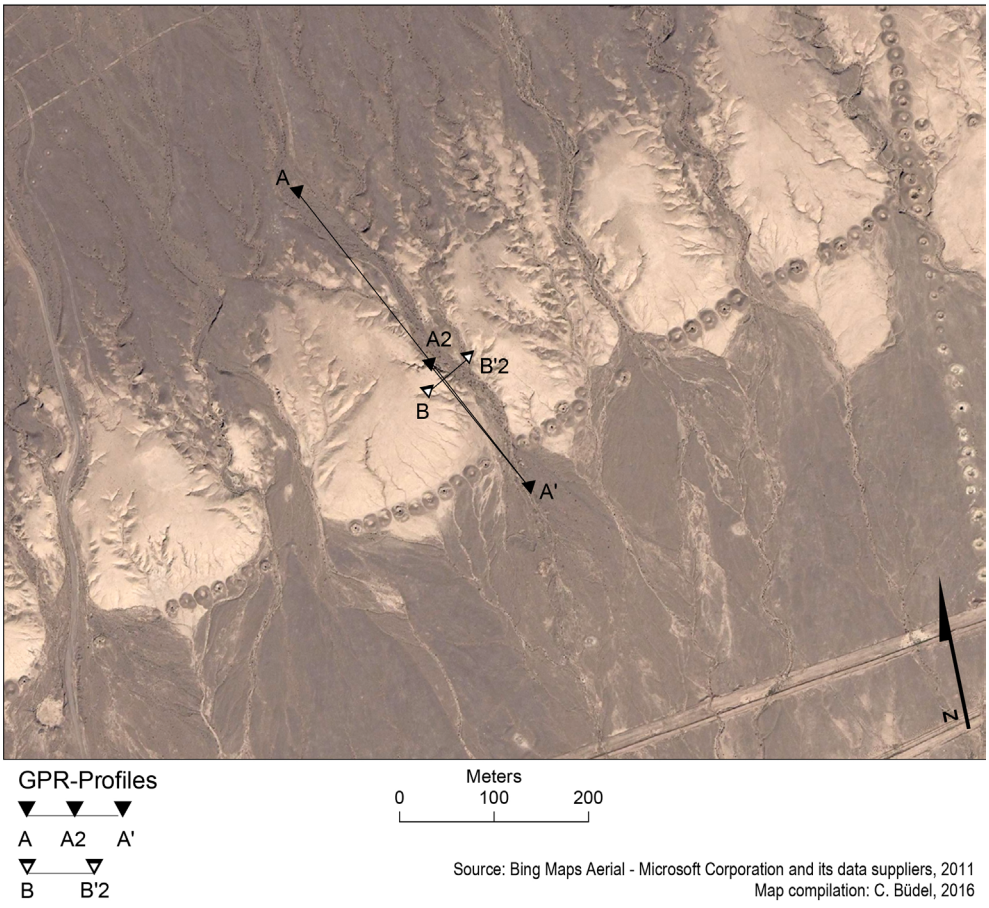

Figure 3.2.2: (A) 200-MHz-antenna, Data 249, profile A-A'-longitudinal profile of fine sediments at distal end of alluvial apron shows detailed internal structure in shallow depth. (B) 200-MHz-antenna, Data 251, profile B-B'2-cross profile of the same fine sediments, shows internal structure in shallow depth, as well as two reflectors in mainly 600 and 700 cm depth, diving down to 1 000 cm and shaping channel form structures.

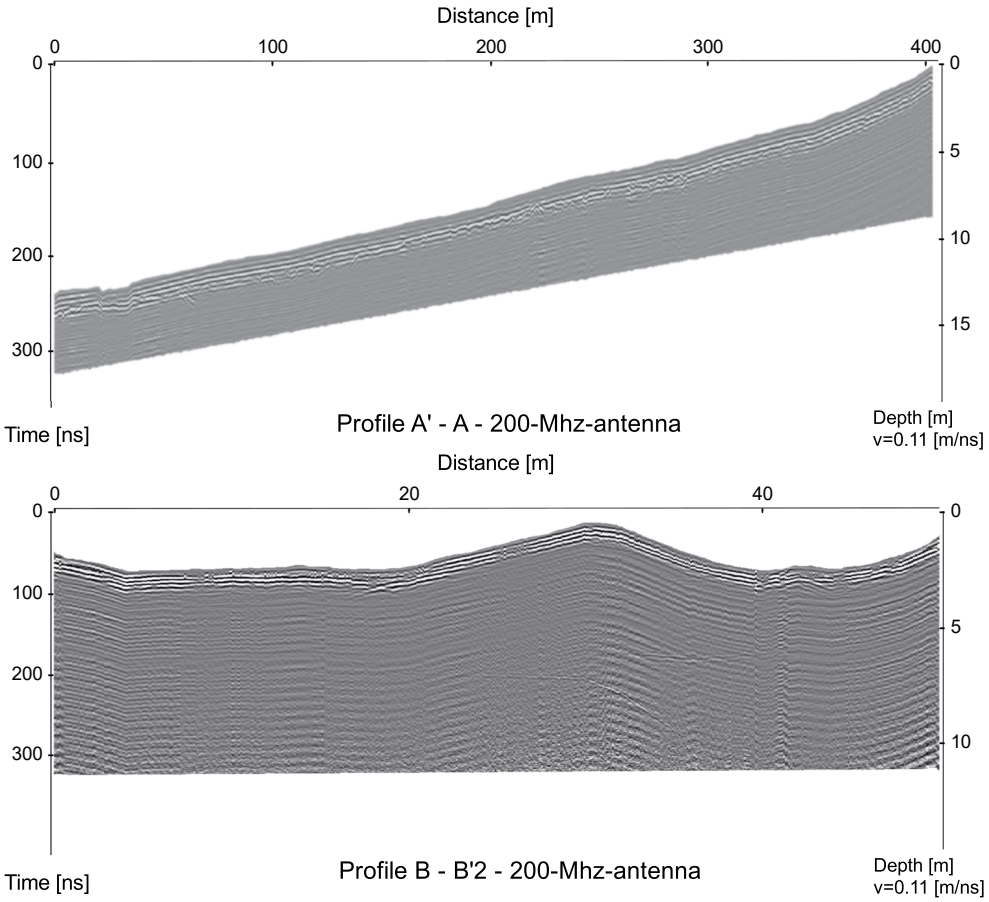

Source: Own illustration

channel form like shapes down to a depth of 1 000 cm, where their signal gets lost. Their smooth and specific channel surface is not correlating with any bedrock observations in the area and is therefore regarded as a potential signal of buried channel surfaces.

Signals in 250-MHz-antenna measurements show more detailed reflectors and allow to distinguish three major reflector layers coincide with several smaller intercalated reflectors, supposedly related to gravel-bars or lenses, which had been observed in the field (Fig. 3.2.3). A major finding in this measurement is the potential signal of the Damghan Fault (Chap. 1.3.1). It may be indicated by a row of reflectors between 108 - 126 m profile distance. They are inclined at about 6° to the south and they are clearly cutting all other reflectors in the scene. Even the reflectors representing the youngest layers in the near subsurface are disturbed by this anomaly.

Figure 3.2.3: 250-MHz-antenna, Data 269, profile A'-A2-Radargram of Q^{al}_0 prograded alluvial fan shows a disturbance in layering between 108-126 m.

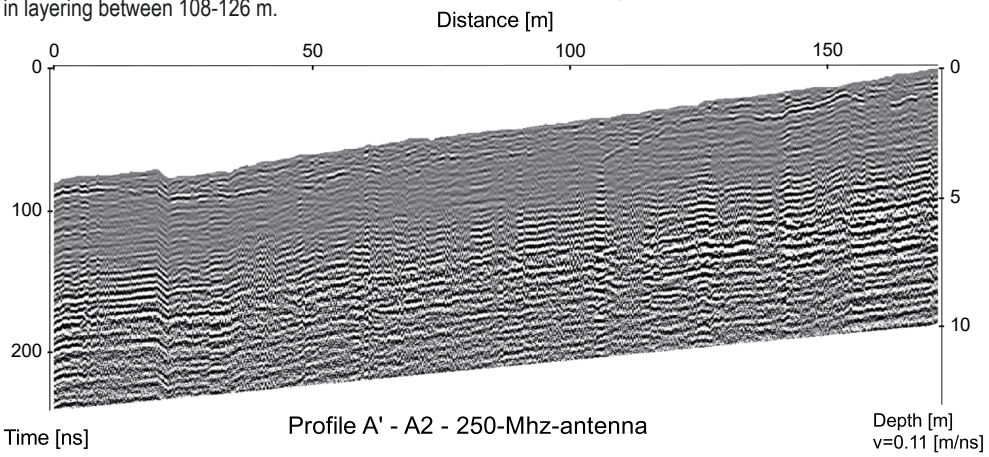

Source: Own illustration

Alluvial fan surfaces and processes

The alluvial fan surfaces materials showed characteristics depending from the varying degree of weathering. Consequently, un-weathered active surfaces are dominating the young alluvial fans or the surface within active depositional lobes (ADL) of the alluvial apron. These active surfaces are covered by un-weathered fluvial or slope-fluvial deposits or are slightly aged, with initial desert pavement and young yermic horizons. Distinct layers of additional activity phases discordantly cover older, weathered layers. Ongoing aggradation and surface sediment reworking are supposed to shape these layers of separate activity phases. The layers frequently show total thicknesses between 65 and 80 cm (Sections: S03-C-I, -C-II and -D-I) and they can cover older fan surfaces, which bear a fossil soil horizon (Fig. 3.2.4). In contrast to this, the observed inactive surfaces typically feature incised slopes from an autochthonous drainage. This forms a dendritic system of shallow saucer-shaped headwater channels and deeper incised v-shaped channels in the course of the flow. Desert pavements and soils develop on the inactive surfaces and shallow channels, while rill erosion and mass movement controls the steeper valley flanks and undercut banks, which bear colluvial layers of widely varying size and structure.

From stratigraphic field descriptions of the near subsurface of different alluvial fan surfaces, increasing depth of gypsic horizons with decreasing relative age can be inferred (Fig. 3.2.4). In $Q^{ap}1$ and $Q^{ap}2$ fossil gypsic horizons are partly eroded and thus covered by discordant layers of alluvial debris. A calcic horizon was also observed in the field, which has developed within the surface substrate and is covered by a stone pavement, with 0.5 mm thick desert varnish, that very occasionally

increases to up to 2 mm thickness. The initial cambic horizon of $Q^{ap}2$ features a more reddish and yellowish hue, which coincides with the field observation of lepidocrocite bearing limonite and hematite precipitates. The precipitation of this minerals can indicate carbonate solution (Scheffer et al. 2010).

Pictures 3.2.1: Alluvial fan surface $Q_{ap}5$ has a well-developed gypsic horizon with beard-shaped gypsum crystals of up to 14 cm in length; the right picture shows the excavated gypsum-beards (scale in cm; Pictures: C. Büdel, 2011).

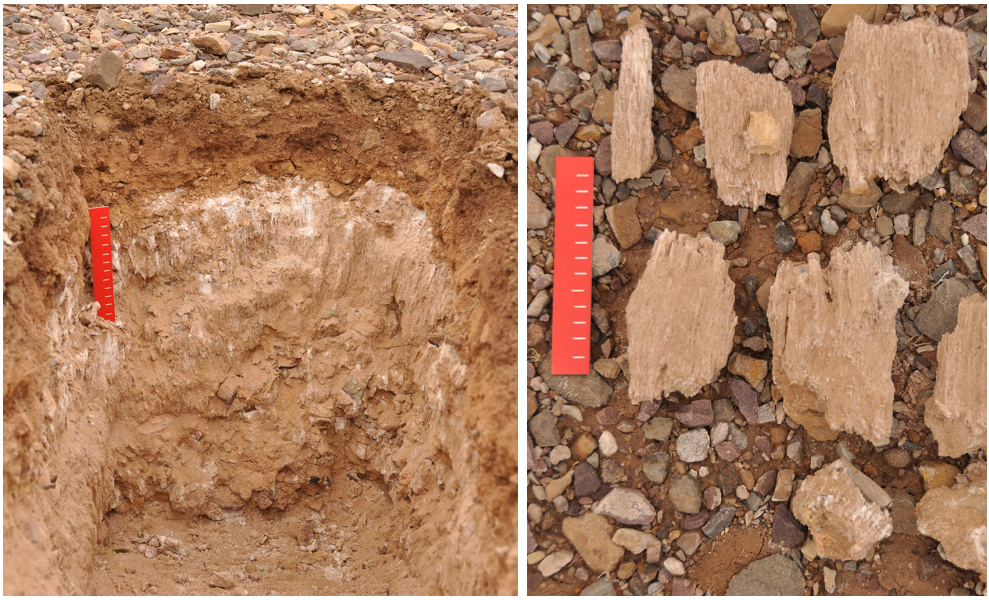

Source: Own photographs

In contrast to this, the older surface – Qap5 – shows high gypsum contents throughout the profile and the gypsic horizon in footwall layers of the stone pavement features gypsum crystals of up to 14 cm in length (Pic. 3.2.1). The depth of this gypsic horizons is supposed to be proportional to an increase in rainfall, resulting in deeper gypsic horizons where rainfall is high (Goudie 2013). In case of the observed profiles in Damghan, precipitation and gypsic horizon depth show an opposite correlation. Here, precipitation declines southwards towards a central playa, while gypsum depth increases. Also, sources for sulphide or anhydrite minerals are essential for gypsum distribution on the alluvial apron and gypsum-rich Miocene sediments cover wide areas of the basin. At this point, data are too limited for drawing any further assumptions.

A yermic, gypsic calcisol was recorded in $Q^{ap}2$-4 and well developed calcaric, cambic leptosol in $Q^{ap}1$ (Fig. 3.2.4 and Tab. 3.2.1). Drainage from $Q^{ap}2$ and older surfaces already has shaped flat-floored, v-shaped valleys wider than 25 m that are covered by young fluvial reworked sediment. Younger surfaces typically feature smaller saucer-shaped drainage ways and smoothly undulating surfaces with ridges tracing debris flow lobes. Younger surfaces are bounded by steps of about 1 m height

and 1-5 m depth while older alluvial sediments are separated from the younger by steep slopes, roughly 1-5 m high and 5-10 m wide.

The clast analysis data from surface $Q^{ap}1$ at S03-C-II and $Q^{al}1$ at S03-B-II describes the changing clast characteristics with increasing transport distance (Tab. 3.2.1). Decreasing clast sizes, together with increasing amount of rolled edges is related to the longer transport distance downslope the alluvial apron. Contrary to this, the field indications of weathering, in particular rock hardness and weathering rind thickness, are ambiguous. With bigger rind thickness at the harder clasts of S03-B-II.

Figure 3.2.4: Sediment logs of eroded alluvial fan surfaces.

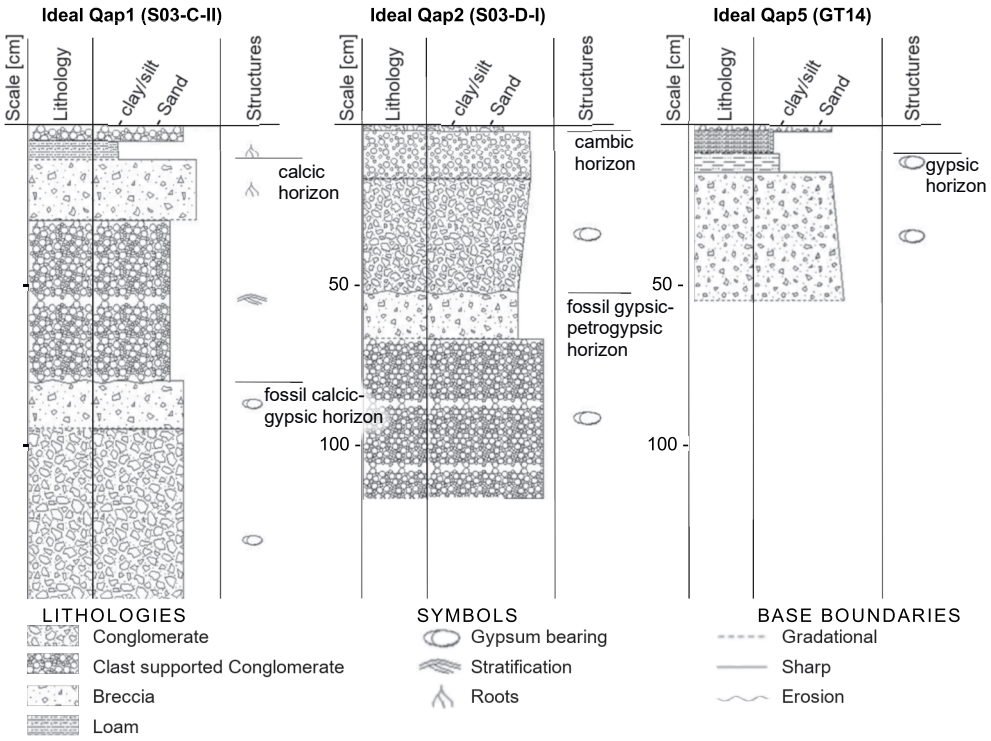

Source: Own illustration

Table 3.2.1: Clast analysis data shows typical characteristics of increased transport distances from medial (S03-C-II) to distal (S03-B-II) area of the alluvial fan, while indications of weathering are ambiguous.

Site no.	L / I / E (mm)			r_{max} / r_{min} (mm)		rounding (1-4)	rolling (%)	hardness (1-5)	rind (mm)	Ie (2r/L x 1000)
S03-C-II	**108.1**	**51.5**	**31.1**	**708.3**	**2.7**	**1.2**	9.3	2.8	0.8	13 103
S03-B-II	72.2	42.1	20.1	514.0	2.2	1.1	**23.9**	**4.0**	**1.1**	**14 246**

Measures & Values (n=36): L = Length; I = width; E = thickness; rmin & rmax measured along L; L-restriction = 50 - 150 mm; Ie = 2r/L x 1000 (Method: Leser 1977)

Source: Own table

Figure 3.2.5: The maps show relationships between mapped landforms (e.g. chronostratigraphic units) and typical spectral characteristics of their surfaces (from Büdel et al. 2017). Note the different characteristics of S03-B-I to B-II, which describe at least two generations of young distal alluvial fans ($Q^{al}0$ & $Q^{al}1$) and thus represent two distinct relative ages. Sites at sections S03-C-I and -C-II embody surfaces of different ages ($Q^{al}0$ & $Q^{ap}1$) in the mid-fan-area. Their spectral properties clearly distinguish relative ages and provenances of the sediments. Finally, S03-D-I is placed in eroded alluvial fan sediments ($Q^{ap}2$) and also represents sediments of different composition. Today, profiles are part of the same alluvial apron section, fed by a distinct watershed. Hence, the lithologic composition or the extent of the watershed has changed over time.

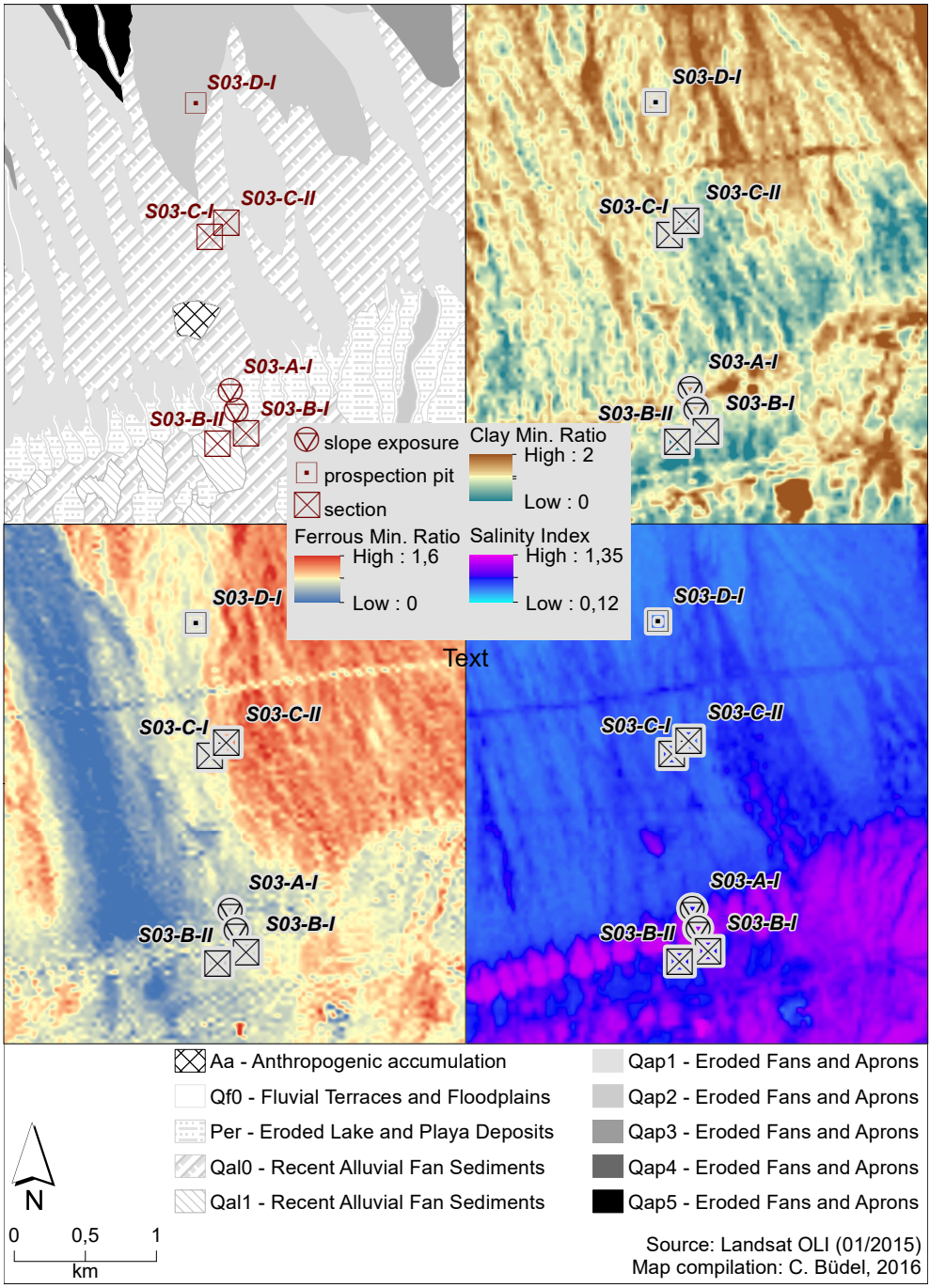

Spectral properties

Spectral properties of the alluvial fan surfaces are presented in figure 3.2.5 (cf. Büdel et al. 2017). The extent of previously recorded distinct degrees of surface weathering at selected sites in the field was reliably detected by the *clay minerals ratio*. In this case, the clay minerals ratio supports the mapping of different relative ages on the hummocky undulating alluvial apron surface.

Contrasting this, the *ferrous minerals ratio* creates apparently different patterns and does not show sensitivity for surface weathering. According to its sensitivity for iron bearing minerals, it distinguishes alluvial fan surfaces of different lithological provenance or composition. All described sections are part of the same alluvial apron segment, and fed by a distinct watershed. Hence, the lithologic composition and/or the extent of the watershed has changed over time, causing the twofold spectral signature of ferrous minerals ratio in the investigation area. The surface salinity is highly variable and easily altered by surface water. Therefore, the *salinity index* is not in line with the Mg/Ca-ratio, as derived from geochemical analysis (Table 3.2.10). All salinity data derived from selected sections are limited regarding their representability for all joined map units.

3.2.2 Detailed field descriptions of the sections

The detailed stratigraphical and lithological field investigations of the seven specific sections from key localities of the alluvial apron (Fig. 3.2.6) provided a comprehensive insight into its youngest sedimentation history. The recent to fossil soil horizons were documented and significant layers of debris flow and fluvial facies sedimentation were identified as evidence for slope-fluvial moprhodynamics, which are constituting the alluvial fans formative events. Two groups of abandoned surfaces characterize the alluvial apron. The first group is partly eroded or covered by active secondary process layers ($Q^{al}0$ & $Q^{al}1$-2), while recent to sub-recent alluvial fan accumulations constitute the second group ($Q^{al}0$-1). All described layers from these groups were sampled and could be precisely characterized later in the laboratory (Chap. 3.2.3).

$Q^{al}0$, $Q^{ap}1$-2 – Eroded alluvial fan and apron sediments at S03-D-I and S03-C-I & -II

Sediments from the higher elevated proximal and medial segments of the alluvial apron were studied at three sections at 1 238 (S03-D-I) and 1 196 (S03-C-I & -II) m a.s.l. They are representatives of three mapping units, with *S03-C-I* for $Q^{al}0$, *S03-C-II* for $Q^{ap}1$ and *S03-D-I* for $Q^{ap}2$. Though, facies identified in a section also occurred in the section of other map units, and hence facilitated a better integration of sediment stratigraphy.

The *S03-D-I* section was prepared from an extended prospection pit, dug in the slope of an incised valley in $Q^{ap}2$ "four" layers had been defined and described in the section (Tab. 3.2.2). These are primarily clast-supported layers of debris, with a

Figure 3.2.6: Section sites with main landscapes at the alluvial apron.

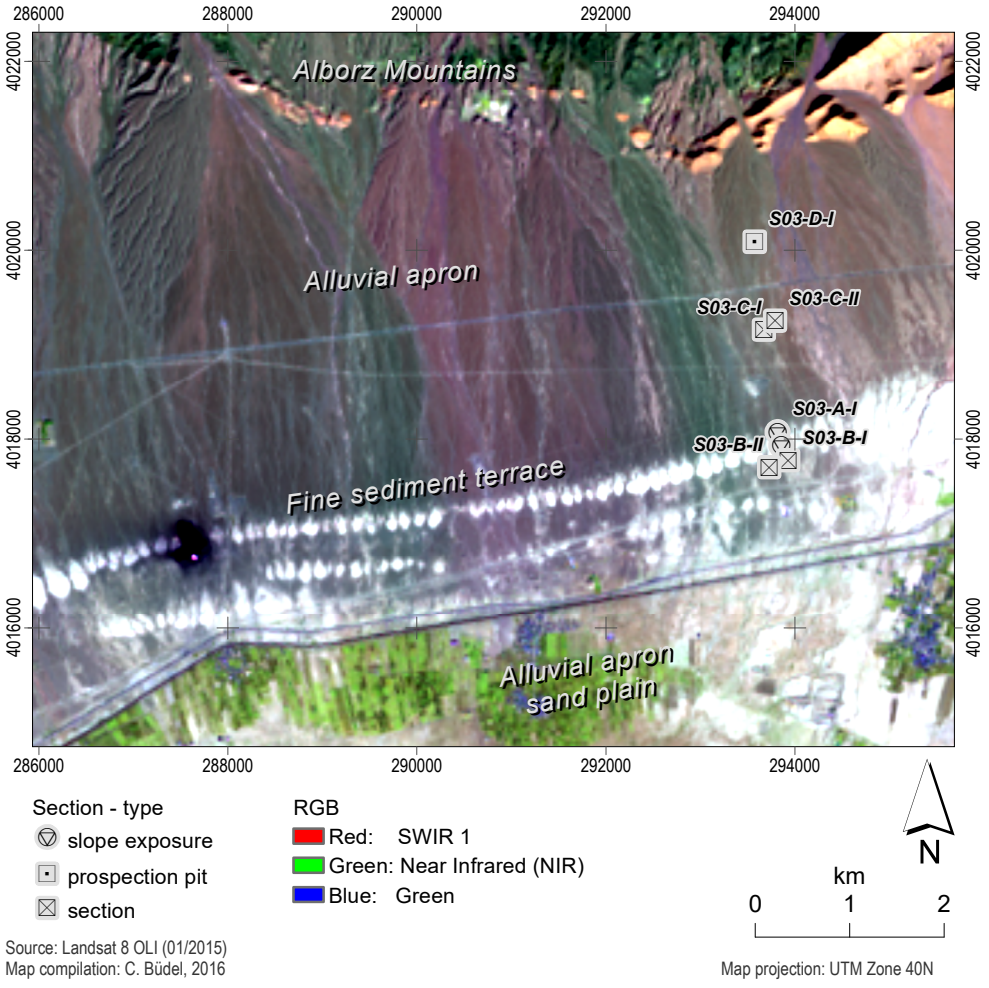

matrix of silty loam to very loamy sand and varying amounts of coarse clasts. The layers show matrix and clast supported structure with up-coarsening clast sizes, which is typical for high energy debris flow deposition. The degree of carbonate cementation is medium to strong in the lower half of the section, and weak cementation is still apparent in the upper section. Two of the debris flow lobes are altered at their surface by developed soils. The recent soil horizons are developed beneath a stone pavement and show indications of a yermic, gypsic calcisol, with a calcic horizon of up to 50 cm depth and gypsum evaporite bearing. The medium to strong cemented gravels in 50 and 65 cm depth bear a petro-gypsic horizon (layer 3), supposedly fossil and thus representing a former surface.

Table 3.2.2: The layer properties of section S03-D-I.

Section S03-D-I: Field description of layers								*slope exposure – 1 238 m a.s.l.*
Layer	depth (cm)	layer description	contact to lying layer	Color (Munsell)[4]	Texture / structure	consolidation[1]	evaporites[2]	root density[3]
1	0 - 15	yermic, cambic A-horizon loamy debris flow gravel under desert pavement	sharp	brown, pink (5 YR 7/4)	silty loam with stones and gravel; unsorted	2 loose	2 weak	3 medium
2	15 - 50	debris flow lobe	sharp; erosional	whitish grey, pink (5 YR 8/3)	stones and gravel with loamy-silty sand; unsorted	3 medium	5 very strong	1 very weak
3	50 - 65	fossil petro-gypsic B-horizon in debris flow lobe	diffuse	red brown, pink (5 YR 7/4)	pebbles and gravels with very few stones and very loamy sand; unsorted	4 solid	2 weak	0 no roots
4	65 - 115+	cemented debris flow lobe with stones and gravel	*(buried)*	brown grey, pink (5 YR 7/4)	gravels and stones with loamy-silty sand; unsorted	4 solid	5 very strong	0 no roots

[1]degree of consolidation: 1-5 - [2]degree of macroscopic evaporite density: 0-5 - [3]degree of root density: 0-5 (Ad-hoc-AG Boden 2005); [4]Munsell Color 2009

Source: Own table

Section *S03-C-II* cuts the mid-fan surface of $Q^{ap}1$ to a depth of 160 cm. Five layers were defined (Tab. 3.2.3), comprising deposits from two debris flow events in layer 1-2 and 3. The debris flows texture in layer 1 and 2 is characterized by clast supported stones and gravels in a matrix of silty loam to very loamy sand. The surface is covered by a stone pavement with a grey-brown yermic A-horizon. The sorting is reduced to an unsorted bottom texture of coarse clasts and a matrix supported top, still unsorted but with considerably decreased clast content. The debris flow constituting layer 3 is part of an intercalation of gravels and pebbles, where the debris event unit is characterized by its matrix supported clasts and up-coarsening sorting of coarse gravel and scattered stones. Thus, it can be regarded as a remain of the event with the highest magnitude within this sequence of alluvial processes. Layers 4 and 5 proved to be solid and showed calcium and gypsum evaporites in between gravels and stones. Layer 4 shows signs of surficial erosion and bears indications for a red-brown calcic-gypsic horizon, which is supposed to be fossil since it was covered by the younger alluvium.

The mid-fan surface at 1 196 m altitude was also investigated at a section excavated in sediments categorized as map unit $Q^{al}0$. These are most recent alluvial fan sediments, which have not yet been reshaped by erosion and which are most recently formed by active transportation and accumulation. Section *S03-C-I* was excavated to a depth of 160 cm and a width of 583 cm. A total of 6 layers was defined (Tab. 3.2.4), with three of them covering the full lateral extent of the section and 3 layers laterally terminating within the section, at least at one side. A seventh area, covering a minor part of the section could not be described, properly.

The surface layer (layer 1) is a clast-supported fluvial or alluvial sediment, which showed few signs of distinct layering or sorting. The surficial brown color of the

Table 3.2.3: The layer properties of section S03-C-II.

Section S03-C-II: Field description of layers								*excavator trench – 1 196 m a.s.l.*
Layer	depth (cm)	layer description	contact to lying layer	Color (Munsell)[4]	Texture / structure	consoli-dation[1]	evaporites[2]	root density[3]
1	0 - 6	yermic A-horizon	diffuse	grey-brown (5 YR 8/3)	silty loam with, pebbles and gravels and very few stones; unsorted	1 very loose	0 no evapo-rites	3 medium
2	6 - 25	calcic B-horizon in clast-rich debris flow	diffuse	brown (7,5 YR 7/4)	gravel and stones with very loamy sand; unsorted	1 very loose	0 no evapo-rites	2 weak
3	25 - 75	debris flow bedded in sorted gravels	sharp; erosional	grey (5 YR 7/3)	mainly rounded gravels with silty sand; well sorted	1 very loose	0 no evapo-rites	0 no roots
4	75 - 90	fossil calcic, gypsic B-horizon in cemented layered gravels	sharp	red-brown (5 YR 7/5)	rounded gravel with stones and very silty sand; very well sorted	4 solid	2 weak	0 no roots
5	90 - 160+	cemented and tilted layered gravels and debris	*(buried)*	grey (5 YR 8/4)	alternation of rounded gravels with stones and loamy sand; unsorted to well sorted, tilted	4 solid	2 weak	0 no roots

[1]degree of consolidation: 1-5 - [2]degree of macroscopic evaporite density: 0-5 - [3]degree of root density: 0-5 (Ad-hoc-AG Boden 2005); [4]Munsell Color 2009

Source: Own table

Table 3.2.4: The layer properties of section S03-C-I.

Section S03-C-I: Field description of layers								*excavator trench – 1 196 m a.s.l.*
Layer	depth (cm)	layer description	contact to lying layer	Color	Texture / structure	consoli-dation[1]	evaporites[2]	root density[3]
1	0 - 30	A-Horizon in fluvic material	diffuse	brown	pebble and debris with loamy sand; unsorted	1 very loose	2 weak	3 medium
2	30 - 50	pebble and gravel in channel fills	sharp	grey	mainly rounded, layered gravels with few pebbles and silty sand; very well sorted	2 loose	1 very weak	1 very weak
3	45 - 75	unsorted debris flow with big clasts	sharp	yellow-grey	coarse stones and pebble with very silty sand matrix; unsorted	1 very loose	0 no evapo-rites	0 no roots
4	70 - 130	well sorted and tilted stratified gravels	sharp; erosional	grey	tilted (~18°) stratified, rounded and angular gravels with silty sand; very well sorted	3 medium	0 no evapo-rites	0 no roots
5	90 - 140	fossil calcic, gypsic B-horizon in cemented layered gravels; layer thikness max 15 cm	sharp	red-brown	stratified, rounded and angular gravels and pebble with very loamy sand; in unsorted to well sorted strata	4 solid	2 weak	0 no roots
6	90 - 160+	cemented layers of gravels	*(buried)*	yellow-grey	Stratified pebbles and gravel, sometimes rounded with loamy sand; in unsorted to well sorted strata	4 solid	2 weak	0 no roots

[1]degree of consolidation: 1-5 - [2]degree of macroscopic evaporite density: 0-5 - [3]degree of root density: 0-5 (Ad-hoc-AG Boden 2005)

Source: Own table

loamy sand matrix indicates an initial A-horizon. Layer 2 features strong evidence for fluvial transportation, such as rounded grains, trough-cross-bedding and distinct layers of very well sorted, one sized gravels. Predominantly rounded and sub-rounded gravels had also been observed in layers 4 and 5, where layer 4 showed tilted gravels and appropriate sorting properties, typical for lateral accumulation. Alluvial fan morphodynamics are represented by layer 3 which is constituted by sediments with distinct debris flow properties. Stones and pebble in this layer are clast-supported, unsorted and show bigger grainsizes, within a matrix of very silty sand. In Layer 5 and 6 lower degrees of sorting together with bigger grain sizes compared to the other fluvially stratified layers had been observed. Layer 5 has a red-brown color and some evidence for a calcic-gypsic B-horizon.

Figure 3.2.7: Drawing of sections S03-C-I & -II (bottom right) and S03-D-I (bottom left).

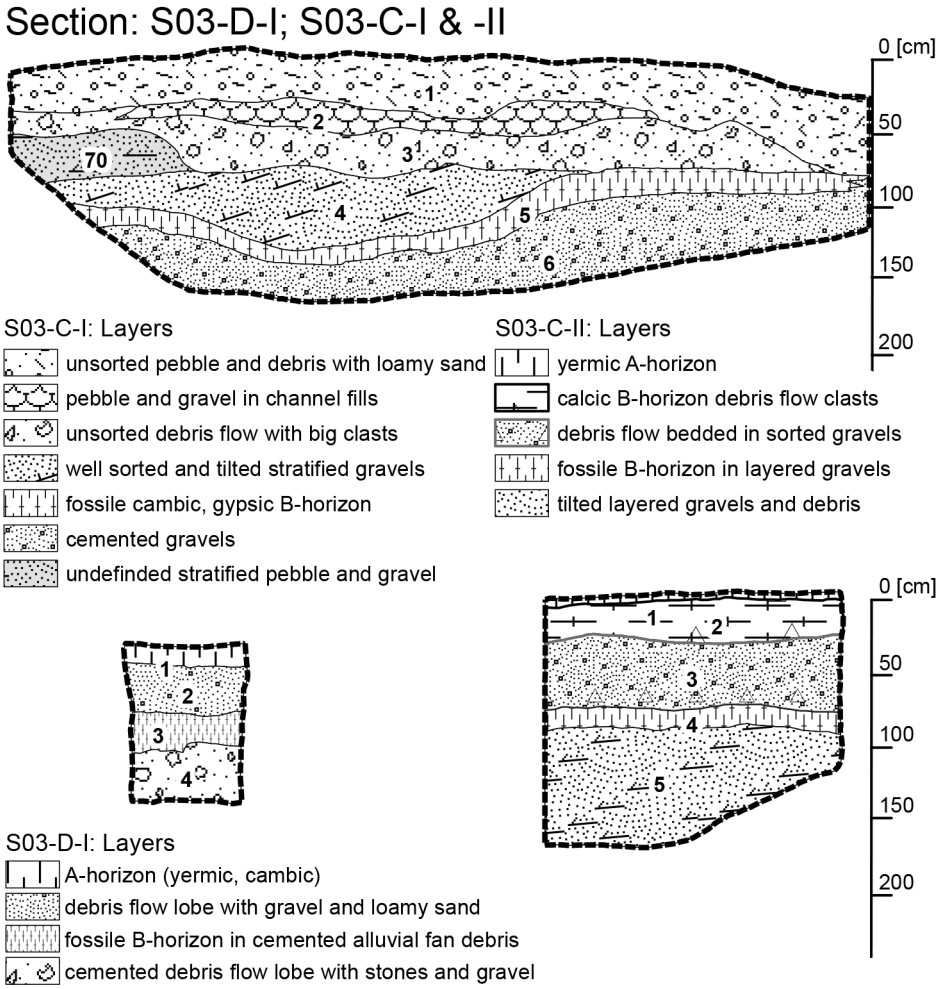

Source: Own illustration

Figure 3.2.8: Drawing of Sections S03-B-I & -II. Map unit $Q^{al}0$ is represented by S03-B-I and the stratigraphy of $Q^{al}1$ is described by S03-B-II. Legend entries are ordered according to their layer description tables.

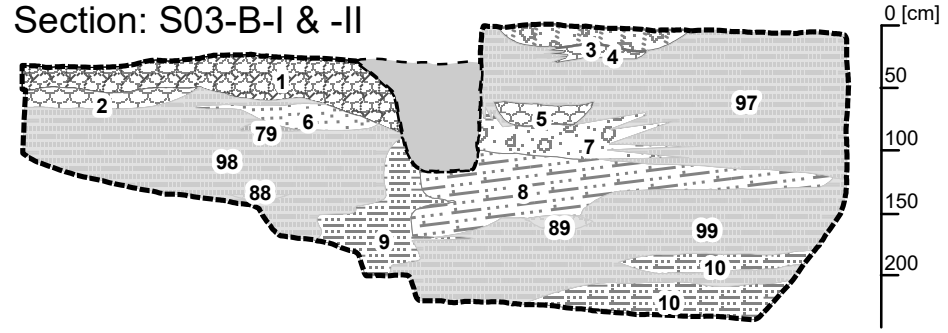

S03-B-I: Layers

- debris flow cover, no alteration
- channel fill, fine sand with gravel
- unsorted gravel and pebble
- channel fill with medium sand
- pebble and gravel in channel fill
- stratified gravels and sand
- debris flow sediments
- tilted, stratified pebble with sand
- silty-sand sediments
- silty-sand with gravel lenses
- undefined channel fill
- undefined gravels and pebbles
- undefined layerd gravel

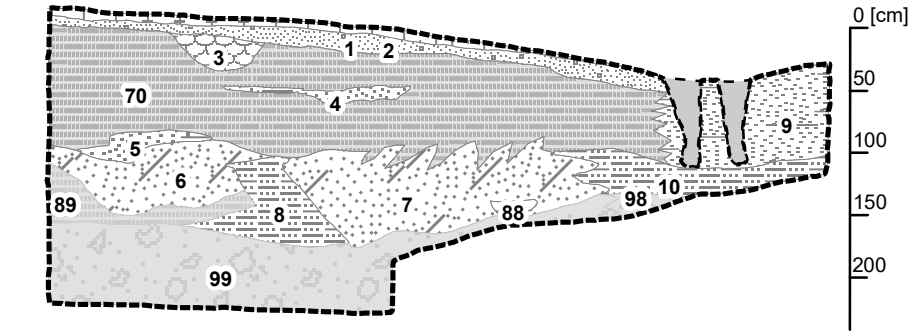

S03-B-II: Layers

- yermic A-horizon
- unsorted sand and pebble
- channel fill
- interlayered gravel
- tilted, stratified gravels and sand
- 2-layered gravel and sand
- 3-layered gravel and sand
- channel fill with loamy sand
- silty-sandy sediments
- silty sandy fines
- undefined layered gravel
- undefined layered gravel and pebble
- undefined cemented fanglomerat

Source: Own illustration

$Q^{al}0$-1 – Recent to Subrecent alluvial fan accumulation at S03-B-I & -II

The distal end, or the toe area, of the alluvial apron is occupied by rows of small alluvial fans. They are all located at about the contour line of 1 150 m a.s.l., and they connect the alluvial apron to the fluvial plain, which expands below this fan line. The alluvial aprons fan toes are terminating in a straight line of fine sediments (P^{er}), as described above and in chapter 3.3. These fine sediments and the alluvial debris from higher elevated sections of the apron are eroded and transported alongside the incised channels until they become re-deposited in the succession of small alluvial fans. Different surface characteristics divide the small alluvial fans in two groups of recent (map unit: $Q^{al}0$) and sub-recent (map unit: $Q^{al}1$) alluvial sedimentation. Section *S03-B-II* gives detailed information about the near-subsurface stratigraphy of $Q^{al}1$, and section *S03-B-I* reveals the stratigraphy of $Q^{al}0$ (Fig. 3.2.8; Pic. 3.2.2).

Section *S03-B-II* is located at 1 140 m a.s.l. in the proximal to medial area of an alluvial fan classified to map unit $Q^{al}1$ – sub-recent alluvial fan activity. It incorporates a cross-sectional profile of the fan, beginning at the active channel and extending 626 cm in direction to the fans central line. It was excavated to a depth of 220 cm, primarily revealing the indifferent inner structure of the sub-recent alluvial fan depositional lobe (Tab. 3.2.5). Due to the indifferent layering, in total 10 distinct layers could be determined, leaving 55 % of the section undefined and without valid field description. Therefore, sampling and data interpretation was partly restricted to the principals of equidistant analyses.

Pictures 3.2.2: Section S03-B-II after a thunderstorm eroded the right handed wall (Picture: C. Büdel, 2011).

Source: Own photograph

The surface layer is represented by a stone pavement with a yermic A-horizon. A cambic B-horizon is clearly distinguishable from the A horizon and both are developed in unsorted debris flow or debris-flow-like sediments. Characteristics of the main alluvial fan body are represented and described by the layers 4, 5 and 9 in the upper section part and layers 6 and 7 in the lower part. While the upper layers feature stratified rounded mostly fine gravels with good sorting, the lower part of the section is dominated by less sorted, coarser and angular gravels and pebbles with tilted stratification. In addition, the lower part of the section is more consolidated and evaporites are more common. Though, the highest amount of evaporites was observed at the surface – layer 1, and in the sands of a small channel fill close to the surface – layer 3. The stratified and tilted gravels of layers 6 and 7 are interfingered with fine sediments of almost entirely very silty sands from layers 8 and 10. These show medium consolidation and bear a considerable amount of evaporites. The section is based on strongly consolidated, unsorted debris flow sediments, which could not be excavated and investigated to an appropriate depth.

Table 3.2.5: The layer properties of section S03-B-II. Layers are ordered by vertical extent and depth.

Section S03-B-II: Field description of layers								*excavator trench – 1 140 m a.s.l.*
Layer	depth (cm)	layer description	contact to lying layer	Color (Munsell)[4]	Texture / structure	consolidation[1]	evaporites[2]	root density[3]
1	0 - 4	Yermic A-horizon in debris flow	diffuse	*no data*	coarse pebble with gravel in very loamy sand; unsorted	1 very loose	3 medium	*no data*
2	4 - 14	Cambic B-horizon, in unstructured sand and pebble	diffuse	*no data*	loamy sand with few gravel and stones; unsorted	2 loose	0 no evaporites	*no data*
3	14 - 35	channel fill sediments	sharp	*no data*	very loamy sand with few gravel; very well sorted	1 very loose	3 medium	*no data*
9	30 - 110	interlayered gravels	sharp	*no data*	alternating well to weak sorted layers of rounded fine and medium gravels with sand	0-1 very loose	2 weak	*no data*
4	~50 - 60 (lense)	lense with stratified gravels in 2 phases	sharp	*no data*	rounded gravel and very silty sand; very well sorted	0-1 very loose	0 no evaporites	*no data*
5	~90 - 110 (lense)	lense with stratified gravels in 3 phases	sharp	*no data*	rounded and few angular gravels and silty sand; well sorted	0-1 very loose	0 no evaporites	*no data*
6, 7	100 - 150	tilted, stratified gravels and sand	diffuse	*no data*	well sorted rounded gravel interlayered with unsorted angular gravel and stones in silty sand	2 loose	1 very weak	*no data*
8, 10	100 - 180	silty-sandy fine sediments, unstructured	sharp	*no data*	very silty sand with few gravel; very well sorted	3 medium	2 weak	*no data*

[1]degree of consolidation: 1-5; [2]degree of macroscopic evaporite density: 0-5; [3]degree of root density: 0-5 (Ad-hoc-AG Boden 2005); [4]Munsell Color 2009

Source: Own table

Most recent alluvial fan activity is represented in map unit $Q^{al}0$, and for the situation of the small alluvial fan succession this unit was investigated in *S03-B-I at 1 140 m a.s.l*. The section covers a cross sectional profile of one of those fans in proximal to medial area and extents from the active depositional lobe 663 cm to a close slightly elevated surface in direction to the fans central axis. 10 layers were determined from this section which describe 40 % of the section area (Tab. 3.2.6). 60 % are left undefined, only represented by selected layers for equidistant analysis, as it is already explained above regarding section S03-B-II.

The young surface at this section is covered by layers 1 and 3, representing debris flow gravels and stones and fluvial gravel and pebble, both without any evidence of alteration. The main body of this alluvial fan is constituted by channel fills – layer 2, 4, 5, and fluvially stratified gravels and sands, partly tilted in the lower half of the section – layer 8. A high energy event is recorded in the sediments of layer 7, that shows unsorted, clast supported gravels and pebbles from at least one debris flow event. Evaporite bearing is restricted to deeper, stratified and coarser sediments, as well as to the yellow-brown fine sediments, which occur in layer 9 and 10. These are similar to the very silty sands from section S03-B-II and like in that section, again they are intercalated with stratified tilted pebbles and gravels – represented by layer 8.

Table 3.2.6: The layer properties of section S03-B-I. Layers are ordered by vertical extent and depth.

Section S03-B-I: Field description of layers								*excavator trench – 1 140 m a.s.l.*
Layer	depth (cm)	layer description	contact to lying layer	Color (Munsell)[4]	Texture / structure	consolidation[1]	evaporites[2]	root density[3]
3	0 - 20	debris flow cover, no alteration	sharp	brown, pinkish grey (5 YR 7/2)	unsorted gravel with stones in silty sands	0-1 very loose	0 no evaporites	3 medium
4	20 - 30	channel fill, fine sand with gravel	sharp	yellow-red-brown, pink (5 YR 7/4)	silty sands and rounded gravel; very well sorted	0-1 very loose	0 no evaporites	2 weak
1	30 - 50	unsorted gravel and pebble	diffuse	yellow-brown, pink (5 YR 6/4)	weakly sorted rounded and angular gravel and pebble with coarse sand	0-1 very loose	0 no evaporites	1 very weak
2	50 - 65	channel fill with medium sand	sharp	yellow-dark-brown, pink (5 YR 7/3)	medium sands with fine gravel; very well sorted	0-1 very loose	0 no evaporites	1 very weak
5	60 - 80	pebble and gravel in channel fill	sharp	red / brown / yellow (no Munsell)	layered rounded and angular gravel in sands; well sorted	0-1 very loose	0 no evaporites	0-1 very weak
6	~65 - 75 (lense)	stratified gravels and sand	diffuse	red / brown / yellow (no Munsell)	layered rounded and angular gravel with few sand; medium sorted	1 very loose	2 weak	0-1 very weak
7	80 - 100	debris flow sediments	diffuse	yellow-brown, pink (5 YR 6/4)	unsorted, clast-supported gravel and pebble with stones and silty sand	0-1 very loose	2 weak	2 weak
8	95 - 175	tilted, stratified pebble with sand	diffuse	yellow-brown, pink (5 YR 6/4)	coarse gravel and pebble interleaved with fine gravels and sand; weakly sorted	1 very loose	1 very weak	1 very weak
9, 10	90 - 220+	silty-sandy sediments	diffuse	yellow-brown, pink (7,5 YR 7/3)	very silty sand with few gravel; very well sorted	0-1 very loose	2 weak	0 no roots

[1]degree of consolidation: 1-5; [2]degree of macroscopic evaporite density: 0-5; [3]degree of root density: 0-5 (Ad-hoc-AG Boden 2005); [4]Munsell Color 2009

Source: Own table

3.2.3 Results of Laboratory analysis

The laboratory measurements of the alluvial apron sediments comprise granulometric, petroloqical and geochemical, and mineralogical properties. The attributes of alluvial fan morphodynamics and of the dominating formative events are primarily evident in the granulometric data, while the major and minor element contents and the mineralogy revealed the differences regarding the post sedimentary alteration.

The total organic carbon (TOC) was calculated from measured TIC and TC (cf. Chap. 2.3). Resulting values are too low (TOC < 1 weight-%) throughout all the samples and TN was below the lower detection limits. This is due to very low to no "contents of" organic matter in the samples and the low concentrations prevent from valid estimations about organic matter traces.

$Q^{al}0$, $Q^{ap}1$-2 – Eroded alluvial fan and apron sedimentology and geochemistry

The granulometric information derived from the alluvial apron sediments shows increased clay and silt contents in the top layer of $Q^{ap}1$ (S03-C-II) and $Q^{ap}2$ (S03-D-I) (Tab. 3.2.7). Here, an increased amount of fine granules coincides with a decrease of the sceleton component and higher contents of oxides from Fe, Mn and P (Tab. 3.2.8). A less pronounced increase of clay and silt was measured in all three sections

Table 3.2.7: Physical and chemical properties of eroded alluvial apron sediments.

				Fine Soil Texture				Sceleton Component	Fine Soil Statistic Properties			pH-Value
Section	Sample	Layer	Depth [cm]	clay [%]	silt [%]	sand [%]	texture class	[%] of total	median [µm]	mean - FWg -	sorting - FWg -	[aqua dest.]
S03-C-I	MP067	1	10	5,33	23,03	71,63	Sl2	62,54	240,40	142,39	6,81	8,37
S03-C-I	MP066	2	40	3,58	12,06	84,33	Su2	64,48	521,50	315,08	4,62	8,34
S03-C-I	MP065	3	70	8,00	39,83	52,15	Su3	86,24	71,09	62,67	8,89	8,13
S03-C-I	MP064	4	110	4,04	15,64	80,35	Su2	43,33	434,80	238,58	5,52	8,20
S03-C-I	MP063	5	90	9,32	35,82	54,89	Sl3	50,82	84,36	59,66	9,00	8,08
S03-C-I	MP062	6	140	6,72	24,74	68,55	Sl2	66,25	238,20	116,02	8,16	8,08
S03-C-II	MP072	1	10	17,20	59,50	23,35	Lu	41,99	15,32	13,99	6,51	8,12
S03-C-II	MP071	2	20	10,50	35,52	54,04	Sl3	57,22	83,66	56,23	9,76	8,08
S03-C-II	MP070	3	60	3,78	14,89	81,25	Su2	72,08	539,70	274,50	5,58	8,28
S03-C-II	MP069	4	80	7,20	31,06	61,81	Su3	64,52	128,20	81,04	8,10	8,17
S03-C-II	MP068	5	120	5,36	20,47	74,23	Sl2	58,85	329,60	156,82	7,30	8,25
S03-D-I	MP087	1	10	19,80	55,50	24,80	Lu	43,53	14,64	13,90	8,02	8,03
S03-D-I	MP086	2	40	10,30	41,30	48,35	Slu	74,65	56,17	50,40	10,28	8,11
S03-D-I	MP085	3	60	8,38	34,79	56,88	Sl3	73,98	113,70	71,99	9,19	8,09
S03-D-I	MP084	4	90	9,82	43,60	46,66	Slu	64,74	50,76	46,75	9,66	8,36

Texture classes/texture suffix: T/t = Clay/clayey << U/u = Silt/silty << S/s = Sand/sandy; L/l = loam/loamy;
Suffix grade: 2 = slightly << 3 = moderately << 4 = very (Ad-hoc-AG Boden 2005) FWg = Folk and Ward geometric method: mean [µm]; sorting (< 1.41: well; 1.41 - 2: moderately; > 2: poorly sorted) (Blott & Pye 2001)

Source: Own table

Table 3.2.8: Content of selected major and minor elements in eroded alluvial apron sediments.

Section	Sample	Layer	Depth [cm]	p-ED-XRF measured elements [area - %]			Aqua regia extracted elements [weight - %]								
				Si_{ox}	Al_{ox}	Ti_{ox}	Ca_{ox}	Mg_{ox}	Na_{ox}	K_{ox}	Sr_{ox}	Fe_{ox}	Mn_{ox}	P_{ox}	S_{ox}
S03-C-I	MP067	1	10	32,12	5,43	0,29	8,56	1,69	0,05	0,76	0,02	1,79	0,04	0,16	0,12
S03-C-I	MP066	2	40	30,44	4,82	0,24	8,96	1,80	0,04	0,72	0,02	1,62	0,03	0,13	0,11
S03-C-I	MP065	3	70	31,19	6,30	0,35	7,38	1,73	0,06	0,89	0,03	2,18	0,04	0,17	0,14
S03-C-I	MP064	4	110	32,40	5,58	0,28	8,46	1,67	0,04	0,82	0,02	1,70	0,04	0,13	0,12
S03-C-I	MP063	5	90	30,70	5,98	0,30	7,96	1,92	0,06	0,93	0,02	2,04	0,04	0,11	0,13
S03-C-I	MP062	6	140	30,42	5,02	0,29	8,66	1,75	0,06	0,80	0,02	1,85	0,04	0,13	0,18
S03-C-II	MP072	1	10	28,11	7,15	0,47	6,52	2,20	0,07	1,19	0,02	2,95	0,06	0,28	0,10
S03-C-II	MP071	2	20	29,27	6,97	0,37	7,11	1,89	0,07	1,27	0,02	2,47	0,05	0,18	0,09
S03-C-II	MP070	3	60	30,80	6,92	0,36	6,92	1,93	0,08	1,26	0,02	2,39	0,04	0,15	0,23
S03-C-II	MP069	4	80	30,70	6,14	0,33	7,28	1,94	0,09	1,03	0,04	2,11	0,04	0,12	1,23
S03-C-II	MP068	5	120	30,41	5,55	0,30	7,95	2,23	0,09	0,97	0,02	2,00	0,04	0,13	0,56
S03-D-I	MP087	1	10	28,55	7,55	0,42	6,55	2,30	0,07	1,24	0,03	2,83	0,06	0,21	0,14
S03-D-I	MP086	2	40	29,70	6,12	0,37	7,47	2,05	0,06	1,14	0,02	2,22	0,04	0,14	0,12
S03-D-I	MP085	3	60	30,54	6,16	0,34	7,79	1,92	0,10	1,04	0,02	2,09	0,04	0,16	0,14
S03-D-I	MP084	4	90	27,21	6,02	0,31	8,76	2,03	0,18	0,91	0,11	1,97	0,04	0,15	5,84

Source: Own table

at depth of about 80-90 cm. Here, the aforementioned pedogenetic key ions do not show any considerable variability, although a fossil B-horizon was observed in the field at about that depth. The properties of fine soil statistics confirm the mapped close morphological relationship of S03-C-II and S03-C-I. The lower layers of both sections represent common morphodynamics and depositional environments, which were classified to $Q^{ap}1$. In contrast to section S03-C-II, the surface of S03-C-I was not abandoned, and alluvial fan morphodynamics prevailed until today. This lead to strongly different development of surface layers and therefore the surface of S03-C-I is classified as $Q^{ap}0$.

The highest pH-values were measured in the young top layers of $Q^{al}0$ and in the oldest layer of $Q^{ap}2$. In this layer's contents of Ca-ions are high, pointing to an increase of calcium carbonate in $Q^{al}0$, and to an increase of calcium sulfate (gypsum) in $Q^{ap}2$. In $Q^{ap}2$ Na- and Cl-ions – supposedly from halite – are also increased. In addition the data reveals a depletion of Ca in the top layers of S03-C-II and -D-I (Tab. 3.2.8), which coincides with increased contents of pedogenic oxides from Fe, Mn, P and Al. Also layer 3 of $Q^{al}0$ shows increased pedogenic oxides and high clay amounts in the fine soil matrix, which – together with the layer's debris flow character – is a sign of allochthonous input of soil matter.

$Q^{al}0$-1 – Recent and Subrecent alluvial fan sedimentology and geochemistry

The common granulometric feature of the youngest alluvial fan generation $Q^{al}0$ (S03-B-I) and the generation $Q^{al}1$ (S03-B-II) is the occurrence of fine, strong to moderately

silty sands in the lowest layers (Tab. 3.2.9). In addition, the skeleton component is reduced in the fine layers. The layers of torrential fluvial or slope-fluvial origin show moderate to high amounts of skeleton together with moderately increased clay and silt contents, which is due to the reduced fluvial selection of grain sizes during a sudden deposition. The high sorting values represent overall poor grain size sorting, according to the applied Folk and Ward geometric method (Blott & Pye 2001). The values increase, where torrential deposition took place, or when extremely high or small grain sizes are dominating the sample. Above ~90 cm depth, the sorting-values of $Q^{al}1$-layers are higher than those of $Q^{al}0$ and this relationship is inverted in the deeper layers. The differing character of the formative events, which formed the two distinct alluvial fan generations, is evident in this two-parted value distribution and to a certain degree in grainsize mean and median values.

Table 3.2.9: Physical and chemical properties of young alluvial fan generations.

				Fine Soil Texture				Sceleton Component	Fine Soil Statistic Properties			pH-Value
Section	Sample	Layer	Depth [cm]	clay [%]	silt [%]	sand [%]	texture class	[%] of total	median [µm]	mean - FWg -	sorting - FWg -	[aqua dest.]
S03-B-I	MP081	3	10	5	23	73	Su2	59	250	163	6,2	8,2
S03-B-I	MP080	4	20	3	12	85	Su2	10	324	247	4,5	8,2
S03-B-I	MP083	1	40	3	9	89	Ss	75	486	387	3,4	8,3
S03-B-I	MP082	2	60	4	14	82	Su2	4	233	197	4,4	8,2
S03-B-I	MP079	5	70	3	9	88	Ss	48	478	365	3,7	8,3
S03-B-I	MP078	6	70	2	7	91	Ss	57	557	503	2,9	8,4
S03-B-I	MP077	7	90	6	26	68	Su3	58	186	119	6,7	8,1
S03-B-I	MP076	8	110	5	19	76	Sl2	78	234	157	5,3	8,1
S03-B-I	MP075	8	130	3	13	84	Su2	54	393	262	4,4	8,1
S03-B-I	MP074	9	150	5	44	51	Su4	3	64	56	5,4	8,1
S03-B-I	MP073	10	220	7	38	55	Su3	26	83	66	7,6	8,1
S03-B-II	MP061	1	10	10	38	52	Sl3	72	68	50	8,7	8,1
S03-B-II	MP060	2	20	7	22	71	Sl2	60	321	135	8,2	8,2
S03-B-II	MP059	3	30	9	32	59	Sl3	12	120	76	9,3	8,2
S03-B-II	MP054	9	60	3	9	88	Ss	54	512	388	3,5	8,2
S03-B-II	MP058b	4	60	6	29	65	Su3	59	272	117	9,0	8,1
S03-B-II	MP058	5	90	3	12	85	Su2	54	552	361	4,6	8,7
S03-B-II	MP057	6	130	3	14	82	Su2	56	491	277	4,8	8,7
S03-B-II	MP056	7	150	5	17	78	Su2	61	462	208	6,3	8,6
S03-B-II	MP053	8	150	7	41	53	Su4	24	69	52	5,1	8,1
S03-B-II	MP055	10	130	5	37	58	Su3	32	93	80	6,2	8,8

Texture classes/texture suffix: T/t = Clay/clayey << U/u = Silt/silty << S/s = Sand/sandy; L/l = loam/loamy; Suffix grade: 2 = slightly << 3 = moderately << 4 = strongly (Ad-hoc-AG Boden 2005) FWg = Folk and Ward geometric method: mean [µm]; sorting (< 1.41: well; 1.41 - 2: moderately; > 2: poorly sorted) (Blott & Pye 2001)

Source: Own table

Table 3.2.10: Content of selected major and minor elements in young alluvial fans.

				p-ED-XRF measured elements [area - %]			Aqua regia extracted elements [weight - %]								
Section	Sample	Layer	Depth [cm]	Si_{ox}	Al_{ox}	Ti_{ox}	Ca_{ox}	Mg_{ox}	Na_{ox}	K_{ox}	Sr_{ox}	Fe_{ox}	Mn_{ox}	P_{ox}	S_{ox}
S03-B-I	MP081	3	10	33,26	4,76	0,28	7,65	1,47	0,06	0,64	0,02	1,75	0,04	0,14	0,16
S03-B-I	MP080	4	20	35,89	4,26	0,24	6,77	1,23	0,04	0,58	0,02	1,43	0,03	0,11	0,12
S03-B-I	MP083	1	40	33,04	4,40	0,23	8,59	1,62	0,04	0,56	0,02	1,53	0,03	0,12	0,13
S03-B-I	MP082	2	60	34,44	4,54	0,26	7,28	1,35	0,07	0,62	0,02	1,56	0,03	0,14	0,14
S03-B-I	MP079	5	70	31,70	4,34	0,26	8,85	1,75	0,05	0,56	0,02	1,55	0,03	0,12	0,21
S03-B-I	MP078	6	70	33,72	4,40	0,22	8,25	1,37	0,04	0,57	0,02	1,35	0,03	0,11	0,24
S03-B-I	MP077	7	90	32,66	5,20	0,30	7,81	1,55	0,05	0,72	0,02	1,75	0,03	0,15	0,21
S03-B-I	MP076	8	110	34,15	4,38	0,25	7,62	1,28	0,04	0,57	0,03	1,50	0,03	0,12	0,54
S03-B-I	MP075	8	130	32,82	4,48	0,23	8,66	1,55	0,03	0,42	0,02	1,38	0,03	0,12	0,54
S03-B-I	MP074	9	150	22,78	4,62	0,22	12,00	1,13	0,06	0,44	0,16	1,30	0,03	0,10	14,10
S03-B-I	MP073	10	220	27,83	4,87	0,26	9,76	1,47	0,07	0,45	0,09	1,56	0,03	0,12	7,79
S03-B-II	MP061	1	10	30,45	5,73	0,33	7,91	1,74	0,08	0,67	0,03	2,15	0,04	0,15	0,17
S03-B-II	MP060	2	20	30,63	5,64	0,26	7,89	1,87	0,04	0,58	0,02	1,87	0,03	0,10	0,16
S03-B-II	MP059	3	30	30,29	5,78	0,32	8,11	1,83	0,08	0,82	0,03	2,09	0,04	0,12	0,17
S03-B-II	MP054	9	60	30,73	4,79	0,23	9,15	1,52	0,03	0,58	0,02	1,50	0,03	0,12	0,26
S03-B-II	MP058b	4	60	24,56	4,77	0,21	11,64	1,65	0,07	0,58	0,13	1,54	0,03	0,10	10,92
S03-B-II	MP058	5	90	30,53	4,64	0,24	9,14	1,53	0,10	0,62	0,04	1,53	0,03	0,11	2,94
S03-B-II	MP057	6	130	31,36	4,87	0,25	8,55	1,84	0,13	0,71	0,05	1,65	0,03	0,12	1,45
S03-B-II	MP056	7	150	31,57	5,31	0,26	8,31	1,75	0,12	0,67	0,03	1,70	0,03	0,13	0,50
S03-B-II	MP053	8	150	25,17	5,27	0,28	10,71	1,41	0,06	0,53	0,13	1,68	0,03	0,10	11,15
S03-B-II	MP055	10	130	27,62	5,26	0,28	9,16	1,73	0,25	0,76	0,06	1,90	0,04	0,13	6,87

Source: Own table

The same relationship can also be observed in the pH-value distribution: when sorting is good the pH-value is high and where the pH-value decreases the sorting is poorer. Although, the pH-values are generally higher in S03-B-II, independent from the aforementioned relationship.

The twofold character of the granulometric layer properties is not clearly evident in the major and minor element contents of the two young alluvial fan generations (Tab. 3.2.10). Anyway, the layers of $Q^{al}1$ (section S03-B-II) show increased contents of sulfur and calcite peaks below 90 cm depth, while increased contents of these gypsum related ions in $Q^{al}0$ were only measured in the deep fine sediment layers of section S03-B-I. Additionally, pedogenic ions (Al, K, Fe, Mn, P) are increased in the top layers of S03-B-II above 30 cm, and – less pronounced – in 10 cm and 90 cm depth of section S03-B-I.

Surface alteration of sediments

The geochemistry of the sediment samples also indicates varying degrees of surface weathering (Büdel et al. 2017). The results of the CIA-calculations as well as proxy

values like the Si/Al- and Mg/Ca-ratio validate the field description of relative surface ages. As described above the CIA-value is an indicator for feldspar weathering (Nesbitt & Young 1982). The Si/Al-ratio indicates un-weathered allochthonous sediment input and Mg/Ca-ratio serves as a proxy for sediment salinity (Schütt 2004). The CIA-values are comparably low, which can be explained by the observed low feldspar contents and by the presence of highly weathered sedimentary rocks in the watersheds (cf. Tab. 1.3.1). Nevertheless, the CIA varies between values from 31.1 at section S03B-I to 52.2 at section S03-D-I (Tab. 3.2.11). This indicates less weathering intensity and a younger surface at S03-B-I and more intense weathering along with an older surface at S03-D-I. Additional observations from fieldwork are also listed in Tab. 3.2.11 and they are in line with the CIA-values. The order of all CIA-values and parameters comprehensively confirms the chronostratigraphic order that was developed from the surface mapping (cf. Chap. 3.1.2).

The mineralogy of selected sections does not conveniently validate the observations from field description and element quantification (Tab. 3.2.12). Semi-quantitative estimations, based on the correlation of XRD-peak intensities with Reference Intensity Ratios (RIR), yield constant evaporite contents between 4-5 % of Calcite and 1-2 % of Gypsum, with considerably low scores for Gypsum-peaks (Tab. 3.2.12). A considera-

Table 3.2.11: Top Layer characteristics of the sections (from Büdel et al. 2017) reveal their chronostratigraphic relationship and the representative potential of the sections for the map units in figure 3.2.5. Chemical Index of Alteration (CIA) and Si/Al-ratio quantify the relative age of the alluvial fan surfaces. The surface at S03-D-I is according to field description and CIA the most weathered surface which is also reflected in clay minerals ratio in figure 3.2.5 for the map unit $Q^{ap}2$ – "Eroded Fans and apron – Quaternary, relative age 2". Ca/Mg-ratio as an indicator for salinity, however, is only in line with salinity index where no desert pavement is disturbing the reflectance.

Section	Field description of top layer	depth (cm)	consolidation[1]	evaporates[2]	root density[3]	Colour (Munsell)[4]	pH	Ca/Mg	Si/Al	CIA
S03-D-I	cambic horizon in loamy debris flow gravel under desert pavement	0 - 15	2 loose	2 weak	3 medium	5 YR 7/4	8.0	0.351	3.78	52.2
S03-C-II	yermic horizon in loamy debris flow gravel under desert pavement	0 - 6	1 very loose	0 none	3 medium	5 YR 8/3	8.1	0.338	3.93	51.0
S03-B-II	yermic horizon in unsorted gravel and loamy sand	0 - 4	1 very loose	3 medium	0 none	--	8.1	0.220	5.32	35.6
S03-A-I	salic horizon in layered sandy silt and gravel	0 - 32	2 loose	4 strong	0 none	7.5 YR 6/4	7.9	0.286	7.30	33.1
S03-C-I	A-Horizon in fluvic material; poorly sorted pebble and gravel in loamy sand	0 - 30	1 very loose	2 weak	3 medium	5 YR 6/3	8.4	0.198	5.92	31.7
S03-B-I	debris flow gravel, no soil horizons	0 - 20	1 very loose	0 none	3 medium	5 YR 7/2	8.2	0.192	6.99	31.1

[1]degree of consolidation: 1-5; [2]degree of macroscopic evaporite density: 0-5; [3]degree of root density: 0-5 (Ad-hoc-AG Boden 2005); [4]Munsell Color 2009

Source: Own table

Table 3.2.12: Mineralogy derived from XRD measurements. Specified minerals are given with Powder Diffraction File (PDF) reference number.

Section	Sample	Layer	Depth [cm]	Quartz - 79-1910 -	Calcite - 83-0578 -	Dolomite - 75-1759 -	Gypsum - 74-1433 -	Feldspar Group Albite / Anorthite	Feldspar Group Orhoclase / Microcline
S03-D-I	MP087	1	10	++++	+++	++		++	++
S03-D-I	MP086	2	40	++++	+++	++		+	++
S03-C-II	MP072	1	10	++++	+++	++		++	++
S03-C-II	MP070	3	60	++++	+++	+++	(+)	++	++
S03-C-II	MP069	4	80	++++	+++	+++	+	++	++
S03-B-II	MP061	1	10	++++	+++	++		++	++
S03-B-II	MP059	3	30	++++	+++	++		++	++

Mica Group Muscovite - 82-0576 -	Mica Group Biotite - 88-1900 -	Clay Mineral Group Kaolinite - 89-6538 -	Clay Mineral Group Vermiculite - 34-0166 -
++	(+)	>+<	>+<
(+)	(+)		
+(+)	+	(+)	(+)
+(+)	+	(+)	(+)
+(+)	+		
+(+)	+		
+	+	>+<	(+)

Percent match of reference intensities to peak intensities (=Score)

++++ > *50 % Score*
+++ > *35 % Score*
++ > *20 % Score*
+ > *10 % Score*

() = *1 strong unexplained line*
>< = *2 strong unexplained lines*

Source: Own table

ble signal of clay minerals is bound to the soil covers of sections S03-C-II and S03-D-I, but is inverted for the younger alluvial fan surface from S03-B-II. This is related to the allochthonous origin of the channel fill, represented by layer 3 of S03-B-II. Thereby, the layers of clay mineral occurrence always coincide with reduced scores for mica.

3.3 Stratigraphy and sedimentological features of the playa sediments

3.3.1 Stratigraphy and initial core description

The stratigraphic and sedimentologic investigations of playa and playa lake related sediments revealed the specific sedimentational environment of their two associated localities, in the central playa (P^{l}; Pic: 3.3.1) and at the elevated and eroded supposed lake terrace (P^{er}).

P^{er} – Eroded lake and playa sediments at S03-A-I & -II

The fine sediments of the lake terrace retrace the 1 150 m a.s.l. contour line at the alluvial aprons fan toe. They are mapped and initially classified as "P^{er} – eroded lake and playa sediments", described as such for the first time by Krinsley (1970). The shape of this prominent sediments is also considered to mark the strike of the Damghan Fault. This fault becomes obvious with a limestone-outcrop penetrating the alluvial sediment in the western connection to the nearby fine sediments. It is a left-lateral fault with a steeply dipping fault plane and likely changing polarity (Hollingsworth et al. 2010). Its tectonic behavior may also have caused enough uplift to save the fine sediments from erosion so that they prevailed at this locality.

Two sections were prepared from slope exposures at the flanks of an incised channel. The channel crosses fine sediments from north to south and the channel bottom shows the same slope as observed for the alluvial aprons distal area. The locations of sections S03-A-I and S03-A-II were chosen in different altitudes alongside the sloping channel flank (Fig. 3.2.6). Thus, the combination of both sections provides a full coverage of the aboveground vertical extent of the fine sediment body. The two sections cover a depth of at least 750 cm and a maximum width of 300 cm. There is an erosional discontinuity between the bottom layer of S03-A-I and the top layer of S03-A-II and it was not possible to identify the missing contact layer of the two sections (Fig. 3.3.1). Hence, their relative position was determined by "their" elevation and situation in the incised channel and the depth values of the single layers (Tab. 3.3.1) are according to the combined depth, which was calculated from the sections relative positions.

Picture 3.3.1: A massive halite salt crusts with polygonal structures characterises the coring site B04-A in the central playa of Damghan (Picture: C. Büdel, 2012).

Source: Own photograph

Figure 3.3.1: Sections S03-A-I and S03-A-II with layer descriptions gives an insight of the texture and structure of map unit "P^{er} - eroded lake and playa sediments". Legend entries are ordered according to their layer description tables.

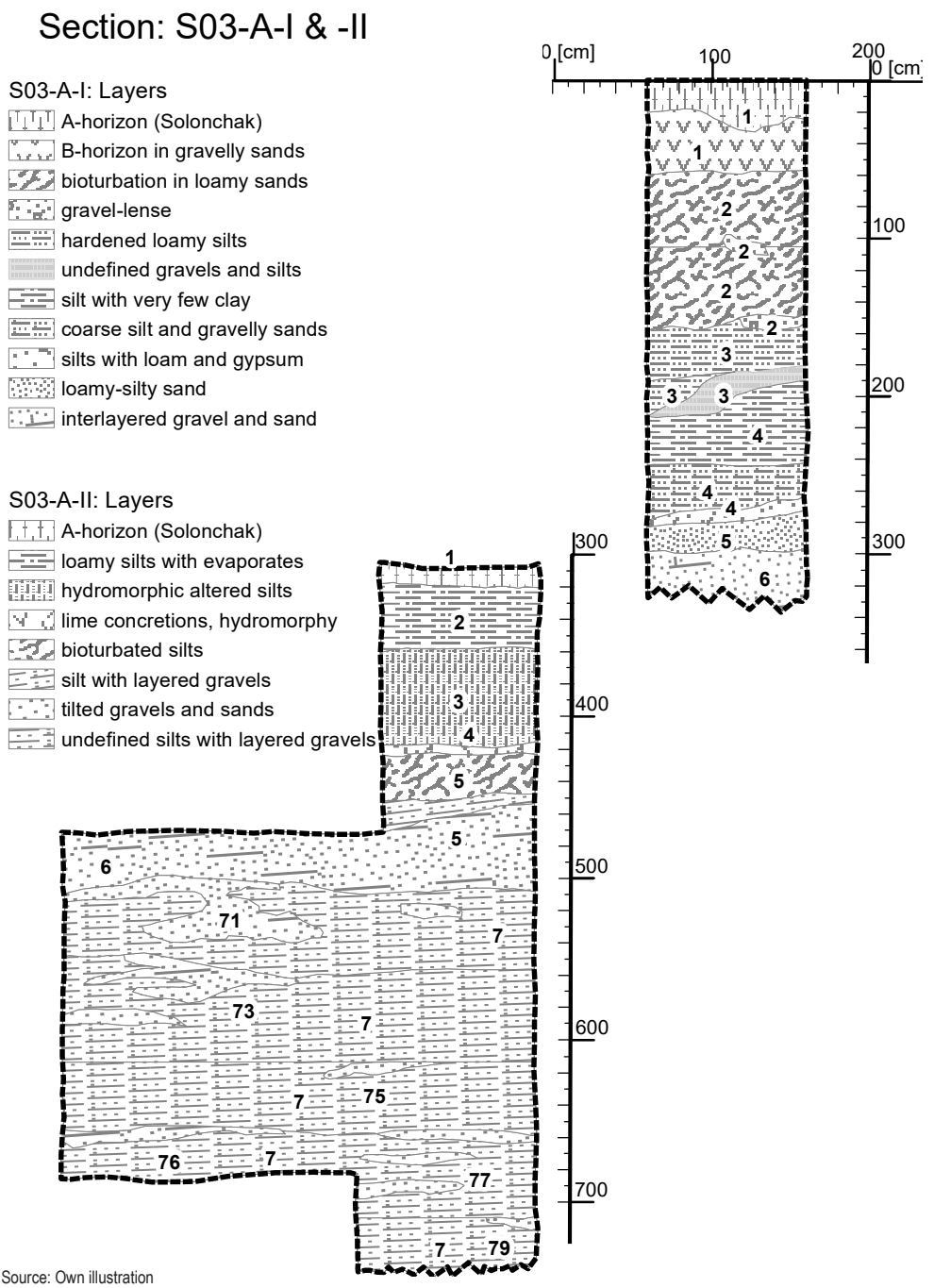

Source: Own illustration

The prepared sections from slope exposures do not show any tectonic deformation and in the surface layer of the fine sediments a Solonchak has developed with decreasing soil thickness from upslope to downslope exposures – layer 1 in the sections (Tab. 3.3.1.)

Loamy sands and silts in layer 2 (S03-A-I) and layers 5 and 7 (S03-A-II) feature fossil traces of roots and burrows. Overall evidence for bioturbation is rare but more frequent in above mentioned type of loamy silts and sands. The fossil traces in layers 5 and 7 ignore layer contacts and are regarded to be of post-sedimentary origin. The issue of layer 4 in S03-A-II, showing loose, densely packed root-shaped lime concretions (Pic. 3.3.2) directly topping layer 5, may indicate a former lake or shoreline surface in this level. Bottom layer 4(c) in SO3-A-I is made up by Gypsum needles, which are layered in line with surrounding loamy-sandy silts. That syn-sedimentary occurrence of gypsum may also indicate a former shoreline.

Picture 3.3.2: The root-shaped lime concretions from S03-A-II may indicate a former littoral area (scale in cm. Picture: C. Büdel, 2010).

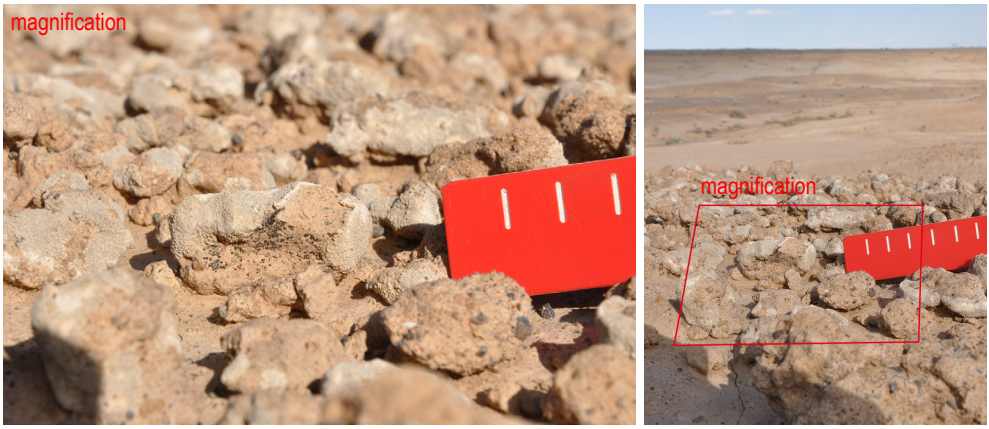

Source: Own pictures

Layers 3 to 6 (S03-A-I) are representing a sequence of down-coarsening sediments, starting with very hard loamy silts at the top and ending up in stratified sand and gravel layers. Coarser sediments show medium to strong alteration by hydromorphic processes, in particular extensive but meager stained surfaces from iron-oxides and -hydroxides together with very weak bleaching. Pores are better developed in the finer sediments at the top of the sequence.

In S03-A-2 hydromorphic oxidation is stronger developed and a high amount of manganese-oxides stains the sediments, particular in layers 3 and 4. Iron oxides intensely trace fossil roots in layers 5-7, while bleaching is hardly noticeable, with an obvious, but still weak bleaching restricted to layers 3 and 4.

Layers 5-7, below 450 cm (S03-A-II) reveal a high amount of sedimentation by fluvial or slope-fluvial processes, interleaved with slack-water or lacustrine-like phases. Here loose, tilted gravels and sands and layered gravel and sand lenses are enveloped by hardened silts with thin gravel layers. Coarse and medium sand dom-

inated gravel lenses can be clearly distinguished from surrounding medium and coarse silts. The stratified sands and gravels, as well as the gravel lenses are tilted downslope with an inclination of 2-3°. They feature unsorted bedding to normal graded bedding with considerable sorted gravels and sands.

Table 3.3.1: The layer properties of section S03-A-I & -II. Layers are ordered by depth.

Section S03-A-I & -II: Field description of layers								*excavator trench – 1 150 m a.s.l.*
Layer	depth (cm)	layer description	contact to lying layer	Color (Munsell)[4]	Texture / structure	consoli-dation[1]	evaporites[2]	root density[3]
1 (A-I)	0 - 60	soil horizons (Solonchak) in gravelly sands	sharp	7,5 YR 6/4	sand and gravel; weakly sorted	0 not visible	2 weak	0 not visible
2	60 - 152	bioturbation in loamy sands	diffuse	7,5 YR 6/4	unsorted loamy sand and silts with gravel lenses	5 very strong	3 medium	0 not visible
3	152 - 213	hardened loamy silts	sharp; tilted	7,5 YR 6/4	loamy-sandy silt with few gravels and a sand and gravel lense	4 strong	2-3 weak to medium	0 (5) very strong (in lense)
4 a, b, c	193 - 284	(a) down-coarsening silts with very few clay to (b) coarse silts and gravelly sands with (c) gypsum at bottom contact	sharp; tilted	7,5 YR 6/4	a) silts with very few clay to (b) sandy silts to loamy sand with some gravel; well sorted	4 strong	2 weak (5 - very strong at (c) bottom contact)	0 not visible
5	284 - 299	loamy-silty sand layer	sharp	7,5 YR 7/4	loamy-silty sand with very few gravels; very well sorted	2 weak	1 very weak	3 medium
6	299 - 330+	interlayered gravel and sand	*(buried)*	*no data*	very silty sand with 4 gravel lenses; well sorted	0-1 very weak	0 no evapo-rates	5 very strong
1 (A-II)	307 - 322	soil horizons (Solonchak) in very clayey silt	diffuse	7,5 YR 6/4	very clayey silt	2 weak	2 weak	0 not visible
2	322 - 361	loamy silts with evaporites	sharp	7,5 YR 7/4	very clayey silt with very few gravel	4 strong	3 medium	0 not visible
3	361 - 421	hydromorphic altered silts	diffuse	2,5 Y 7/4	very clayey silt with very few gravel	4 strong	2 weak; nodules	5 very strong
4	421 - 427	lime concretions in hydromorphic altered silts	sharp	10 YR 7/4	very clayey silts	5 very strong	5 very strong; concretions	5 very strong
5	427 - 477	bioturbated silts and silt with layered gravels	sharp; tilted	10 YR 7/4	loamy-sandy silts with some gravel	2 weak	1 very weak; concretions	4 strong
6	477 - 517	tilted gravels and sands	diffuse; tilted	10 YR 7/4	unsorted gravels with silty to loamy sands	*no data*	1 very weak	3 medium
7	517 - 747+	undefined silts with layered gravels	*(buried)*	10 YR 7/4	loamy-sandy silts with lenses of unsorted gravels with silty to loamy sands	2 weak	1 very weak; concretions	4 strong (3 in lenses)

[1]degree of consolidation: 1-5 - [2]degree of macroscopic evaporite density: 0-5 - [3]degree of root density: 0-5 (Ad-hoc-AG Boden 2005); [4]Munsell Color 2009

Source: Own table

P^l – Central Playa at core site B04-A

The recent central playa – map unit "P^l – Central Playa" – extents south from the geographic center of the basin, at an altitude of about 1 050 m a.s.l. It covers an area of about 445 km² (derived from Landsat 8 Scene: 11.01.2015; Fig. 3.3.2) and it is fully concealed by a massive, segmented salt crust (Pic. 3.3.1). This features polygons of up to 70 x 70 m in the outer belt, where ground water variability and salt-tectonic activity is high. Furthermore, the massive perennial salt crust is flooded periodically, and extreme events pour in new clastic sediments episodically from the surrounding alluvial aprons (cf. Ullmann et al. 2016).

Figure 3.3.2: Drilling sites B04-A and B02-A with the main landforms which are surrounding playa and clay flats.

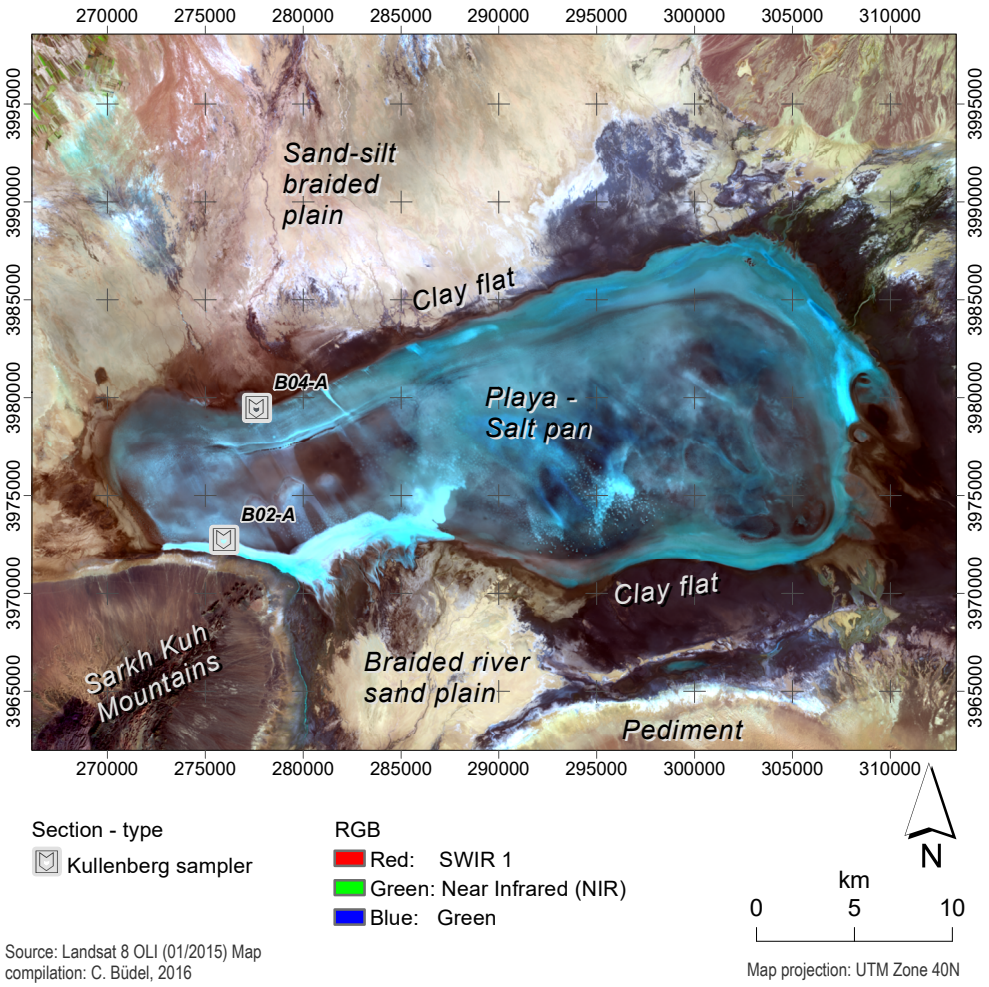

Figure 3.3.3: Core log from the playa sediments at site B04-A.

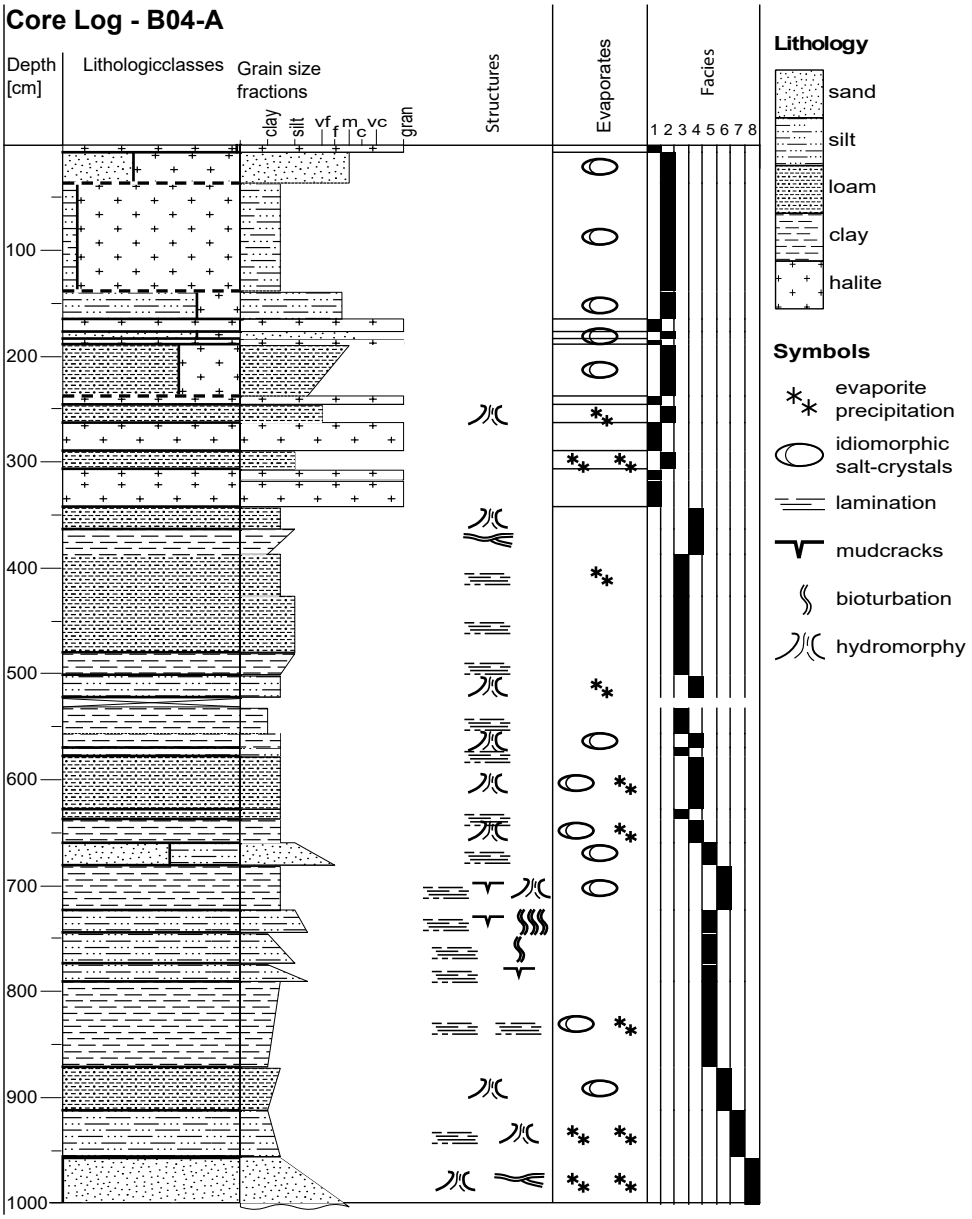

Source: Own illustration

Hence, two sites were selected for ramming core sampling in the central playa, one at each margin in a North-South-transect. Also, the central playa was explored and proved unsuitable for core sampling due to the massive central salt crust. At core site B02-A, the sediment thickness is left unclear and sampling ended in 172 cm depth in massive salts. The lower core was lost after penetrating some minor layers of loamy sand at the top of the core site. Therefore, all results presented hereafter are based on cores of the northern margin site B04-A.

During the compilation of initial core descriptions, core B04-A was separated to eight distinct facies that can be grouped in four units of specific phases of physical and chemical development. The two facies, which constitute one unit, are commonly alternating several times (Fig. 3.3.3; Fig. 3.3.4; Tab. 3.3.2).

Figure 3.3.4: High-resolution line scans of core B04-A (Scans prepared by V. Wennrich, Cologne). Description from top to bottom (uncorrected depths in parenthesis).

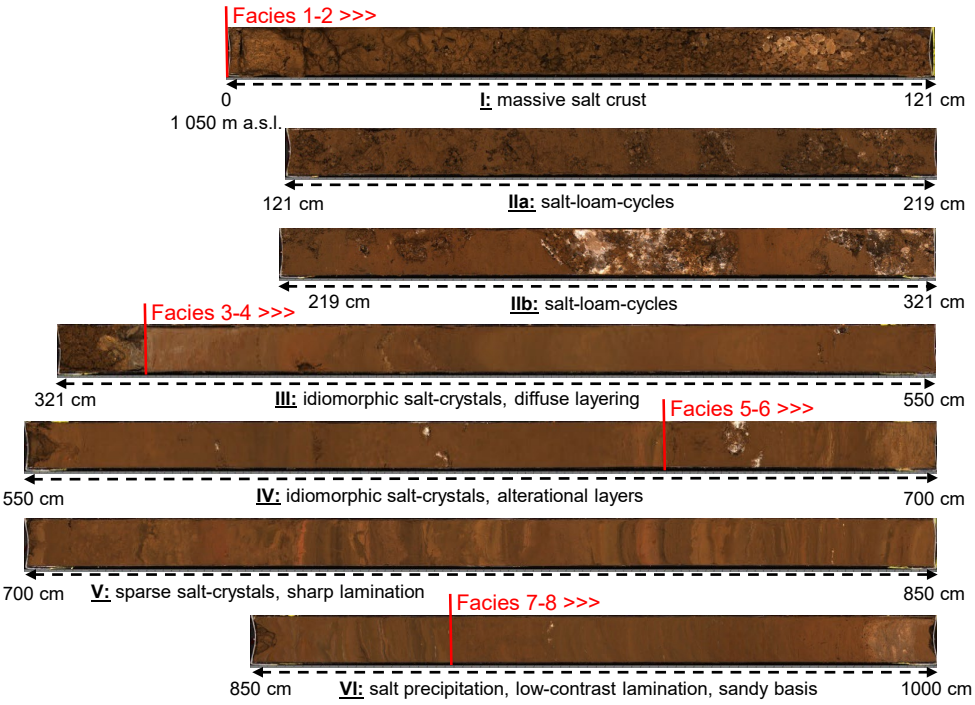

Initial Core Description

I. 0 (36-) – 121 cm; salt crust
II. 121 (166-) – 321 cm (IIa+IIb); salt-loam-cycles (two short scans)
III. 321 (435-) – 550 cm; idiomorphic salt-crystals, diffuse layering
IV. 550 (584-) – 700 cm; idiomorphic salt-crystals, alterational layers
V. 700 (740-) – 850 cm; sparse salt-crystals, sharp lamination
VI. 850 (923-) – 1000 cm; salt precipitation, low-contrast lamination, sandy basis

Source: Own illustration

- **Facies 7-8 (1000 - 913 cm)**
  The core is terminating in densely packed loamy silty sands which prevented deeper penetration. Layering and hydromorphic features with gypsum influence the lower layers, while weak lamination can be seen in upper parts (facies 7). A high amount of macroscopic gypsum crystals was observed at the unit's bottom, which constitute a medium sand texture and may indicate gypsum crusting.

- **Facies 5-6 (913 - 660 cm)**
  A fining-up texture to silty loam leads to facies 5 and 6, which are dominated by three major phases of fining up silts and later sand. The particular silt and sand phases belong to facies 5 and are setting in at 810, 765 and 700 cm. The cores are laminated with locally sharp laminae between 1 - 12 mm thick throughout the whole facies 5. Where coarser silts occur and clay content is reduced lamination vanishes or shifts to rough layering. At the contact to hanging facies 6 signs of intense bioturbation occur and material from hanging wall is translocated to foot layers. Facies 6 shows a more chaotic fabric, indices of bioturbation and hardly noticeable layering or isolated laminae are typical. Hydromorphic features, mud-cracks and idiomorphic salt-crystals are common in facies 6.

- **Facies 3-4 (660 - 343 cm)**
  This unit shows homogenous, partly laminated deposits with less grain-size variety and almost exclusively very silty clay or very clayey silt. Structures of layering and locally fine (1 - 5 mm) lamination often are diffusely preserved and hydromorphy was abundantly active. Idiomorphic salt crystals were observed, together with the hydromorphic features in lower layers of facies 4. Evaporite precipitation of gypsum shows regular peaks and at the top of the unit, within facies 4, coarse tilted layering with salt layers prevailed.

- **Facies 1-2 (343 - 0 cm)**
  Alterations of massive salt crusts and intercalated loam and clayey to sandy silt deposits make up this unit which expands down to a depth of 346 cm. Mud layers consist mainly of idiomorphic halite crystals in a unstructured sediment matrix. Coarse sands in loamy-sandy silts occur in two major phases at a depth of 10 - 40 and 140 - 240 cm.

3.3.2 Geophysical and geochemical properties of playa sediment samples

The laboratory analysis of playa and playa lake related sediments from map units P^{er} and P^{l} support the postulated relationship of these two geoarchives. The granulometric and geochemical properties observed in facies 3 - 4 of core B04-A show evident relationship to the properties of combined section S03-A-I & -II from 500 cm upwards. These are based on the salinar cycle and on the development of pH-values and to the genesis of the sediments.

Table 3.3.2: Segment description of core B04-A.

Core Segments	Facies	Thick. [cm]	Depth [cm]	Base boundary	Color (Munsell)	Texture	Main grain sizes	Structures
D2-001	1	7.1	7.1	Sharp	10YR 4/6	Halite 98 %; Silt 2 %	granule	ideomorphic NaCl - massive
D2-002	1	29.2	36.3	Gradational	10YR 5/3	Sand 40 %; Halite 60 %	medium sand	ideomorphic NaCl - lmax=30mm
D2-003a - D2-006	2	102.8	139.1	Gradational	10YR 5/4 - 10YR 4/3	Silt 8 %; Halite 92 %	clay/silt	ideomorphic NaCl - Lmax=15-30 mm, concretions
D2-007	2	25.8	164.9	Sharp	10YR 4/3	Silt 75 %; Halite 25 %	fine/ medium sand	concretions
D2-008a	1	12.3	177.1	Sharp	-	Halite	granule	
D2-008b	2	7.1	184.2	Sharp	10YR 4/3	Sand 75%; Halite 25 %	medium/ coar se sand	ideomorphic NaCl - Lmax=8 mm
D2-008c	1	5.2	189.4	Sharp	-	Halite	granule	
D2-008, +009 +010a	2	47.7	237.1	Gradational	10YR 4/2 - 10YR 5/3	Mud 65 %; Halite 35 %	medium sand - silt/very fine sand	ideomorphic NaCl - Lmax=10-20mm, concretions
D2-010	1	9.0	246.2	Sharp	-	Halite	granule	
D2-11a	2	16.8	262.9	Sharp	10YR 4/4	Mud	very fine sand	Water structures, Evaporite precipitation
D2-011	1	27.7	290.7	Sharp	-	Halite	granule	
D2-012	2	16.8	307.4	Sharp	10YR 4/4	Mud	silt	Evaporite precipitation, Evaporite precipitation
D2-013	1	10.3	317.8		-	Halite	granule	
D2-014	1	24.9	342.7	Sharp	-	Halite	granule	
D2-015a	4	20.9	363.6	Sharp	10YR 4/4	Mud	clay/silt	Water structures
D2-015+016a+ 016b+016c+ 016d	4	23.9	387.5		10YR 5/3 - 10YR 4/4	Clay	silt - clay	Swaley cross stratification
D2-016	3	39.8	427.3		10YR 4/3	Mud	clay/silt	diffuse lamination, Evaporite precipitation
D2-017	3	53.8	481.1	Sharp	10YR 4/4	Mud	silt	diffuse lamination
D2-018+19a	3	20.9	502.0	Sharp	10YR 5/3; 10YR 4/4	Clay	silt - clay/silt	diffuse lamination
D2-019	4	20.9	522.9	Sharp	10YR 4/4	Silt	clay/silt	Water structures, Evaporite precipitation
disturbance	0	9.0	531.8	Sharp	-			disturbance
D2-020	3	23.9	555.8	Gradational	10YR 4/4	Clay	clay	diffuse lamination

Continuation of Tab. 3.3.2

D2-021a	4	13.6	569.3	Sharp	10YR 4/3	Clay	clay/silt	Water structures, concretions
D2-021b+021	3	9.1	578.4	Sharp	10YR 4/4 - 10YR 4/3	Silt	clay/silt	Horizontal planar lamination
D2-022a+022b +022+023a	4	49.1	627.5	Sharp	10YR 5/3 - 10YR 3/3	Mud	clay/silt	Water structures, concretions
D2-023+024a	3	10.3	637.9	Sharp	10YR 4/4; 7,5YR 4/3	Mud	clay/silt	Horizontal planar lamination, Evaporite precipitatio
D2-024	4	22.0	659.9	Sharp	10YR 4/3	Clay	clay/silt	Water structures, concretions, Evaporite precipitation
D2-025a+025b +025c +025d+025	5	22.0	681.8	Sharp	10YR 4/2; 7,5YR 4/3; 10YR 6/4	Sand 60 %; Silt 40 %	silt - fine sand	Horizontal planar lamination, very few concretions
D2-026a+026 +0 27a +027b	6	41.7	723.5	Sharp	10YR 5/3 - 4/2; 7,5YR 5/4 - 4/2	Clay	clay/silt	Horizontal planar lamination, Mudcracks, Water structures, Microscale evaporites
D2-027+028a	5	22.2	745.7	Sharp	5YR 5/4; 7,5YR 5/3; 10YR 4/2	Silt	silt - silt/very fine sand	Horizontal planar lamination, Mudcracks, Intense bioturbation
D2-028b+028	5	28.5	774.2	Sharp	7,5YR 4/2 - 10YR 5/4	Silt	clay - silt	Horizontal planar lamination, Minor bioturbation
D2-029a+b+c+d +029	5	16.7	790.9	Sharp	7,5YR 5/2 - 10YR 4/4	Silt	clay - silt/very fine sand	Horizontal planar lamination, Mudcracks
D2-030a+030 +031a+031	5	81.9	872.7	Sharp	7,5YR 5/2 - 10YR 4/3	Clay	clay/silt - clay	Horizontal planar lamination, Microscale evaporites, Evaporite precipitation
D2-032a+32	6	39.9	912.7	Sharp	7,5YR 4/3 - 10YR 4/2	Mud	clay/silt - clay	Water structures, Microscale evaporites
D2-033a+033	7	43.8	956.5	Sharp	7,5YR 4/2 - 7,5YR 4/4	Silt	clay - clay/silt	Horizontal planar lamination, Water structures, Evaporite precipitation
D2-034a+034	8	43.8	1000	Erosion	7,5YR 4/3; 10YR 5/2	Sand	clay/silt - m	Water structures, Swaley cross stratification, Evaporite precipitation

Source: Own table

Basin sedimentation and issues of sedimentational environments in lakes and playa lakes are closely related to the occurrence and stratigraphic relationship of biogenic matter in the sediments. Therefore, total organic carbon (TOC) was calculated from measured TIC and TC (cf. Chap. 2.3). Resulting values are too low (TOC < 1 weight-%) throughout all the samples and TN was below the lower detection limits. This is due to very low to none organic matter in the samples and the low concentrations prevent from valid estimations about organic matter traces. Calculations about biogenic silicate contents also revealed lowest biogenic contents, and these circumstances are addressed and discussed in chapter 4.4.

P^{er} – Eroded lake and playa sedimentology and geochemistry

The granulometric data of combined section S03-A-I and -II shows very poorly sorted moderately and strongly silty sand and very sandy silts (Fig. 3.3.5). The sorting varies with the grain sizes but overall trends to poorer sorting at the top of the section, with lowest sorting values (= better sorting) between 450 cm and 300 cm depth. This coincides with a continuum of clay and silt maximum values. This transition to more homogenous silts and loamy sands is marked by a steep increase of pH-values at about 500 cm (Büdel et al. 2017).

Major element contents including Ca, Fe and Al show high variation in the lower part of the section and vary with higher frequency but less amplitude in the upper part of the section (Fig. 3.3.6). Although, Al- and Fe-contents do not change with the same conciseness, the standard deviation of their moving averages decreases from about 500 cm upwards. The amount of ions and the range of ion contents of Al, Fe, Mn and K oxides decreases again at a depth of 300 cm. This coincides with decreasing range of Ca-values, but not for the ranges of the S- and Sr-ions, which show highest content peaks above 320 cm depth. This is related to the lack of gypsum in the lower section as it is validated by the XRD data. Hence, R squared for Ca/S-ratio is r^2=0.51 in the first 300 cm and falls to r^2<0.01 from 300-750 cm. The Al/Fe-ratio shows comparable relationship with r^2=0.82 in 0-300 and 0-500 cm depth and r^2<0.01 in the lower section from 500-750 cm. The XRD data reveals reduced signal intensity for mica and feldspar (Muscovite and Microcline) in the layers between 500 and 300 cm and no variability in the surface layers. Additionally, there is no variation of pedogenic ions in the top layers, which supports the field observation of a strong surface erosion on the fine sediment terrace. The high contents of Na values coincide with increased numbers of Cl-ions und thus indicate halite precipitation. Also, a new phase of increasing contents of Mg-ions was measured above the 500 cm depth mark, again with a remarkable shift at 300 cm depth.

P^{l} – Central playa sedimentology and geochemistry

The remarkable step in pH-value which was observed in P^{er} sediments was also measured in sediments from the central playa - P^{l} (Core: B04-A) from about 690 cm upwards (Fig. 3.3.7; Büdel et al. 2017). Here, the top layers of this facies 5 bear a steep increase of the pH-value from pH = 7.0 to more alkaline conditions with pH = 8.0 and thus anticipating the transition to the overlying facies 4. This rapid change of pH-values may also correlate with the pH-step at 500 cm in S03-A-sections. The ph-value decreases with onset of facies 1-2 above 320 cm. Along with this step to more acidic conditions the electric conductivity raises instantly and marks the frequent development of massive halite salt crusts. The sorting decreases (= higher values) continuously and the range of sorting values widens together with the onset of increased pH-values at facies 3-4. The grain sizes highly vary below 690 cm depth with silt-rich layers of facies 5-6 and also in facies 1-2, where massive halite precipitation alternates with coarse sands and clayey silts, primarily from fluvial and slack water deposition. The highest clay contents occur in facies 5-6, where layering is disturbed by the supposedly aeolian input of coarse silt and fine sands, and the clays hardly prevail throughout facies 3-4 until the decrease of clay becomes stronger.

Figure 3.3.5: The granulometry of the combined section S03-A-I and -II shows highest clay contents between 450 cm and 300 cm depth. In addition, the sorting is best in this segment and pH-values increase from 500 cm upwards. Torrential layers with coarse clasts are more frequent below 450 cm, and at the top of the section.

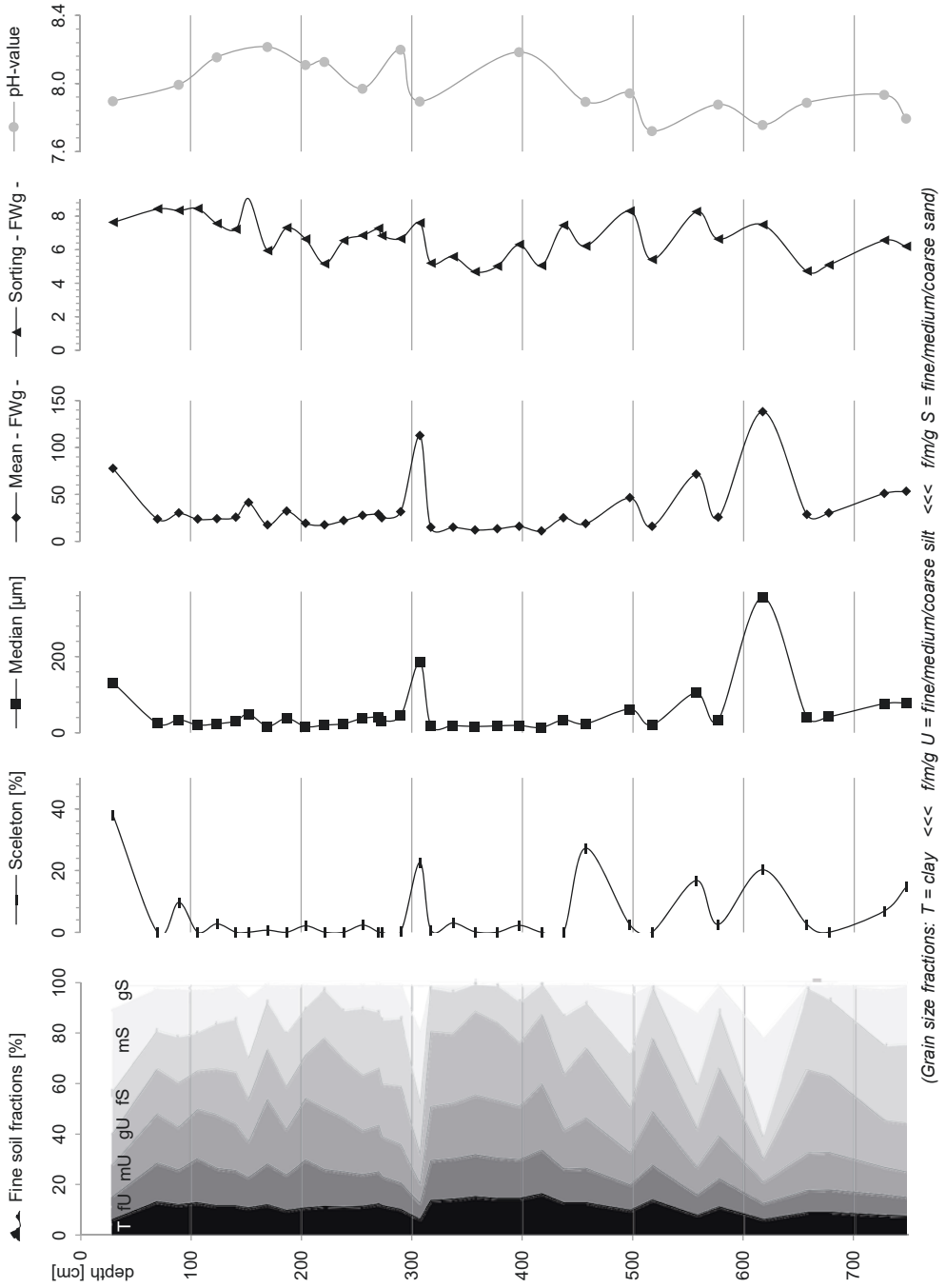

Source: Own illustration

Figure 3.3.6: The element contents of section S03-A-I & -II indicate varying sediment properties. At a depth of 500 cm below the surface an apparent shift affecting all major elements can be observed.

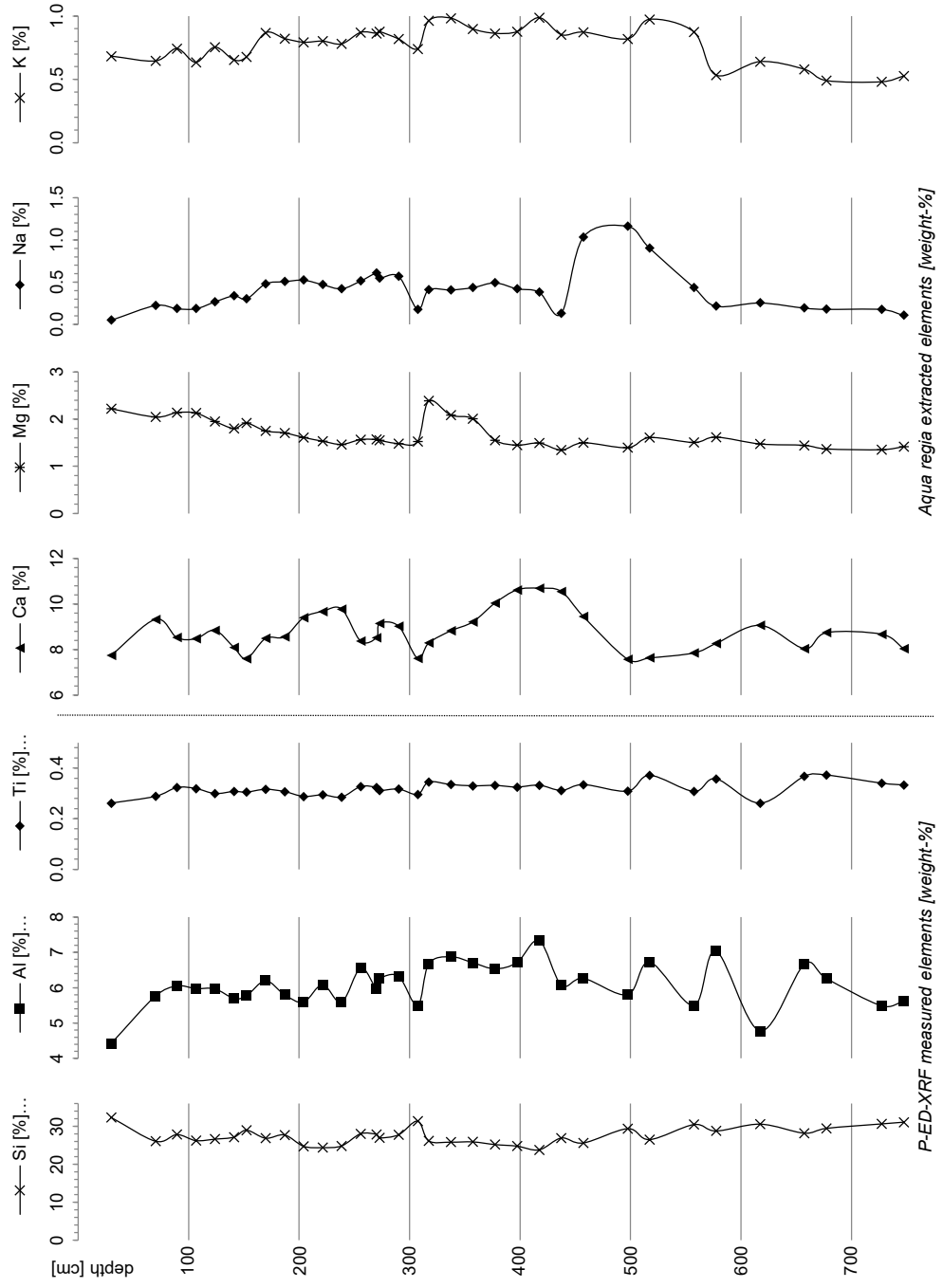

Continuation of Fig. 3.3.8

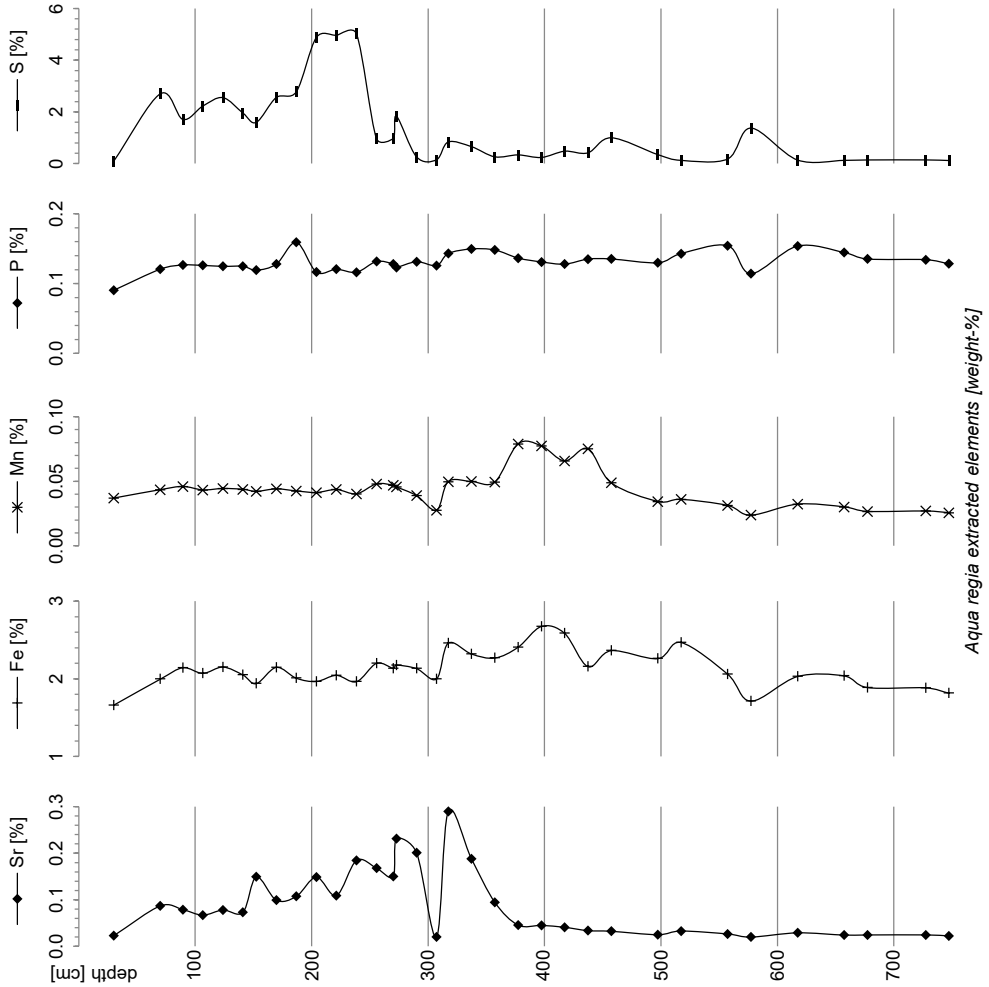

Source: Own illustration

The high Ca and S contents in geochemical data of facies 7-8 confirm the macroscopic evidence and XRD peaks of high gypsum content at the unit's bottom, coinciding with reduced Fe- and Al-Values (Fig. 3.3.8). The $EC_{2.5}$-values of about 6.4-8.4 ms/cm indicate strongly saline conditions regarding easily soluble salts (Bubenzer & Besler 2010; Bertrams et al. 2014).

The geochemical analyses also reveal 4 peaks of sulfur enrichment in facies 5-6, which occur at the beginning and at the end of the unit, suggesting changing hydrological conditions. Electric conductivity is generally reduced in this unit but still shows values of strongly saline conditions which coincide with an increased variability. Calcium is not correlating with the S-content in this unit and features low variability. The opposite behavior is recorded in Al- and Fe-values which are tracing the grain-size peaks, both tightly depending on changes in sedimentation rates.

Figure 3.3.7: Granulometry and statistical and geochemical indicators of core B04-A reveal considerably shifting conditions at the change from facies 5-6 to 3-4 at 660 cm, with an onset of increased pH-values and continuously poorer sorting. The change to facies 1-2 at 343 cm also is indicated by strong changes along with the development of massive salt crusts in more acidic milieus.

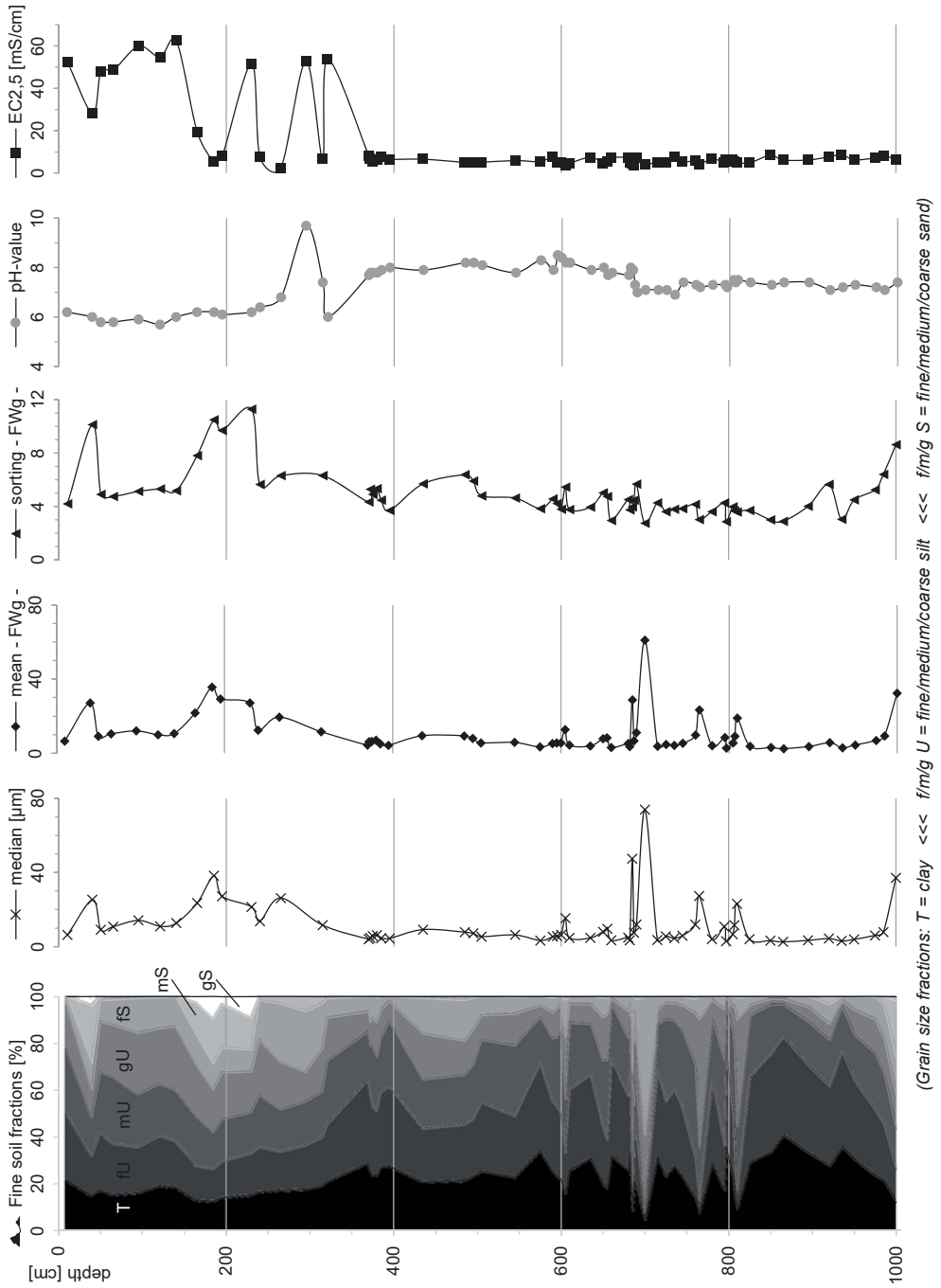

Source: Own illustration

Figure 3.3.8: The description and analytical data from core B04-A reveals a major change from ~400 cm upwards. The Ca/S-ratio has r^2=0.42 for facies 3-4 (343-660 cm) and r^2=0.09 for facies 5-6 (from 660-913 cm). The Al/Fe-ratio shows an opposite behavior with r^2=0.09 in facies 3-4 and r^2=0.66 in facies 5 and 6.

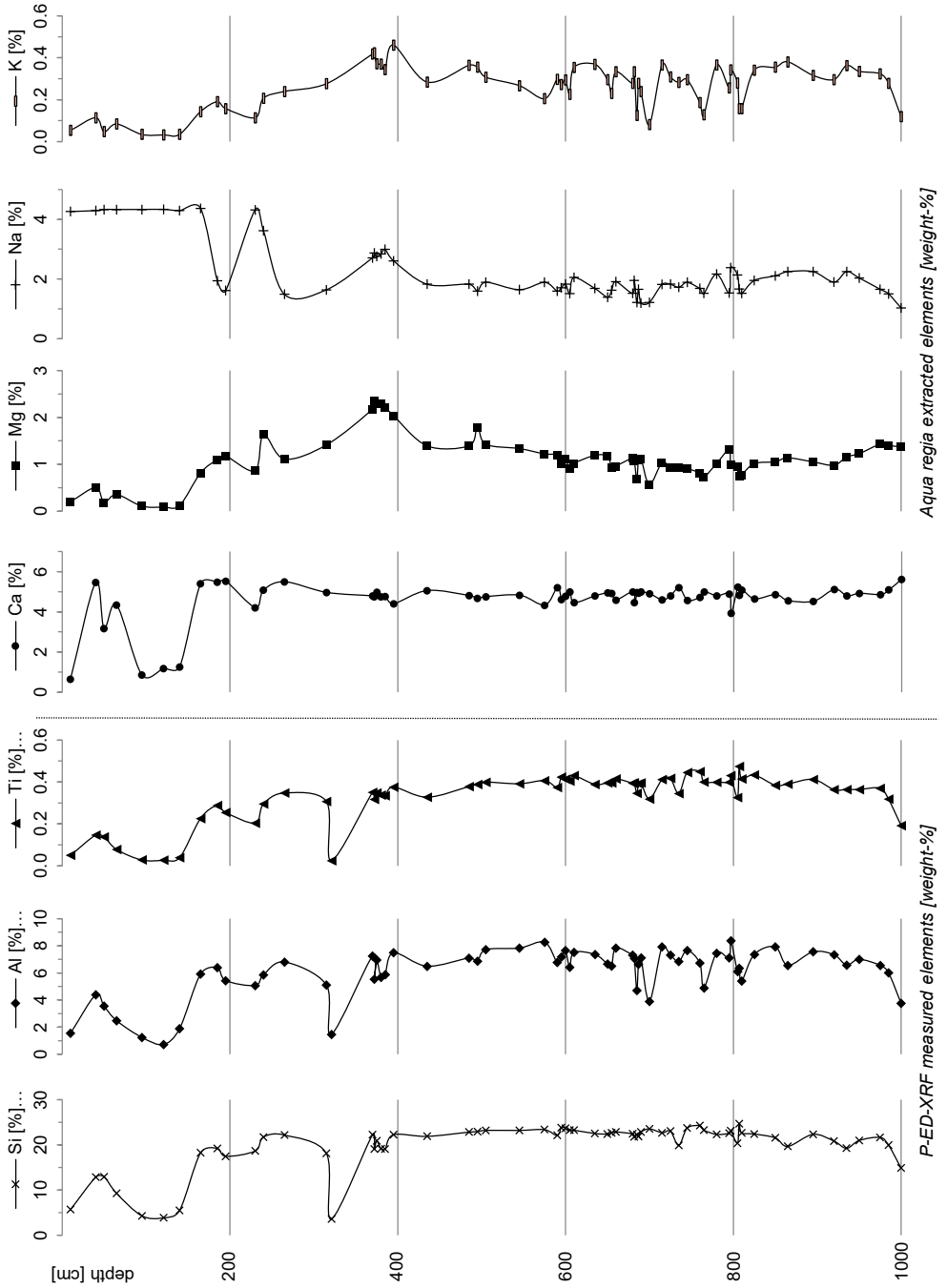

Continuation of Fig. 3.3.8

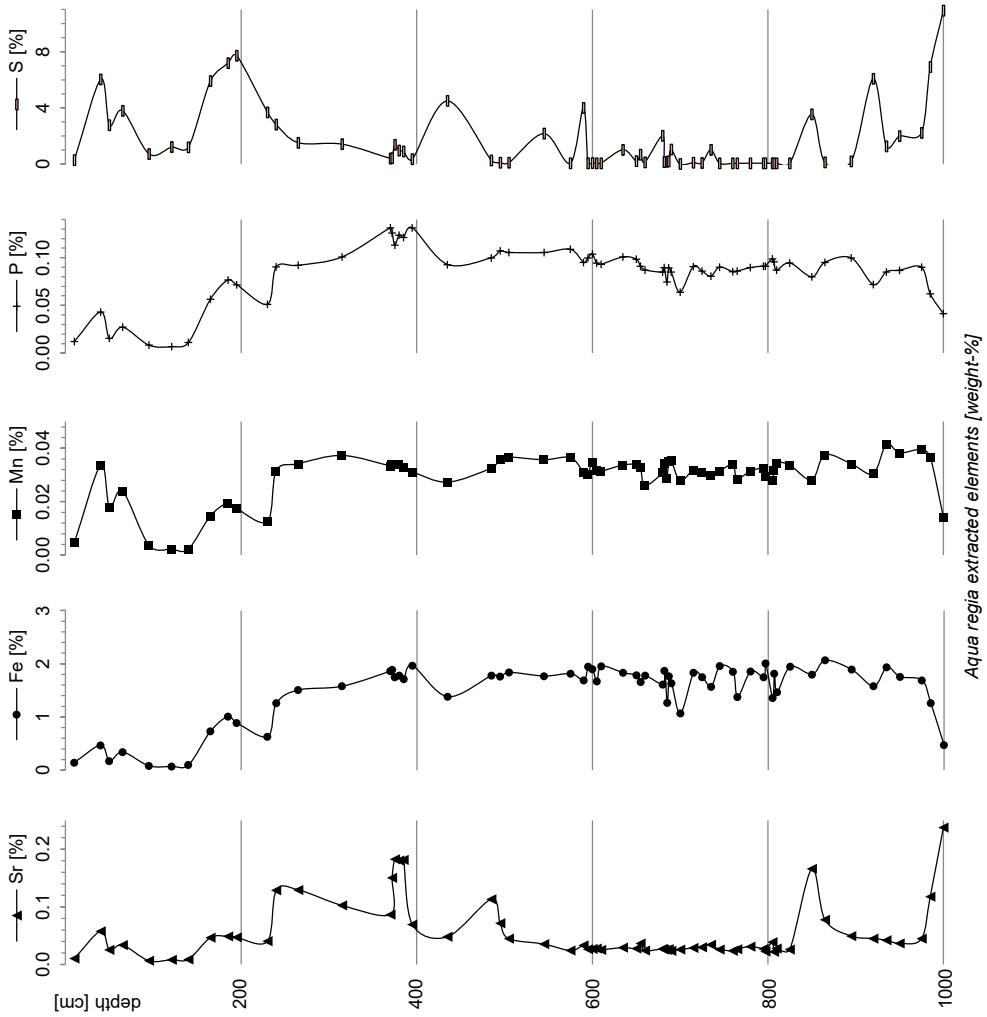

Source: Own illustration

The electric conductivity rises to strong saline conditions > 5.0 mS/cm above facies 3-4, while contents of Mg-, K-, Sr- and S-ions already increase within facies 3-4 above 560 cm. This points to a diagenetic conversion of Ca-sulfates with the typical occurrence of K-Mg-sulfates like polyhalite and Kieserite in K-Mg-rich brines (Okrusch & Matthes 2010). The reduced range in grain-size supposedly leads to low variation in Si-, Al-, Ti- and Fe-values throughout the unit above 560 cm depth. The contents of Al, Ti, Fe and Mn slightly decrease between 560 cm and 370 cm depth which is comparable to the values of combined section S03-A-I & -II.

Geochemical properties are changing entirely with facies 1-2. The abundant salts in massive crusts and idiomorphic crystallization induce layers with highly reduced amounts of Al and Fe-ions. pH-values decrease to about pH = 6.0 and electric

Figure 3.3.9: Aluminum and Titanium based potentials for biogenic silicates (BSi) in playa related sediments. All peaks are comparably small and broadly related to allochthonous inputs. The potential for biogenic silicates, like diatoms, is low.

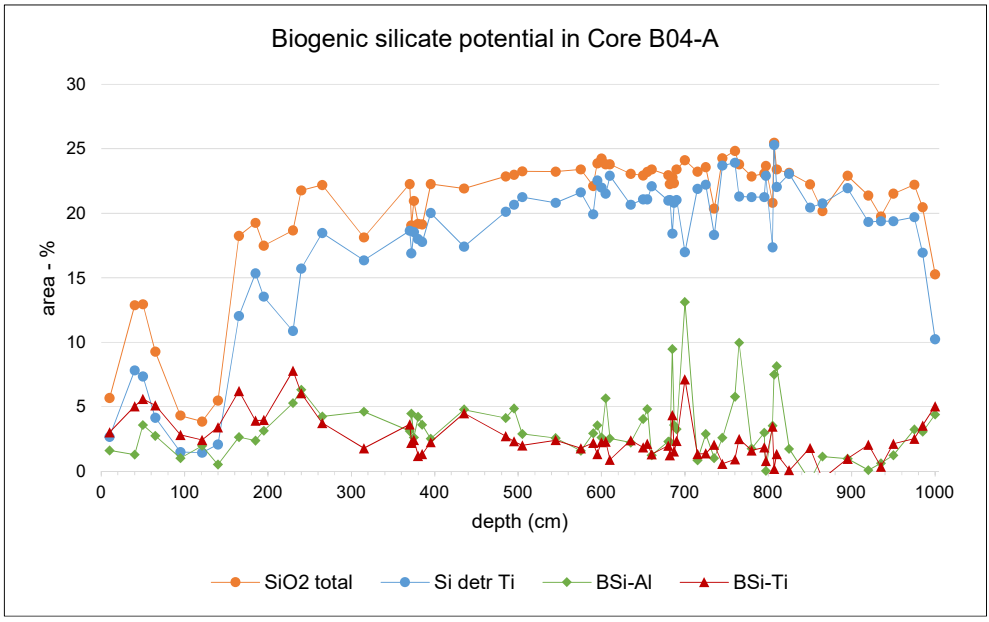

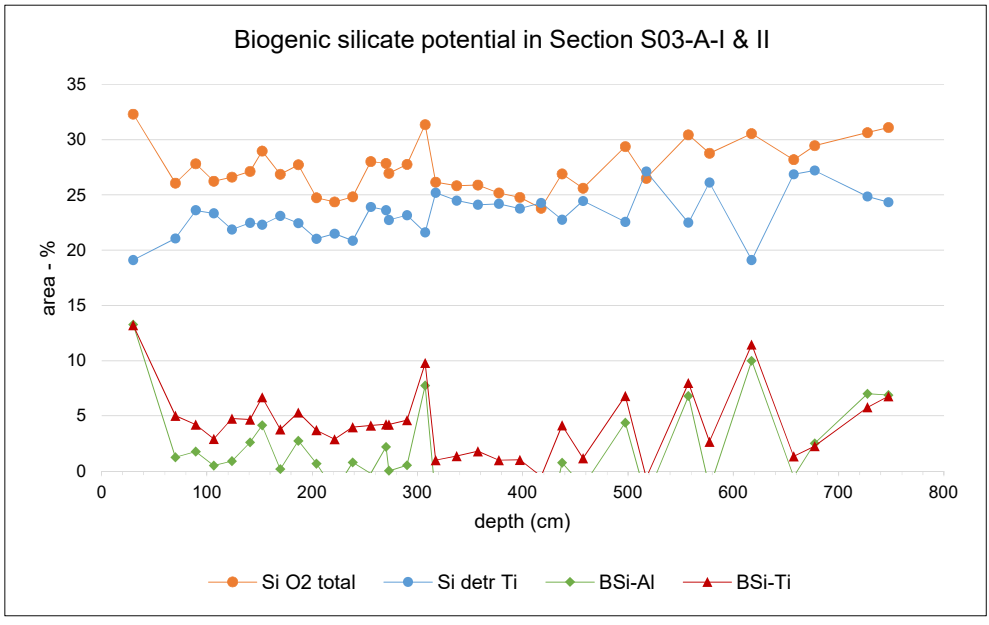

Source: Own illustration

conductivity raises to extremely saline conditions depending on the halite content. A high variability can also be observed in Ca- and S-values where Gypsum is precipitated or deposited and was also measured using XRD at the muddy layers.

Biogenic silicate potentials

In order to unveil detailed environmental conditions of morphodynamic phases in Damghan Playa, the analyses of biogenic sediments and microfossils has a key role, when providing environmental proxies (cf. Snyder et al. 2001). The potential for diatoms is of special importance in extreme environments like playa lakes, in which organic carbon preservation is low. In order to identify playa deposits with high potential for biogenic silicate – e.g. from diatoms – the Si/Al- and Si/Ti-ratios of combined section S03-A-I & -II and core B04-A were investigated (Brown et al. 2007; Francus et al. 2009; Brauneck 2010). Consequently, layers with high detrital input were selected as a reference for detrital Si/Al- and Si/Ti-Ratios. The mean ratios calculated for this layers were Si/Al = 5.38 (n=12) and Si/Ti = 97.43 (n=12) in Section S03-A-I & -II, and for core B04-A, these values are Si/Al = 3.61 (n=15) and Si/Ti = 96.83 (n=15). To prevent negative values, an additional factor (a) was applied in the formula (7), which was used for the calculation of BSi-Al, from p-ED-XRF-measured element contents [area-%]. Formula (7) was accordingly used for calculating BSi-Ti, when using Ti values instead of with Al [area-%]:

$$BSi - Al\,[area - \%] = Si\,[area - \%] - (a \times Al\,[area - \%]) \tag{7}$$

The investigations revealed very low potentials of biogenic silicates and local silicate peaks were small and not significant to an occurrence of biogenic silicate (Fig. 3.3.9).

3.4 Chronological order of investigated landforms and landform-genesis

Together with the stratigraphic correlation of the landforms a chronological correlation was developed. The map units could be preliminary grouped by their relative age. This was based on the relative order of stratigraphic layers in their vertical extent and the lateral succession of distinct alluvial fan surface generations, which are representing the map units (Tab. 3.4.1). The calculation of absolute ages from luminescence measurements could validate and refine the stratigraphic order and the correlation of related morphogenetic processes. Also, the OSL measurements revealed the uncertainties regarding sufficient bleaching within distinct stratigraphic features of alluvial fans.

Table 3.4.1: OSL sample and section descriptions with map units.

Lab No	Map unit	Section	Layer	Depth [cm]	Elevation [m a.s.l.]	Layer description
GI 44	$Q^{al}0$	S03-B-I	4	30	1 140	channel fill, fine sand with gravel
GI 45	$Q^{al}0$	S03-B-I	8	130	1 140	tilted, stratified pebble with sand
GI 46	$Q^{al}0$	S03-B-I	9	150	1 140	silty-sandy sediments
GI 47	$Q^{al}1$	S03-B-II	3	30	1 140	channel fill sediments
GI 48	$Q^{al}1$	S03-B-II	6	130	1 140	tilted, stratified gravels and sand
GI 49	$Q^{al}1$	S03-B-II	8	150	1 140	silty-sandy fine sediments, unstructured
BT979	P^{er}	S03-A-I	2	89	1 150	bioturbation in loamy sands
BT980	P^{er}	S03-A-I	3	170	1 150	hardened loamy silts
BT981	P^{er}	S03-A-II	3	70	1 150	hydromorphic altered silts
BT982	P^{er}	S03-A-II	7	260	1 150	undefined silts with layered gravels
GI 50	$Q^{al}0/Q^{ap}1$	S03-C-I	2	40	1 196	pebble and gravel in channel fills
GI 51	$Q^{ap}1$	S03-C-I	6	140	1 196	cemented layers of gravels
GI 52	$Q^{ap}2$	S03-D-I	2	40	1 238	debris flow lobe
GI 53	$Q^{ap}2$	S03-D-I	4	90	1 238	cemented debris flow lobe with stones and gravel

Source: Own table

OSL ages and age distribution of the sediments

Despite the application of an OSL protocol, which is adapted for calculating insufficiently bleached quartz grains, the ages derived from any sample must be considered as maximum ages (Tab. 3.4.2; Fig. 3.4.1).

Table 3.4.2: OSL ages and luminescence properties of the sediments. All measurements are given with deviation values of ± 1 σ.

Lab No	Map unit	Section	Layer	U (ppm)	Th (ppm)	K (%)	Dose rate (Gy/ka)	Equivalent dose (max Gy)	OSL age (max ka)
GI 44	$Q^{al}0$	S03-B-I	4	2.04 ± 0.15	4.4 ± 0.49	1.83 ± 0.06	2.60 ± 0.26	4.8 ± 0.6	1.85 ± 0.3
GI 45	$Q^{al}0$	S03-B-I	8	2.13 ± 0.15	4.49 ± 0.50	1.96 ± 0.06	2.73 ± 0.28	7.9 ± 0.3	2.89 ± 0.31
GI 46	$Q^{al}0$	S03-B-I	9	2.09 ± 0.15	4.22 ± 0.48	1.57 ± 0.05	2.35 ± 0.24	4.8 ± 0.2	2.05 ± 0.22
GI 47	$Q^{al}1$	S03-B-II	3	2.11 ± 0.25	6.63 ± 0.81	2.14 ± 0.06	3.03 ± 0.31	22.3 ± 0.8	7.36 ± 0.8
GI 48	$Q^{al}1$	S03-B-II	6	2.11 ± 0.23	5.69 ± 0.75	2.43 ± 0.07	3.22 ± 0.33	32.5 ± 3.9	10.09 ± 1.6
GI 49	$Q^{al}1$	S03-B-II	8	2.16 ± 0.22	5.46 ± 0.74	2.18 ± 0.07	2.98 ± 0.31	18.9 ± 1.2	6.34 ± 0.77
BT979	P^{er}	S03-A-I	2	2.33 ± 0.19	6.21 ± 0.50	1.89 ± 0.06	2.82 ± 0.29	30 ± 3.7	10.85 ± 1.73
BT980	P^{er}	S03-A-I	3	1.88 ± 0.15	8.05 ± 0.64	1.79 ± 0.05	2.72 ± 0.28	36.4 ± 3.0	13.52 ± 1.78
BT981	P^{er}	S03-A-II	3	2.62 ± 0.21	5.2 ± 0.68	1.64 ± 0.05	2.61 ± 0.26	30.6 ± 3.8	12.02 ± 1.95
BT982	P^{er}	S03-A-II	7	2.93 ± 0.25	7.38 ± 0.82	1.85 ± 0.06	2.96 ± 0.31	161 ± 16.3	54.91 ± 7.99
GI 50	$Q^{al}0/Q^{ap}1$	S03-C-I	2	1.35 ± 0.11	6.49 ± 0.52	1.95 ± 0.06	2.69 ± 0.27	1.6 ± 0.2	0.6 ± 0.1
GI 51	$Q^{ap}1$	S03-C-I	6	2.05 ± 0.20	4.24 ± 0.65	2.24 ± 0.07	2.95 ± 0.30	39.2 ± 4.6	13.3 ± 2.08
GI 52	$Q^{ap}2$	S03-D-I	2	2.65 ± 0.17	4.90 ± 0.56	2.00 ± 0.06	2.92 ± 0.30	42.9 ± 2.3	14.68 ± 1.68
GI 53	$Q^{ap}2$	S03-D-I	4	2.37 ± 0.17	5.68 ± 0.57	1.84 ± 0.06	2.76 ± 0.28	41.4 ± 1.6	15.01 ± 1.62

Source: Own table

Figure 3.4.1: Distribution of OSL ages and quaternary units (standard error indicated in red).

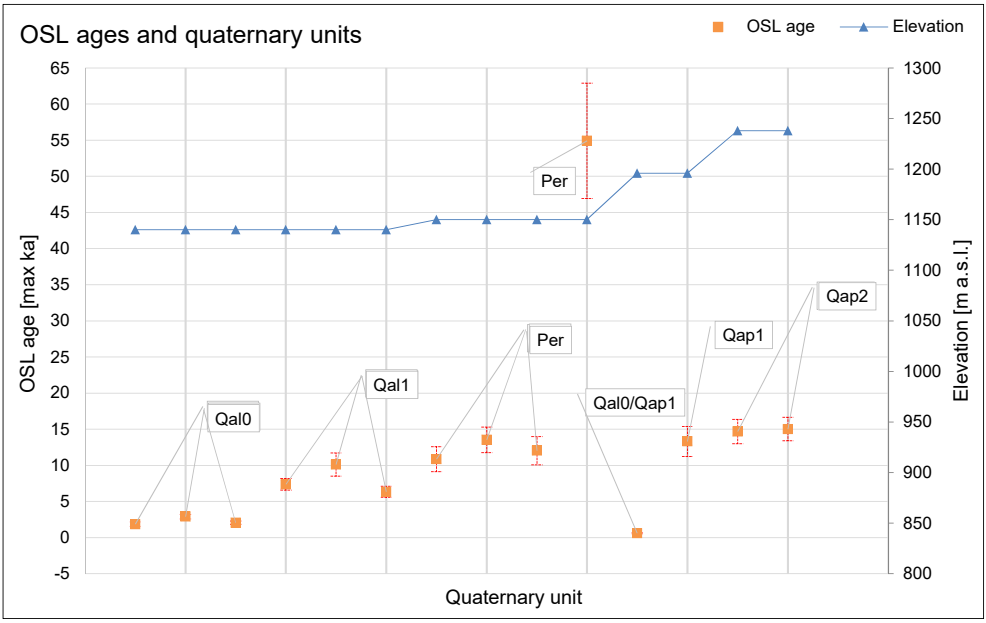

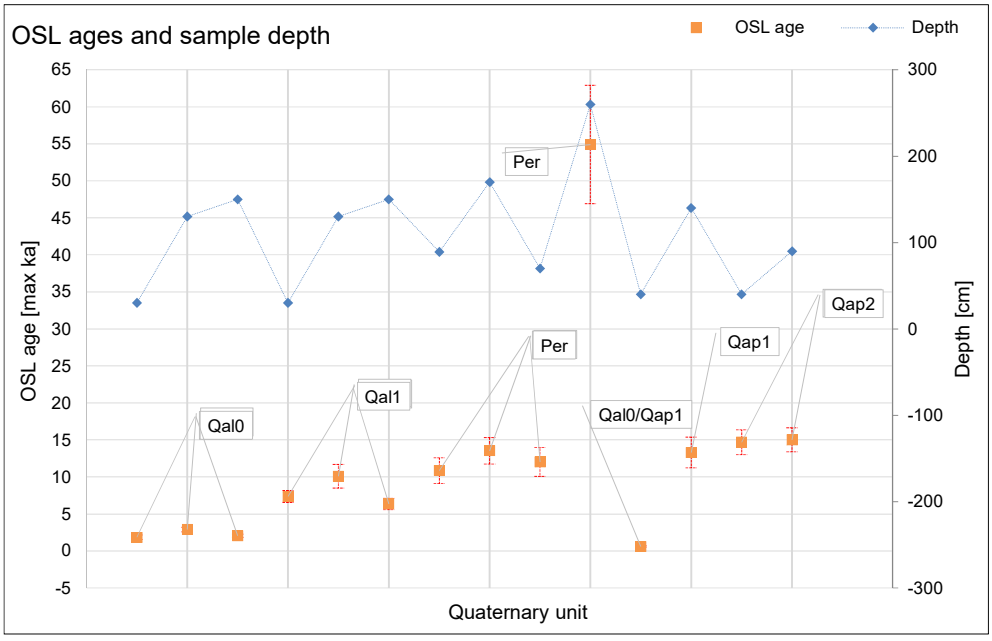

Source: Own illustration

Overall, the OSL ages are grouped according to their related map unit, starting with $Q^{al}0$ as the youngest map unit, represented by young alluvial fans from section S03-B-I, with maximum ages between 1.85 and 2.89 ka, and in the recently active depositional lobe (Sample: GI50) with a maximum age of 0.6 ka. The next generation of young alluvial fans – $Q^{al}1$, from S03-B-II – is considerably older and covers ages between maximum 6.34 and 10.09 ka. The eroded lake sediment terrace – P^{er} – shows an extraordinary maximum age of ~55 ka from the deepest sample in S03-A-II, which might be due to insufficient bleaching. The other ages of P^{er} are grouped closer and show the chronological relation to map unit $Q^{ap}1$, which is represented in the deeper layers of S03-C-I. Together they cover maximum ages between 10.85 and 13.52 ka, which may relate these prevalent (Tab. 3.1.1) alluvial fan sedimentations to the Younger Dryas Event (Chap. 5.1). The highest sedimentation age of alluvial fan sediments was measured for $Q^{ap}2$. Here the maximum ages of 14.68 to 15.01 ka indicate a chronological relationship to early MIS 1, before the maximum onset of the Younger Dryas Event.

An increased equivalent-dose-scatter was observed with increased sediment age and in samples with a high amount of coarse grains, unsorted texture and turbulent bedding features, which indicates high energy transport and fluvial to slope-fluvial deposition. This also coincides with phenomena of age inversion, which occurs in young alluvial fans of section S03-B-I and -II. Here, higher ages are measured in layer 8 (B-I) and Layer 6 (B-II), and both are described as layers of tilted and stratified pebble/gravel and sand. The younger ages are derived from fine sediments of layers 9 (B-I) and 8 (B-II), which are representing well-sorted, yellowish silty-sandy deposits, supposedly eroded from the nearby lake terrace. The section further reveals the stratigraphic relation of layer 8 to 9 (B-I) and layer 6 to 8 (B-II), which shows the parallel development of (slope-)fluvial and slack water deposits, occurring in close neighborhood and with abrupt transition between the two sedimentary milieus. Hence the age inversions are explained by bleaching insufficiencies related to the morphogenetic differences of the sediments (cf. Tab. 3.4.1; Chap. 3.2.2.1).

The statistical outlier of sample BT982, with a maximum age of 54.91 ka at S03-A-II is not disturbing the chronostratigraphic order, but it is regarded as a highly overestimated age. A sedimentation that would have taken place some ~55 000 years ago would be corresponding with alluvial fan strata like from Rieben's "*Kharizak Formation – B Alluvium*", which he studied in the Teheran Alluvium. Like the underlying, Miocene-Pleistocene "Hezardareh Formation" (Rieben 1955) this formation is slightly tilted, by neo-tectonic activity and corresponds to the standardized map unit $Ng^{c;\ 1-?}$, which is observed in most of the intramontane basins in North Iran (Alavi 1996; Rezaeian 2008), and which was also mapped at higher elevations in the study area (cf. $Q^{ap}5$; Vaziri & Majidifard 2000). The description and field evidence of these known older materials and their structural and textural differences, contradict a temporal synchrony of $Q^{ap}5$ and the lower layers of P^{er}.

Chronostratigraphic order and landform-genesis

The statistical outliers of ~55 ka and 0.6 ka are not disturbing the chronostratigraphic order of the sediments and the previously estimated chronostratigraphic order of

sediment bodies and alluvial surfaces, which are represented by the map units, is thoroughly confirmed by the OSL ages. Also the distinction between layers, only reworked by secondary processes (e.g. sample GI50) and layers of primary aggradation (sample GI51) is evident in the OSL data.

The temporal distinction between $Q^{ap}1$ and $Q^{ap}2$ is based on field evidence and unconfidently confirmed by the ages. Additional OSL samples of $Q^{ap}1$ were taken from section S03-C-II and will provide more information about this relationship.

The morphogenesis of the small alluvial fans below the fine sediments terrace is explained by a small scale shift of the incised channel and the active depositional lobe of the alluvial apron segment, which controls the studied sections. This spatial distinction is completed by the temporal determination of the alluvial fan generations, which are separated by age differences of minimum 3.45 ka to maximum 8.24 ka, without any evidence for a parallel development. However, due to the poor OSL qualities of the samples and the restriction to maximum ages, a parallel development cannot be excluded, entirely. But the close neighborhood of the geomorphic systems of this two alluvial fan generations, together with their close connection to the same alluvial apron segment, reduces the uncertainties from eventually strongly differing morphodynamics, regarding their control on deposition and bleaching qualities.

The sections S03-A-I & II and S03-B-I and -II are connected directly to the fine sediments line, which also represents the fault-line of Damghan Fault. Evidence for a high fault activity is correlated to the devastating Qumis Earthquake, which happened 856 A.D. (Hollingsworth et al. 2010). All OSL ages from the related sections are older than this important event, and thus, a deposition triggered by the earthquake could not be identified. Neo-tectonic activity of this fault is discussed in chapter 4.1. Anyway, the effect of slow uplift of the fine sediments, which are constituting the terrace cannot be excluded. This should be considered regarding the high age of sample BT982.

4 Discussion

4.1 Correlation of basin morphology and playa sediments

Morphodynamic phases

The granulometric properties of the samples revealed a sensitivity to major changes in terrestrial as well as in lacustrine sediments. This can be a key for the correlation of paleo-lake geomorphology with depositional features of the playa sediments. The statistical properties calculated from laser granulometric measurements using GRADISTAT (Blott & Pye 2001) show distinct characteristics of facies lithology in core B04-A (Fig. 4.1.1). The adoption and comparison of the approach of Folk and Ward with the stratigraphic structures in the studied sections gives a first idea about the sediment source interpretation (Folk & Ward 1957). Hence, the observed high mean/skewness-ratios in core B04-A can be an indicator for high energy events with a grain size distribution typical for fluvial events and high mean grain sizes. In the case of the Damghan cores, low values are a result of low mean grain sizes and high specific grainsize distribution supposedly caused by combination and reworking of different well sorted sediment types. This combination can be a result of mixed phases of several individual and originally well sorted fluvial or lacustrine sediments. In addition, it can reveal a combination of aeolian and lacustrine sediments, which showed good sorting bevor erosion and re-accumulation (Folk & Ward 1957). The particles deposited without any sorting are typically observed in flash flood and debris flow layers. Therefore, a high energy transportation is also indicated in the data with high median/sorting-ratios. Contrary to this, low values show small grainsize and increased sorting and indicate slack water sedimentation and little fluvial activity.

In Core B04-A facies 1-2 has two noticeable peaks in granulometric data from 10-40 cm and 140-240 cm. The first phase has a higher median/sorting-ratio and both feature shifting mean/skewness-ratios suggesting initial homogeneity of unsorted sediments followed by a growing influence of well or considerably different-sorted sediment source or a better sorting transportation process (Fig. 4.1.1). Units from facies 3-6 show the general twofold milieu of playa-sedimentation seen in the results before. Correlation of facies 5-6 peaks in median/sorting-ratio and Ti/Al-ratio reflects the short termed input of allochthonous material into the playa sediments during this period. In opposite to this a parallel trend of reducing Ti/Al- and Fe/Al-ratios can be observed with the onset of facies 1-2. This can be supposed as a signal of sediment transport lasting over longer distance and time, resulting in an increasing depletion of heavy minerals bearing titanium-iron-oxides (Chen et al. 2013). This observation is a strong argument for the idea of retreating lake levels since early- to mid-Holocene, and for the succession of lake oriented cultural landscape elements, surrounding Damghan playa with 'Tepe Hissar' – onset ~7 000 years ago – as the most famous ancient city (Thornton & Rehren 2009; Fig. 4.1.2).

Figure 4.1.1: The outlined facies of core B04-A (from Büdel et al 2017). There are two remarkable peaks in Facies 1-2, highlighting two main phases of allochthonous sediment input at 10-40 cm and at 140-240 cm.

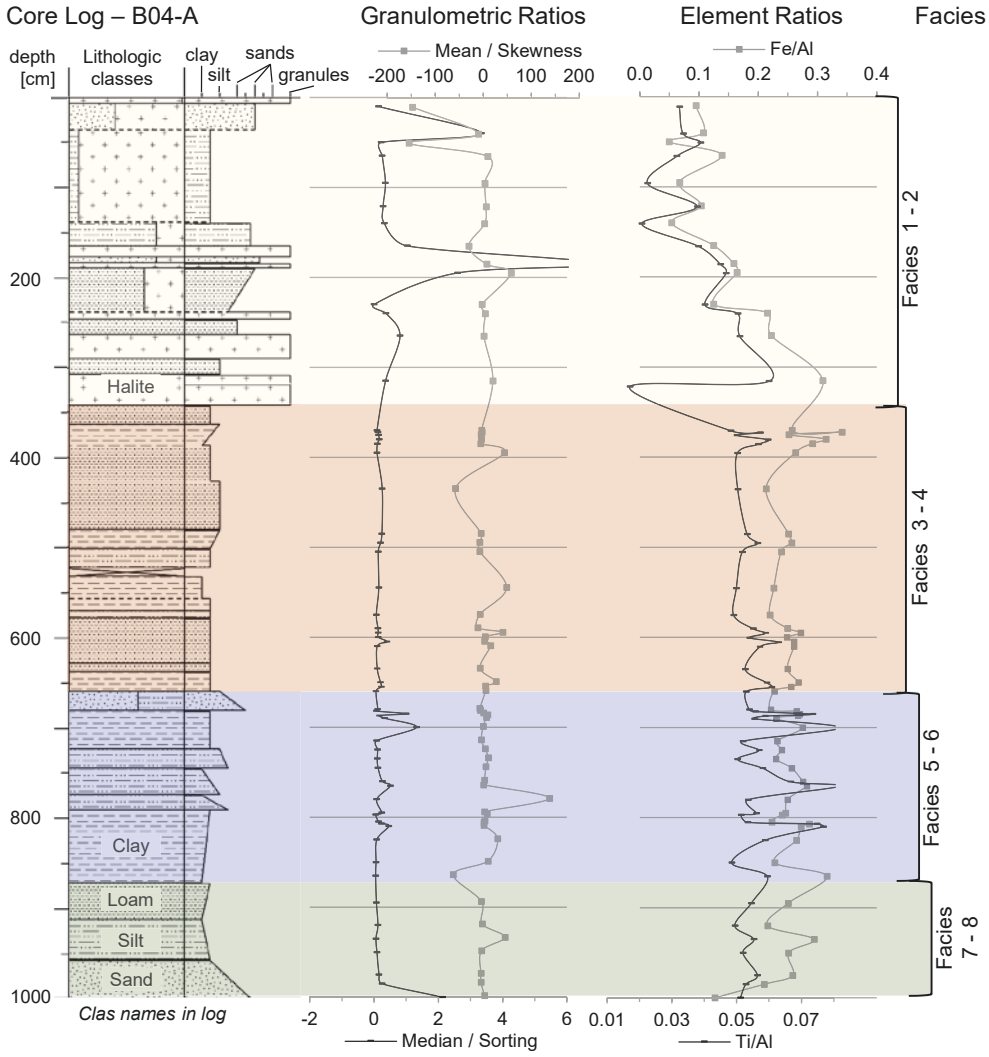

Source: Own illustration

Regarding the postulated lake level retreat, there is evidence for increased erosion and accumulation activity commonly triggered by lowered erosional basis. A young generation of small alluvial fans has developed directly below the fine sediments line and is partly fed by erosional material from these fines. The geomorphological mapping and stratigraphic studies of the sections revealed two distinct surface ages, dividing the fans in a younger and an older accumulation phase. The alluvial fans stratigraphy shows layers of eroded fine sediments, which were reworked and re-accumulated in the alluvial fan system, and thus they are frequently

Figure 4.1.2: The correlation of the lake related sediments shows several accumulation phases during the time of the maximum lake extent. After the onset of desiccation and lake retreat, sedimentation at the eroded lake terrace (site: S03-A-I/II) ends and two generations of alluvial fans develop below the old terrace level, while the playa center (site: B04-A) is dominated by salt crusting and flooding during extreme rainfall events.

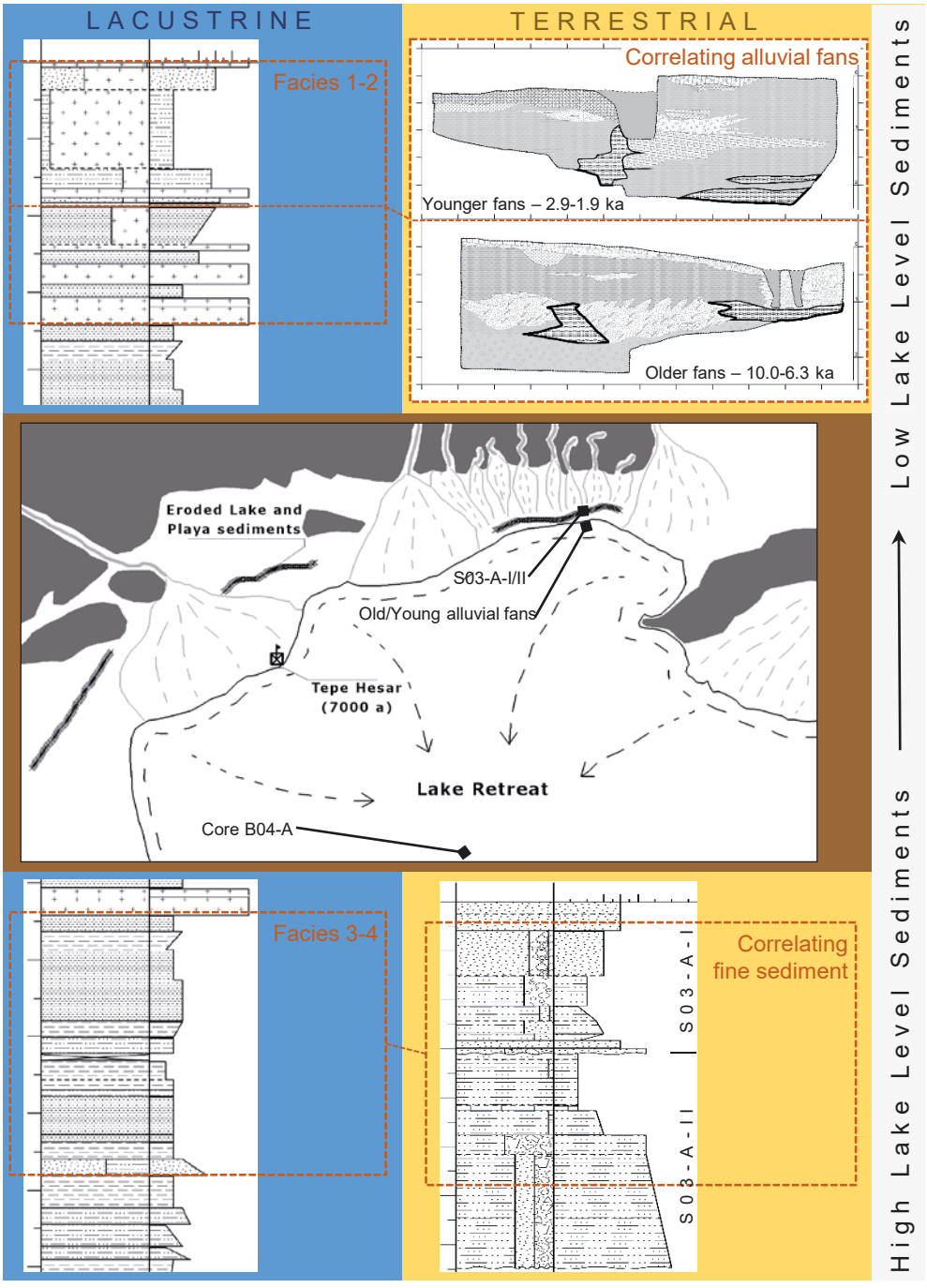

Source: Own illustration

intercalated with debris flow materials (Fig. 4.1.2). This setup of young alluvial fan activity in two phases and the two phases of increased high energy sediment transport observed in core facies 2 may be found in the same origin – the retreat of a former high lake level in Damghan Basin.

Neo-tectonic activity

The neo-tectonic activity within the aforementioned Damghan Fault system (Chap. 1) considerably affects the development of even young alluvial fans. Hollingsworth et al. also regard the lake-terrace-like fine sediment outcrop as a possible fault related phenomena of uplifting (Vaziri & Majidifard 2000; Hollingsworth et al. 2010). Hence, fault activity becomes a critical aspect when interpreting depositional history of the sediment bodies in the area. The GPR measurements conducted during this study yielded potential evidence for fault activity affecting even the youngest sediments of map unit $Q^{al}0$. Hollingsworth et al. (2010) discussed the activity of Damghan fault most recently. They argue that Damghan "Fault" activity during 856 A.D. Qumis Earthquake is likely and show ruptures from an excavated trench, located about 25 km north-west from Damghan City. The ruptures cut the sediment layers in the described section AT3 and were chronologically classified using ^{14}C-ages from the disrupted layers. The rupture time windows reveal a least phase of fault activity at about the same time as the Qumis Earthquake, as well as relative tectonic stability since this event until now. The offset of the layer disturbed just by this latest event is about 30 cm, which is in about the same dimension as the potential layer offset observed in the GPR measurements of this study (Chap. 3.2.1). Therefore, this major neo-tectonic event is well documented in the region, and appears to be causal for at least a minor part of sedimentation on top of the young alluvial fans, but not for the general sedimentation phases and morphodynamics in the setting of the fine sediments and the younger alluvial fans.

4.2 Autochthonous and allochthonous gypsum contents

Gypsum contents in saline lake environments show varying strontium concentrations in their gypsum minerals (Büdel et al. 2017). This can be an indicator when distinguishing allochthonous and autochthonous genesis of evaporite precipitation. Thereby, strontium has proven as a useful indicator for palaeosalinity in several studies (cf. West 1973; Kushnir 1982; Warren 2016). In brines with negative water balance strontium becomes higher concentrated and the high Sr-concentration is primarily incorporated into the precipitated gypsum lattice by replacing Ca^{2+}-ions, or in discrete celestine minerals ($SrSO_4$) (Playà & Rosell 2005; Warren 2016). Pedogenic gypsum shows normal Sr-concentrations around 2200 ppm, when it originates from eroded and transported sediments. Low Sr-contents are regarded to represent dilution processes by increased fluvial input and high detritus supply (Schütt 2004).

Figure 4.2.1: Sulfur and strontium distribution in core B04-A and in terrace section S03-A-I & -II. Comparable increasing strontium values appear in facies 3-4 of core B04-A above 545 cm and in section S03-A-I & -II above 370 cm. Where they coincide with a raised sulfate content (inverted X-axis) they are related to autochthonous gypsum precipitation. S/Sr-ratio is shown without axis-values. Note the highlighted sulfur maximum of S03-A-I & -II and a correlating peak in B04-A.

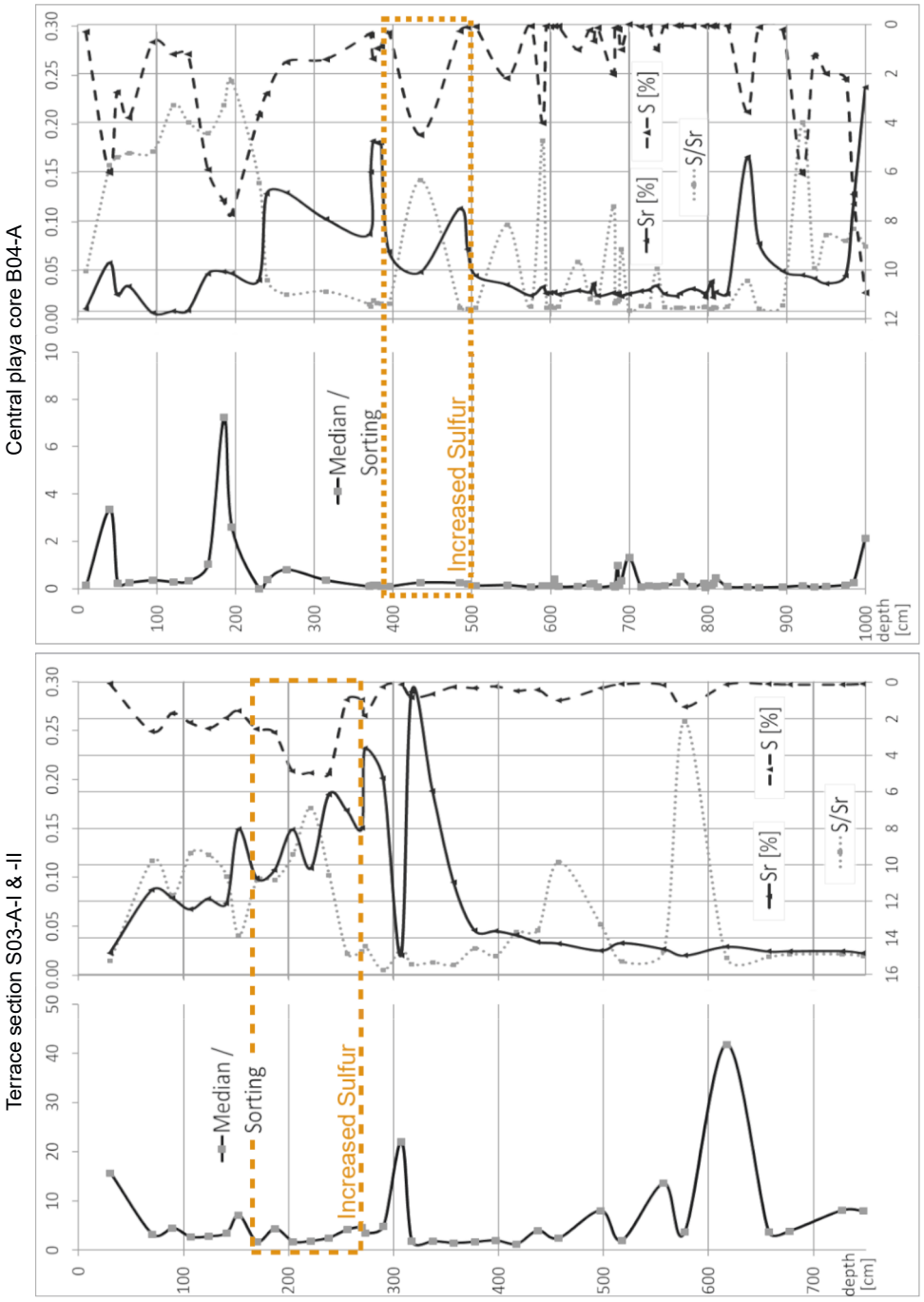

Source: Own illustration

Figure 4.2.1 shows the distribution of strontium and sulfur in both playa sediments and terrestrial sediments. Two peaks of the S/Sr-ratio in section S03-A-II at a depth of 570 and 460 cm are due to slightly higher S-concentrations and coincide with reduced Sr-contents during phases of slack water sedimentation. This relationship establishes throughout the section and suggests autochthonous gypsum precipitation in lower concentrated brines or moderate allochthonous gypsum supply from terrigenous sources. An increase in Sr-content sets in at about 370 cm depth. From 370 to 250 cm Sr-content increases prior to S-contents, resulting in a low S/Sr-ratio. At 220 cm Sr-concentration begins to decrease but S-contents remain high at first and then slowly decrease towards the top. In the uppermost layer of section S03-A-II the Sr-concentration is reduced again to the lowest concentrations, supposedly due to a decreased water availability.

The sulfur distribution of core B04-A below 340 cm, is roughly comparable to those of the total section S03-A-I & -II. The first major S/Sr-peak at a depth of 570 cm is not complemented by an increased Sr-concentration. Thus, allochthonous supply of gypsum by moderate transportation rates in the feeding streams is expected. Subsequent layers in facies 3-5 show common behavior of increased strontium contents that correspond to an increase in sulfur. A sharp increase in strontium content occurs in core B04-A in facies 3 and 4, from 545 cm upwards the core. Again, peaks of Sr-enrichment do not coincide with higher sulfur concentrations, and may therefore be associated with allochthonous sources, e.g. from deflated, clay mineral rich soils, which are exposed by a decrease of vegetation. However, an overall core-upward trend of increasing sulfur and strontium concentration was measured and evidence for slightly increased transport energy was observed. With the onset of high energy phases in facies 1-2, a depletion of Sr sets in and high S/Sr values are almost entirely due to allochthonous sulfur supply. This implies roughly comparable water chemistry in two correlating segments of the S03-A-sections and the core. The first segment locates at a depth below 500 cm in S03-A and correlates with core facies 5-6. Accordingly, the second correlation appears at the more homogenous layers of section S03-A above 500 cm depth and connects these layers with facies 3-4 of the playa core. Facies 1-2 seems not to be represented in the layers of S03-A-sections, which would fit the thesis of a retreating lake level and fading sedimentation of fine sediments at this remote terrace locality, during ongoing sedimentation in the playa center.

The highest sulfur content in S03-A-sections was measured in layer 4 (S = 5 %), which consists of silt with minor clay and gravely sands at the bottom (Büdel et al. 2017). Measurements of facies 3-4 yield S = 2.0-4.5 % between 400-600 cm depth (Fig. 4.2.1 & 4.2.2). Sources for allochthonous gypsum contents in facies 1-2 may be found in young alluvial fans where values of highly concentrated sulfur – S > 10 % – were measured in reworked fine sediments. Analysis of older alluvial fan sediments in proximal location yielded high sulfur contents in hardened footwall layers (Fig. 4.2.2).

In highly concentrated brines, sulfates may also crystalize with K-, and Mg-oxides, to polyhalite – $K_2Ca_2Mg(S0_4)_4 \, x \, 2H_20$, or to kieserite – $Mg(SO_4) \, x \, H_2O$ (Okrusch & Matthes 2010). There are indications of a post-sedimentary replacement of gypsum or anhydrite by these minerals in facies 3-4 of core B04-A, where Mg-, K-, and S-ion

Figure 4.2.2: Relationships between core facies 3-4 and “Eroded lake and playa deposits”, represented here in Section S03-A-I can be established regarding comparable sulfur content variation between 2-5 % (from Büdel et al. 2017). The map shows a potential sulfur storage in the studied profiles, and thus gives an overview over the potential sulfur sources along the transportation path. Values are roughly estimated by multiplying the layer’s sulfur contents (S % - cf. laboratory results), with their areal percentage (area %) of section extents, which gives a broad impression about sulfur distribution as it may be induced from the section observation.

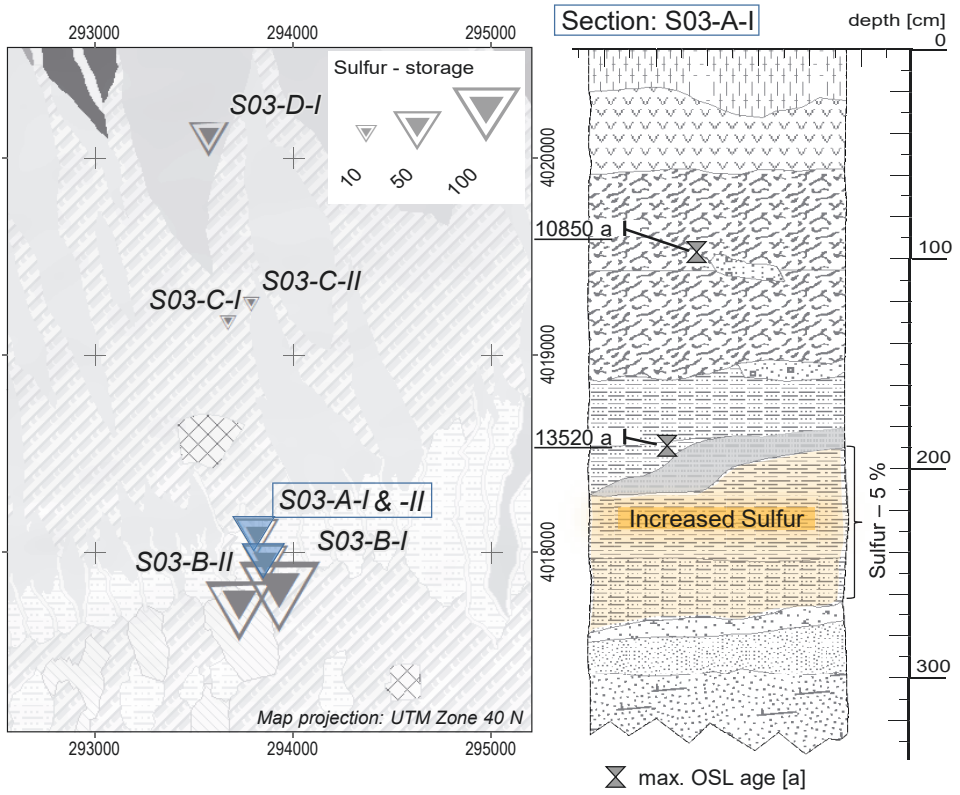

Chrono-Stratigraphic Units

- Aa - Anthropogenic accumulation
- Qf0 - Fluvial Terraces and Floodplains
- Per - Eroded Lake and Playa Deposits
- Qal0 - Recent Alluvial Fan Sediments
- Qal1 - Recent Alluvial Fan Sediments
- Qap1 - Eroded Fans and Aprons
- Qap2 - Eroded Fans and Aprons
- Qap3 - Eroded Fans and Aprons
- Qap4 - Eroded Fans and Aprons
- Qap5 - Eroded Fans and Aprons

Layers

- A-horizon (Solonchak)
- B-horizon in gravelly sands
- bioturbation in loamy sands
- gravel-lense
- hardened loamy silts
- undefined gravels and silts
- silt with very few clay
- coarse silt and gravelly sands
- silts with loam and gypsum
- loamy-silty sand
- interlayered gravel and sand

Source: Own illustration

contents raise without an increase of Ca-values. The hyper-concentration of ground and surfaces water controlled brines and a constant source of Mg- and K-ions is provided in the investigation area by underlying Miocene marls of the Upper Red Formation – unit M^r (Chap 3.1.2.7, Appendix II).

4.3 Chronostratigraphic framework

An important finding of this study is a major shift from less saline conditions with intercalated allochthonous and autochthonous sedimentation to extremely saline conditions with the development of massive salt crusts in the core's top 3.4 m. The according changes of physical and chemical properties may indicate a transition from a fluvial active Pleistocene to a wet early Holocene and then to arid mid Holocene conditions. These three stages in north-eastern Iran are derived from previous investigations (Stevens et al. 2006; Walker & Fattahi 2011) and their correlation with findings and chronostratigraphic framework from our study is discussed below (from Büdel et al. 2017). Beside this signal from the core, the sequence-stratigraphy of terrestrial sediments, reveals parallel alluvial and fluvial progradation. This took place in at least two distinguishable phases, which were eventually separated by the middle Holocene dry period, which was observed in several archives in Iran before (Wasylikowa et al. 2006; Stevens et al. 2006). According to aforementioned data (cf. Chap. 1.2.2), an onset of lake level retreat in Damghan at about ~8 500 years ago may be supposed. This would result in a sedimentation of 3.4 m in 8 500 years and a linear sedimentation rate of 0.4 mm yr^{-1}, if the onset of salt crusting together with the decreasing Ti/Al-ratio in Facies 1-2 of core B04-A does really reflect the retreat. The remarkable step of the pH-value at 687 cm depth in core B04-A can also be seen in 500 cm depth of Profile S03-A, and should be considered as a further indication of changing conditions. Aforementioned studies on lake levels coincidently point out the Younger Dryas Event as a phase of cold and dry climate. This period lasted from maximal 12 800 years ago on to at least 10 500 years ago, with a significant shift in general climatic conditions (Wasylikowa et al. 2006; Wick et al. 2003; Çağatay et al. 2014). If this remarkable shift is reflected in the step in pH-value in the studied sediments, proximal sedimentation rates can be derived for the time period from 12 800 (maximal onset of Younger Dryas) to 8 500 (onset of last lake level retreat) years ago. This would result in a lacustrine sedimentation of 3 470 mm in 4 300 years in B04-A and a terrestrial sedimentation with more fluvial depositions of 5 000 mm in 4 300 years, as observed in combined section S03-A. Thus, linear sedimentation rates of 0.81 mm yr^{-1} in lacustrine environments and 1.16 mm yr^{-1} in terrestrial sediments are inferred for a period from late Pleistocene to early Holocene. The sedimentation rates are in line with observed geomorphology and are not contradicting the plausibility of the estimated time frame.

The chronostratigraphic framework of the investigated sediments can be established between sediments older than Younger Dryas Event, possibly from the transi-

tional period of MIS I and II, and sediments from youngest morphodynamics, probably from Subboreal and Subatlantic period (cf. Fig. 4.4.2).

Additionally, the OSL ages (Chap. 3.4) broadly support this detailed and independent age estimations, which are furthermore integrating the development of the core, where dating was impossible.

4.4 Morphodynamic history and phases of basin sedimentation

The moprhodynamic indicators from proximal ($Q^{ap}2$) and medial ($Q^{ap}1$) alluvial fan sections bear evidence for a parallel development of the alluvial deposits, below a depth of about 70-100 cm and thus below the activity depth of recent surfaces morphodynamics (Chap. 3.2). Furthermore, the mapping of the abandoned surfaces $Q^{ap}1$ and $Q^{ap}2$, also reveals their systematic relationship to the eroded playa sediment terrace of P^{er} (Chap. 3.1; Appendix I). This, together with the sediment max. ages of about ~13 ka for both, P^{er} surface and $Q^{ap}1$ main body, validates the hypothesis of closely related and intercalated slack water deposits and distal alluvial apron deposits. Hence, where the fine sediment terrace is prone to surface erosion and denudation, the directly associated alluvial fan surface belongs to $Q^{ap}1$ and dissection has started. Therefore, the termination of the lake terrace P^{er} is directly linked to the alluvial fan surface abandonment of $Q^{ap}1$ and indirectly with the preceding $Q^{ap}2$ (Fig. 4.4.1).

A good correlation of the lake development in Damghan Basin with known lake-related geoarchives in Iran becomes apparent, when integrating the morphogenetic model of the alluvial apron development of Damghan (Fig. 4.4.1) with its chronostratigraphic framework, as discussed above (Chap. 4.3). The oldest aggradation of proximal alluvial fan surfaces with maximum ages of max. 15 000 a is located in the proximal sequence of the alluvial apron (D-I) and may correlate with higher sediment supply in the watershed and moderate humidity. The alluvial fan sedimentation progrades to medial alluvial fan areas (C-I & -II) and continues to the time around max. 13 300 years ago. At the same time, fine sediments accumulate at the distal end of the alluvial apron and thus mark a probable lake level highstand (A-I & -II). The Younger Dryas event, with a steep decrease of humidity, as discussed above may be represented in the abrupt change of geochemical properties of the lake terrace. After this, sedimentation at the lake terrace continued to the time of max. 10 850 years ago, and with a phase of intensified biogenic activity and accordingly increased humidity. Subsequently the lake terrace and higher alluvial fan surfaces got abandoned and erosion set in; represented by the end of sedimentation and onset of erosion at A-I & -II. This happened together with the deposition of a first alluvial fan generation below the former lake shoreline (B-II) during a dry period between max. 10 090 - 6 340 years ago. The youngest phase, represented in the investigated sediments, is the reworking of alluvial deposits in midfan area (C-I) and

Figure 4.4.1: Morphogenetic model of alluvial apron development with integrated OSL-ages. (Site symbols within sketch A refer to brown labels of sketch B).

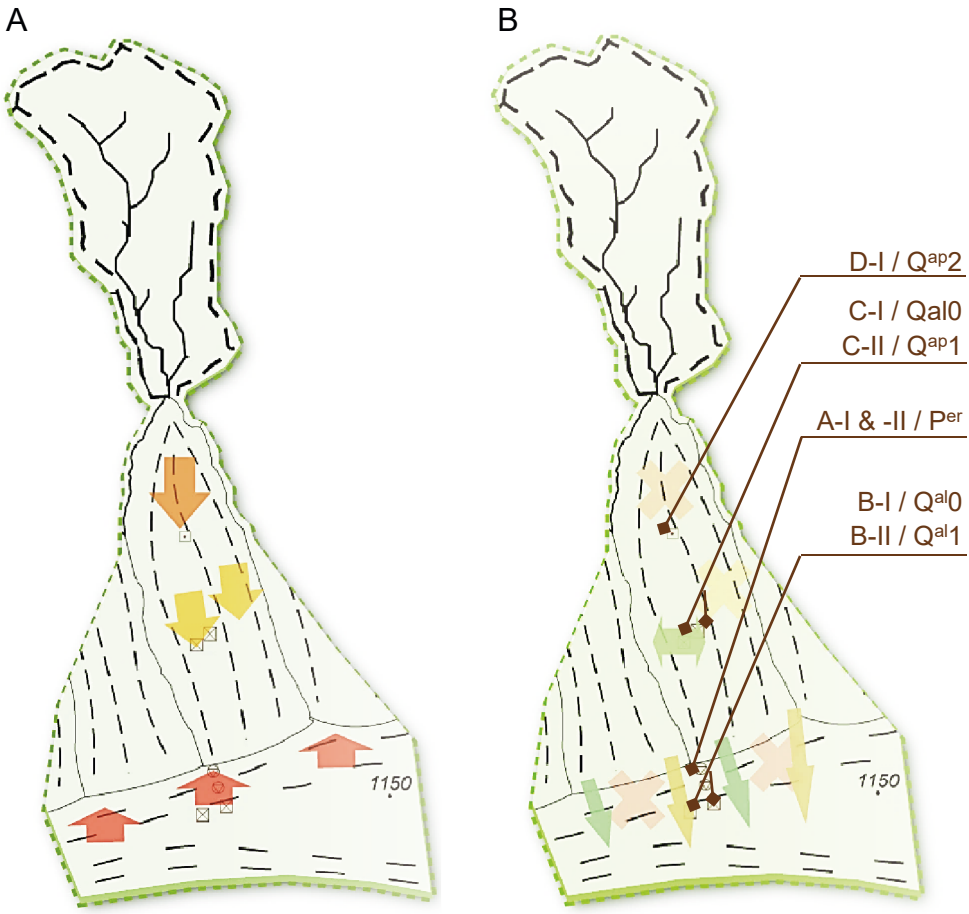

Sketch A

- Phase I, IV (max (55-)11 ka):
  lake level highstand with sedimentation at A-I & -II
- Phase II (max 15 ka):
  aggradation on proximal fan area at D-I
- Phase III (max 13.3 ka):
  aggradation on mid-fan area at C-I & -II

Sketch B

- Phase V (max 10-6.5 ka):
  lake level retreat with following fan toe erosion and progradation of first generation distal fans at B-II
- Phase VI (max 2.9-1.9 ka):
  Lateral shifts of active depositional lobe at C-I controls local progradation of last generation distal fan toe fans at B-I
- Phase VII (max 0.6 ka):
  youngest activity in recent channels and reworking of mid-fan surfaces at C-I

Source: Own illustration

the deposition of a second alluvial fan generation (B-I) below the lake terrace. This phase lasted from max. 1 850 - 2 890 years ago and coincides with hyper saline conditions and extreme low humidity (Fig. 4.4.2).

Figure 4.4.2: The past period humidity for Damghan Basin, as interpreted from morphological and geochemical evidence presented in this study. The reference humidity for the additional lakes and sites is taken from literature (cf. Fig. 1.2.4).
References: Wick et al. 2003, Çağatay et al. 2014 – Lake Van; Bottema 1986 – Lake Urmia; Wasylikowa et al. 2006, Djamali et al. 2009a – Lake Almalou; Sharifi et al. 2015 – Lake Neor; Djamali et al. 2008 – Lake Zeribar; Griffiths et al. 2001, Stevens et al. 2006 – Lake Mirabad; Djamali et al. 2009b – Lake Maharlou; Lisiecki & Raymo 2005 – Benthic $\delta^{18}O$.

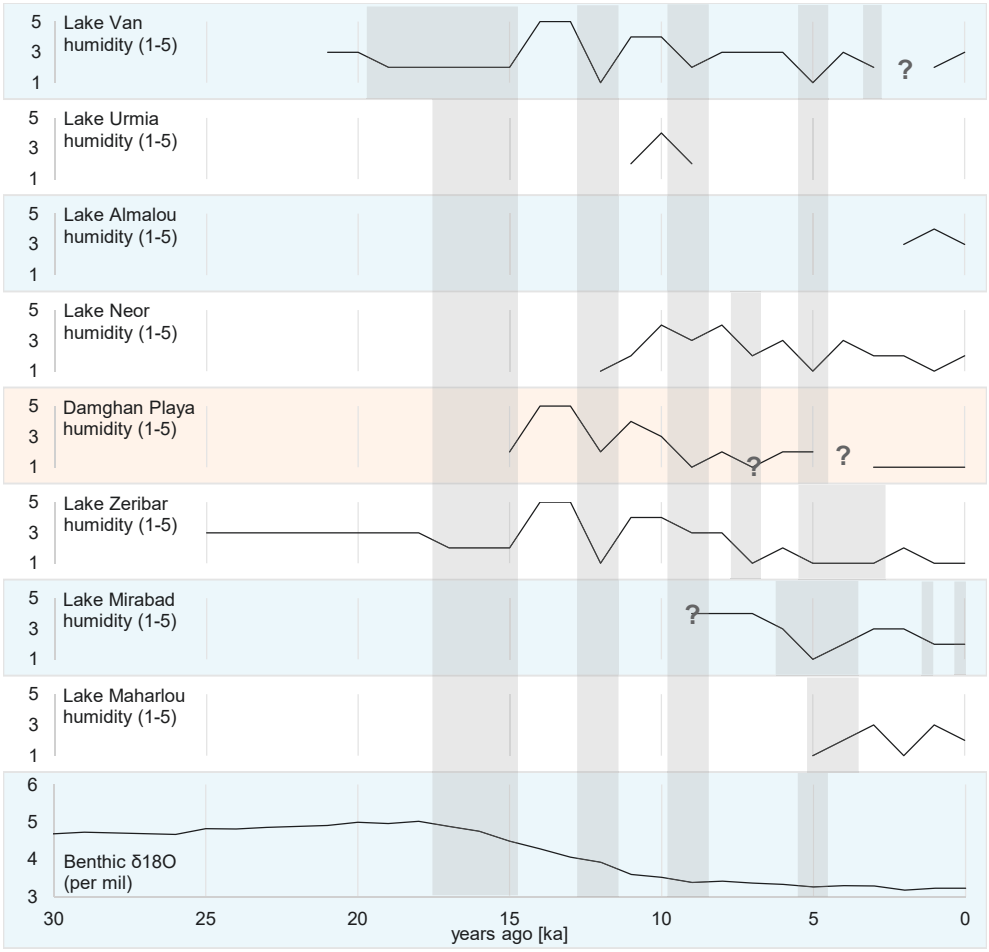

Source: Own illustration

5 Conclusions

5.1 Geomorphological relationships

The findings provide first information about geomorphologic relationships in the Basin of Damghan. The analysis of specific surface and subsurface characteristics led to a chronostratigraphic classification of the alluvial fan generations into two distinct active alluvial fan surfaces and five rather inactive classes of eroded fan surfaces. Their morphological relationship appears in the shape and alteration of their surfaces and with the topography of their geomorphologic system elements. In addition, the stratigraphy of some sections reveals intercalations of slack water deposits of a supposed former lake level. This directly links the alluvial fan surface generations to the variability of the lake's water budget. Thereby, the lake represents the erosional base and this again may control alluvial fan surface abandonment and the development of distinct surface generations.

The applied analytical geomorphological mapping approach helped to classify and quantify those alluvial surfaces as generations of denudational alluvial aprons and foot slopes. In addition, the geomorphological maps reveal surfaces of active slope-fluvial deposition, as well as their topologic relationship to the abandoned surfaces. The morphometric and morphographic classification of map unit borders and the definition of geomorphologic system contacts gives comprehensive insight into the geomorphology and development of these alluvial fan surfaces and enables further studies with independent hypotheses.

5.2 Geoarchives for morphogenetic correlation

Drying and lake level retreat or at least a lowering of former erosional basis is documented in the stratigraphic records of both terrestrial fluvial to lacustrine still water sediments and in playa deposits of the central depression. This can be seen in increasing grain sizes with reduced sorting, coincide with intensified evaporation and higher Ti/Al-ratio in playa sediments (cf. Büdel et al. 2017). This supports our hypothesis of high energy events leaving signals in both: terrestrial and lacustrine geoarchives with a certain synchronicity (Chap. 1). Even so, the geomorphological landform-succession and alluvial fan morphogenesis, such as the described progradation of young alluvial fans, confirms a lake level retreat. The correlation orders the different geoarchives in the mapping area into a firm sequence-stratigraphy, where the observed fluvial and alluvial surfaces are connected by distinct processes of erosion and accumulation. These typically occurred in individual phases with temporal and spatial gaps in sedimentation continuity, which leaves the correlation scattered. Regarding our research questions this leads to the following conclusions about the studied geoarchives:

1 Location:
Promising geoarchives in the basin are placed around the central archive, comprising the playa deposits. They are part of a sediment cascade which connected the morphodynamic and morphostructural properties (e.g. sedimentation phases, grain size distribution, lithology) of alluvial archives from the Alborz footslopes to fluvial and lacustrine archives of the central depression.

2 Types:
The archives of terrestrial type are formed by alluvial or fluvial morphogenesis, but can also incorporate former lacustrine phases. They are still systematic elements of alluvial and fluvial geomorphology and affected by periodically occurring erosion and sedimentation. Most recent lacustrine deposits in the playa are affected by groundwater and are periodically flooded. They provide non-continuous information with the best temporal resolution, but foremost the youngest layers are highly distorted by intensive evaporation and salt tectonic dynamics.

3 Evaluation:
Terrestrial archives such as alluvial fans and fluvial plains cover wide areas. Their near subsurface structure is chaotic and highly erratic in both vertical and lateral directions. Therefore, detailed information about surface ages and surface activity approved to be crucial for developing a proper sample strategy and for deriving samples from representative sediment bodies. In conjunction with this, surface morphology by itself constitutes the geoarchive and must be considered. Archive information from the lacustrine and playa sediments is predominantly structured by phases of changing salinity and high energy events. Fine layering and lamination showed to be underrepresented and imprinted by salt dynamics. Further studies and detailed investigations on the cores will focus on their paleo-ecological significance.

References

Abbas, A.; Khan, S. (2007): Using Remote Sensing Techniques for Appraisal of Irrigated Soil Salinity. In: L. Oxley and D. Kulasiri (Eds.): *International Congress on Modelling and Simulation (MODSIM).. Modelling and Simulation Society of Australia and New Zealand* (2632–2638). Brighton

Abbassi, M.; Farbod, Y. (2009): Faulting and folding in quaternary deposits of Tehran's piedmont (Iran). *Journal of Asian Earth Sciences 34* (4): 522–531.

Ad-hoc-AG Boden (2005): Bodenkundliche Kartieranleitung. 5. Aufl. Hannover: Schweizerbart.

Ad-Hoc-Arbeitsgruppe Geologie (Hg.) (2002): *Geologische Kartieranleitung. Allgemeine Grundlagen. Unter Mitarbeit von Carsten Schwarz, Lutz Katzschmann und Karl-Heinz Radzinski.* (Geologisches Jahrbuch Reihe G, 9). Hannover.

Aghanabati, A. (1994): *Sedimentary–Structural Units. 23rd Geoscience Conference of Iran.* Teheran: Geological Survey of Iran.

Aghanabati, A. (2004): *Geology of Iran.* Teheran: Geological Survey of Iran.

Airbus Defence and Space (2005): *SPOT DEM Product Description. Version 1.2.* Tolouse.

Alavi Panah, S. K.; Goosens, R.; Matinfar, H. R.; Mohamadi, H.; Ghadiri, M.; Irannegad, H.; Alikhah Asl, M. (2008): The Efficiency of Landsat TM and ETM+ Thermal Data for Extracting Soil Information in Arid Regions. *Journal of Agricultural Science and Technology 10*: 439–460.

Alavi, M. (1996): Tectonostratigraphic synthesis and structural style of the alborz mountain system in Northern Iran. *Journal of Geodynamics 21* (1): 1–33.

Allbed, A.; Kumar, L. (2013): Soil Salinity Mapping and Monitoring in Arid and Semi-Arid Regions Using Remote Sensing Technology. A Review. *Advances in Remote Sensing 02* (04): 373–385.

Anonymous, 2001. DIN EN 13346, (April 2001). *Charakterisierung von Schlämmen - Bestimmung von Spurenelementen und Phosphor - Extraktionsverfahren mit Königswasser* (Deutsche Fassung EN 13346: 2000), Beuth Verlag.

Azabdaftari, A.; Sunar, F. (2016): Soil Salinity Mapping Using Multitemporal Landsat Data. *The International Archives of the Photogrammetry, Remote Sensing and Spatial Information Sciences XLI-B7*: 3–9.

Berberian, M. (1974): *A geological description of North-Central Iran* (Report, 29). Tehran: Geological Survey of Iran.

Bertrams, M.; Protze, J.; Eckmeier, E.; Lehmkuhl, F. (2014): A geochemical approach on reconstructing Upper Pleistocene environmental conditions from wadi deposits – an example from the Wadi Sabra (Jordan). *Zeitschrift* für *Geomorphologie, Supplementary Issues 58* (1): 51–80.

Blott, S. J.; Pye, K. (2001): GRADISTAT. A grain size distribution and statistics package for the analysis of unconsolidated sediments. *Earth Surface Processes and Landforms 26* (11): 1237–1248.

Blume, H.-P.; Stahr, K.; Leinweber, P. (2010): Bodenkundliches Praktikum. Heidelberg: Spektrum Akademischer Verlag.

Bottema, S. (1986): A late quaternary pollen diagram from Lake Urmia (Northwestern Iran). *Review of Palaeobotany and Palynology 47* (3-4): 241–261.
Brauneck, J. (2010): *Late Quaternary Climate Changes in the Central Sahara. New evidence from palaeoenvironmental research in NE-Niger.* (Würzburger Geographische Arbeiten, 103). Würzburg: Würzburg University Press
Briere, P. R. (2000): Playa, playa lake, sabkha: Proposed definitions for old terms. *Journal of Arid Environments 45* (1): 1–7.
Brown, E. T.; Johnson, T. C.; Scholz, C. A.; Cohen, A. S.; King, J. W. (2007): Abrupt change in tropical African climate linked to the bipolar seesaw over the past 55,000 years. *Geophysical Research Letters 34* (20).
Brunsden, D. (1993): The persistence of landforme. In: Rhodes Whitmore Fairbridge and Karl-Heinz Pfeffer (Eds.): *Klimagenetische Geomorphologie. Climatogenetic geomorphology.* (Zeitschrift für Geomorphologie. Supplementary Issues, 93): 13–28.
Brunsden, D. (1996): Geomorphological events and landform change. *Zeitschrift für Geomorphologie, NF 40* (3): 273–288.
Brunsden, D. (2006): Formative Event. In: Andrew Goudie (Ed.): *Encyclopedia of Geomorphology: Volume 1: A–I. 2 Bände*: 404–405.
Bubenzer, O.; Besler Hanna (2010): Sands as Archives of Environmental Change. Examples from Egypt, Sudan and Namibia. In: Wilhelm J.G. Möhlig, Olaf Bubenzer and Gunter Menz (Eds.): *Towards Interdisziplinarity. Experiences of the Long-term ACACIA Project*. (Topics in Interdisciplinary African Studies, 15): 23–48. Köln: Rüdiger Köppe Verlag.
Büdel, C.; Padashi, S. M.; Hoelzmann, P.; Fuchs, M.; Baumhauer, R. (2017): The correlation of North-Iranian Late-Pleistocene and Holocene playa sediments to basin geomorphology. In: *Zeitschrift* für *Geomorphologie, Supplementary Issues 61* (1): 77–99.
Buggle, B.; Glaser, B.; Hambach, U.; Gerasimenko, N.; Marković, S. (2011): An evaluation of geochemical weathering indices in loess–paleosol studies. *Quaternary International 240* (1-2): 12–21.
Busche, D.; Siefker, U. (2004): *Endbericht zum BMBF-Vorhaben 50EE0042 DRYSAT-MAP, Entwicklung einer neuen, anwendungsorientierten geomorphologischen Kartiermethode* für Trockengebiete mittels hochauflösender Satellitenbilddaten. Würzburg: Selbstverlag.
Çağatay, M.; Öğretmen, N.; Damcı, E.; Stockhecke, M.; Sancar, Ü.; Eriş, K.; Özeren, S. (2014): Lake level and climate records of the last 90ka from the Northern Basin of Lake Van, eastern Turkey. *Quaternary Science Reviews 104:* 97–116.
Chen, H.-F.; Yeh, P.-Y.; Song, S.-R.; Hsu, S.-C.; Yang, T.-N.; Wang, Y. et al. (2013): The Ti/Al molar ratio as a new proxy for tracing sediment transportation processes and its application in aeolian events and sea level change in East Asia. *Journal of Asian Earth Sciences 73*: 31–38.
Chivas, A. R. (2007): Terrestrial Evaporites. 10th Chapter. In: David J. Nash and Sue J. McLaren (Eds.): *Geochemical Sediments and Landscapes*: 331–364. Malden, MA: Blackwell Publishing Ltd.
Costantini, L.; Dyson, R. H., JR. (1990): The Ancient agriculture of the Damghan plain: The archaeobotanical evidence from Tepe Hissar. In: Naomi F. Miller (Ed.):

Economy and Settlement in the Near East: Analyses of Ancient Sites and Materials. Philadelphia: 47–68.: MASCA, The University Museum of Archaeology and Anthropology (MASCA Research Papers in Science and Archaeology, 7). Pennsylvania: University of Pennsylvania Press.

de Boer, Gerben B. J.; Weerd, C. de; Thoenes, D.; Goossens, H. W. J. (1987): Laser Diffraction Spectrometry: Fraunhofer Diffraction Versus Mie Scattering. *Particle & Particle Systems Characterization 4* (1-4): 14–19.

Demek, Jaromir (Ed.) (1982): *Geomorphologische Kartierung in mittleren Maßstäben. Grundlagen, Methoden, Anwendungen* (1. dt.-spr. Aufl.) (Petermanns geographische Mitteilungen Ergänzungsheft, 281). Gotha: Haack.

Demek, Jaromír; Gellert, Johannes F. (Eds.) (1976): *Handbuch der geomorphologischen Detailkartierung. International Geographical Union.* Wien: Hirt.

Djamali, M.; Beaulieu, J.-L. de; Shah-hosseini, M.; Andrieu-Ponel, V.; Ponel, P.; Amini, A. et al. (2008): A late Pleistocene long pollen record from Lake Urmia, NW Iran. *Quaternary Research 69* (3): 413–420.

Djamali, M.; Beaulieu, J.-L. de; Andrieu-Ponel, V.; Berberian, M.; Miller, N. F.; Gandouin, E. et al. (2009a): A late Holocene pollen record from Lake Almalou in NW Iran. Evidence for changing land-use in relation to some historical events during the last 3700 years. *Journal of Archaeological Science 36* (7): 1364–1375.

Djamali, M.; Beaulieu, J.-L. de; Miller, N. F.; Andrieu-Ponel, V.; Ponel, P.; Lak, R. et al. (2009b): Vegetation history of the SE section of the Zagros Mountains during the last five millennia; a pollen record from the Maharlou Lake, Fars Province, Iran. *Vegetation History and Archaeobotany 18* (2): 123–136.

Douaoui, A. E. K.; Nicolas, H.; Walter, C. (2006): Detecting salinity hazards within a semiarid context by means of combining soil and remote-sensing data. *Geoderma 134* (1-2): 217–230.

Drury, S. A. (2001): *Image interpretation in geology* (3rd ed). Malden, MA: Blackwell Science.

Eugster, H. P. (1980): Geochemistry of evaporitic lacustrine deposits. *Annual Review of Earth and Planetary Sciences 8* (1): 35–63.

Eugster, H. P.; Hardie, L. A. (1978): Saline Lakes. In: Abraham Lerman and P. Baccini (Eds.): *Lakes. Chemistry, geology, physics*: 237–293. New York: Springer.

FAO (2006): *Guidelines for soil description* (4th ed.) Rome: Food and Agriculture Organization of the United Nations.

FAO (2012): *Harmonized World Soil Database*. (version 1.2). Rome (Italy), Luxenburg (Austria): Food and Agriculture Organization of the United Nations.

Fattahi, M.; Walker, R.; Hollingsworth, J.; Bahroudi, A.; Nazari, H.; Talebian, M. et al. (2006): Holocene slip-rate on the Sabzevar thrust fault, NE Iran, determined using optically stimulated luminescence (OSL). *Earth and Planetary Science Letters 245* (3-4): 673–684.

Federal Geographic Data Committee (Eds.) (2006): *FGDC Digital Cartographic Standard for Geologic Map Symbolization* (Document Number FGDC-STD-013-2006). Reston, Va: U.S. Geological Survey.

Finné, M.; Holmgren, K.; Sundqvist, H. S.; Weiberg, E.; Lindblom, M. (2011): Climate in the eastern Mediterranean, and adjacent regions, during the past 6000 years – A review. *Journal of Archaeological Science 38* (12): 3153–3173.

Folk, R. L.; Ward, W. C. (1957): Brazos River bar [Texas]; a study in the significance of grain size parameters. *Journal of Sedimentary Research 27* (1): 3–26.

Francus, P.; Lamb, H.; Nakagawa, T.; Marshall, M.; Brown, E. (2009): The potential of high-resolution X-ray fluorescence core scanning: Applications in paleolimnology. *PAGES newsletter 17*(3): 93–95.

Fuchs, M.; Dietze, M.; Al-Qudah, K.; Lomax, J. (2015): Dating desert pavements – First results from a challenging environmental archive. *Quaternary Geochronology 30*: 342–349.

Fuchs, M.; Lang, A. (2009): Luminescence dating of hillslope deposits—A review. *Geomorphology 109* (1-2): 17–26.

Fuchs, M.; Wagner, G. A. (2003): Recognition of insufficient bleaching by small aliquots of quartz for reconstructing soil erosion in Greece. *Quaternary Science Reviews 22* (10-13): 1161–1167.

Gansser, A.; Huber, H. (1962): Geological observations in the central Elburz, Iran. *Schweizerische mineralogische und petrographische Mitteilungen 42* (2): 584–630.

Geyer, G.; Bayet-Goll, A.; Wilmsen, M.; Mahboubi, A.; Moussavi-Harami, R. (2014): Lithostratigraphic revision of the middle Cambrian (Series 3) and upper Cambrian (Furongian) in northern and central Iran. *Newsletters on Stratigraphy 47* (1): 21–59.

Goudie, A. (2013): *Arid and semi-arid geomorphology*. Cambridge: Cambridge University Press.

Griffiths, H.; Schwalb, A.; Stevens, L. (2001): Environmental change in southwestern Iran: The Holocene ostracod fauna of Lake Mirabad. *The Holocene 11* (6): 757–764.

Gustavsson, M.; Kolstrup, E. (2009): New geomorphological mapping system used at different scales in a Swedish glaciated area. *Geomorphology 110* (1-2): 37–44.

Gustavsson, M.; Kolstrup, E.; Seijmonsbergen, A. C. (2006): A new symbol-and-GIS based detailed geomorphological mapping system: Renewal of a scientific discipline for understanding landscape development. *Geomorphology 77* (1-2): 90–111.

Gustavsson, M.; Seijmonsbergen, A. C.; Kolstrup, E. (2008): Structure and contents of a new geomorphological GIS database linked to a geomorphological map — With an example from Liden, central Sweden. *Geomorphology 95* (3-4): 335–349.

Haas, T. de; Ventra, D.; Carbonneau, P. E.; Kleinhans, M. G. (2014): Debris-flow dominance of alluvial fans masked by runoff reworking and weathering. *Geomorphology 217*: 165–181.

Hamdi, B. (1989): *Stratigraphy and Paleontology of the Late Precambrian to Early Cambrian in the Alborz Mountains Northern Iran*. Tehran: Geological Survey of Iran.

Handford, C. R. (1981): A process-sedimentary framework for characterizing recent and ancient sabkhas. *Sedimentary Geology 30* (4): 255–265.

Harvey, A. M. (2012): The coupling status of alluvial fans and debris cones: a review and synthesis. *Earth Surface Processes and Landforms 37* (1): 64–76.

Hijmans, R. J.; Cameron, S. E.; Parra, J. L.; Jones, P. G.; Jarvis, A. (2005): Very high resolution interpolated climate surfaces for global land areas. *International Journal of Climatology 25* (15): 1965–1978.

Hollingsworth, J.; Nazari, H.; Ritz, J.-F.; Salamati, R.; Talebian, M.; Bahroudi, A. et al. (2010): Active tectonics of the east Alborz mountains, NE Iran: Rupture of the left-lateral Astaneh fault system during the great 856 A.D. Qumis earthquake. *Journal of Geophysical Research 115* (B12).

IUSS Working Group WRB (2007): *World Reference Base for Soil Resources 2006. Ein Rahmen für internationale Klassifikation, Korrelation und Kommunikation. 1. Update 2007* (dt. Ausg.). Hannover: BGR.

IUSS Working Group WRB (2015): *World Reference Base for Soil Resources 2014. International soil classification system for naming soils and creating legends for soil maps. 1st update 2015* (World Soil Resources Reports, 106). Rome: FAO.

Jansen, M. (2007): *Digitale geomorphologische Kartographie. Potenziale der Informationstechnologie zur Weiterentwicklung eines geowissenschaftlichen Kartenwerks*. Diplomarbeit. Rheinische Friedrich-Wilhelms-Universität. Bonn: Geographisches Insititut.

Jol, H. M. (2009): *Ground Penetrating Radar Theory and Applications*. Burlington: Elsevier.

Kamp, A. E.; Dean, J.; Pearce, R. B.; Pike, J. (2001): Recognition and analysis of bedding and sediment fabric features. In: William M. Last and John P. Smol (Eds.): *Tracking environmental change using lake sediments. Physical and Geochemical Methods* (Developments in paleoenvironmental research, 2): 7–23. Dordrecht, Boston, London: Kluwer Academic Publishers.

Kerry, R.; Rawlins, B. G.; Oliver, M. A.; Lacinska, A. M. (2009): Problems with determining the particle size distribution of chalk soil and some of their implications. *Geoderma 152* (3-4): 324–337.

Kober, F.; Zeilinger, G.; Ivy-Ochs, S.; Dolati, A.; Smit, J.; Kubik, P. (2013): Climatic and tectonic control on fluvial and alluvial fan sequence formation in the Central Makran Range, SE-Iran. *Global and Planetary Change 111*: 133-149.

Kottek, M.; Grieser, J.; Beck, C.; Rudolf, B.; Rubel, F. (2006): World Map of the Köppen-Geiger climate classification updated. *Meteorologische Zeitschrift 15* (3): 259–263.

Krinsley, D. B. (1970): *A geomorphological and paleoclimatological study of the playas of Iran. Final report 1965 - 1970. Ed. by Geological Survey (U.S.) and Air Force Cambridge Research Laboratories (U.S.).* Bedford, Mass: U.S. Air Force; Geological Survey (U.S.).

Kushnir, J. (1982): The partitioning of seawater cations during the transformation of gypsum to anhydrite. *Geochimica et Cosmochimica Acta 46* (3): 433–446.

Lehner, B.; Grill, G. (2013): Global river hydrography and network routing. Baseline data and new approaches to study the world's large river systems. *Hydrological Processes 27* (15): 2171–2186.

Leser, H. (1977): *Feld- und Labormethoden der Geomorphologie* (1. Aufl.) (De Gruyter Lehrbuch). Berlin, New York: De Gruyter.

Leser, H.; Stäblein, G. (1985): Legend of the geomorphological map 1 : 25 000 (GMK 25). Fifth version in the GMK priority program of the Deutsche Forschungsgemeinschaft. In: Dietrich Barsch and Herbert Liedtke (Eds.): *Geomorphological mapping in the Federal Republic of Germany. Contributions to the GMK-prioritypro-gramm IV* (Berliner geographische Abhandlungen, 39): 61–89. Berlin: Institut für Physische Geographie der Freien Universität Berlin.

Leser, H.; Stäblein, G.; Göbel, P. (1975): *Geomorphologische Kartierung. Richtlinien zur Herstellung geomorphologischer Karten 1:25000. GMK-Schwerpunktprogramm* (2. veränderte Auflage) (Berliner geographische Abhandlungen, Sonderheft). Berlin: Institut für Physische Geographie der Freien Universität Berlin.

Li, C.; Yang, S. (2010): Is chemical index of alteration (CIA) a reliable proxy for chemical weathering in global drainage basins? *American Journal of Science 310* (2): 111–127.

Lisiecki, L. E.; Raymo, M. E. (2005): A Pliocene-Pleistocene stack of 57 globally distributed benthic δ 18 O records. *Paleoceanography 20* (1): n/a.

Lisle, R. J.; Brabham, P.; Barnes, J. W. (2011): *Basic geological mapping* (5th ed.) (The geological field guide series). Chichester, West Sussex, Hoboken, NJ: Wiley-Blackwell.

Lomax, J.; Kreutzer, S.; Fuchs, M. (2014): Performance tests using the Lexsyg luminescence reader. *Geochronometria 41* (4): 327–333.

McLennan, S. M. (1993): Weathering and Global Denudation. 100th Anniversary Symposium: Evolution of the Earth's Surface. *The Journal of Geology 101* (2): 295–303.

Milsom, J. (2003): *Field geophysics* (3rd ed.) (The geological field guide series). Chichester, Hoboken, N.J.: Wiley.

Modarres, R.; Sarhadi, A. (2011): Statistically-based regionalization of rainfall climates of Iran. *Global and Planetary Change 75* (1-2): 67–75.

Modarres, R.; Sarhadi, A.; Burn, D. H. (2016): Changes of extreme drought and flood events in Iran. *Global and Planetary Change 144*: 67–81.

Munsell Color (2009): *Munsell Soil Color Charts* (2009-year rev.). Grand Rapids, MI: Munsell Color.

Murray, A. S.; Wintle, A. G. (2000): Luminescence dating of quartz using an improved single-aliquot regenerative-dose protocol. *Radiation Measurements 32* (1): 57–73.

NASA Goddard Space Flight Centre (2016): *Landsat 7 Science Data Users Handbook*. Access at 01.11.2016, http://landsat.gsfc.nasa.gov/.

NASA JPL (2009): *ASTER Global Digital Elevation Model*. Access at 01.11.2016, https://lpdaac.usgs.gov/products/astgtmv002/.

NASA JPL (2013): *NASA Shuttle Radar Topography Mission Global 3 arc second*. Access at 01.11.2016, https://lpdaac.usgs.gov/products/srtmgl3v003/.

Nesbitt, H. W.; Young, G. M. (1982): Early Proterozoic climates and plate motions inferred from major element chemistry of lutites. *Nature 299* (5885): 715–717.

Nichols, G. J. (2009): *Sedimentology and stratigraphy* (2nd ed.), Chichester, UK, Hoboken, NJ: Wiley-Blackwell.

Okrusch, M.; Matthes, S. (2010): *Mineralogie. Eine Einführung in die spezielle Mineralogie, Petrologie und Lagerstättenkunde* (8. Aufl.). Berlin, Heidelberg: Springer.

Olaya, V. (2009): Chapter 6 Basic Land-Surface Parameters. In: Tomislav Hengl and Hannes I. Reuter (Eds.): *Geomorphometry. Concepts, software, applications* (Developments in soil science, 33): 141–169. (1st ed.). Amsterdam, Oxford: Elsevier.

Park, C.-S.; Hwang, S.; Yoon, S.-O.; Choi, J. (2014): Grain size partitioning in loess-paleosol sequence on the west coast of South Korea using the Weibull function. *Catena 121*: 307–320.

Playà, E.; Rosell, L. (2005): The celestite problem in gypsum Sr geochemistry. An evaluation of purifying methods of gypsiferous samples. *Chemical Geology 221* (1-2): 102–116.

Preusser, F.; Degering, D.; Fuchs, M.; Hilgers, A.; Kadereit, A.; Klasen, N. et al. (2008): Luminescence dating: basics, methods and applications. *E&G – Quaternary Science Journal 57* (1-2): 95-149;

Ramezani, E.; Marvie Mohadjer, M. R.; Knapp, H.-D.; Ahmadi, H.; Joosten, H. (2008): The late-Holocene vegetation history of the Central Caspian (Hyrcanian) forests of northern Iran. *The Holocene 18* (2): 307–321.

Regard, V.; Bellier, O.; Braucher, R.; Gasse, F.; Bourlès, D.; Mercier, J. et al. (2006): 10Be dating of alluvial deposits from Southeastern Iran (the Hormoz Strait area). *Palaeogeography, Palaeoclimatology, Palaeoecology 242* (1-2): 36–53.

Reu, J. de; Bourgeois, J.; Bats, M.; Zwertvaegher, A.; Gelorini, V.; Smedt, P. de et al. (2013): Application of the topographic position index to heterogeneous landscapes. *Geomorphology 186*: 39–49.

Reuter, H. I.; Nelson, A.; Jarvis, A. (2007): An evaluation of void-filling interpolation methods for SRTM data. *International Journal of Geographical Information Science 21* (9): 983–1008.

Rezaeian, M. (2008): *Coupled tectonics, erosion and climate in the Alborz Mountains, Iran*. PhD thesis. University of Cambridge.

Rieben, H. (1955): The geology of the Teheran plain. *American Journal of Science 253* (11): 617–639.

Rieben, H. (1966): *Geological observations on alluvial deposits in Northern Iran.* (Sāzmāni Zamīn-Šināsī-i Kišwar: Report, 9). Tehran: Geological Survey of Iran.

Rizza, M.; Mahan, S.; Ritz, J.-F.; Nazari, H.; Hollingsworth, J.; Salamati, R. (2011): Using luminescence dating of coarse matrix material to estimate the slip rate of the Astaneh fault, Iran. *Quaternary Geochronology 6* (3-4): 390–406.

Robinson, C.; El-Baz, F.; Kusky, T.; Mainguet, M.; Dumay, F.; Al Suleimani, Z.; Al Marjeby, A. (2007): Role of fluvial and structural processes in the formation of the Wahiba Sands, Oman: A remote sensing perspective. *Journal of Arid Environments 69* (4): 676–694.

Rothwell, R. G.; Rack, F. R. (2006): New techniques in sediment core analysis. An introduction. In: Guy R. Rothwell (Ed.): *New techniques in sediment core analysis* (Special Publication, 267): 1–29. London: Geological Society.

Schäfer, A. (2005): *Klastische Sedimente. Fazies und Sequenzstratigraphie* (1. Aufl.). München, Heidelberg: Elsevier, Spektrum Akad. Verl.

Scheffer, F.; Schachtschabel, P.; Blume, H.-P. (2010): *Lehrbuch der Bodenkunde* (16. Aufl.) (Spektrum Lehrbuch). Heidelberg, Berlin: Spektrum, Akad. Verl.

Schmidt, E. Friedrich (1937): *Excavations at Tepe Hissar, Damghan. With an additional chapter on the Sasanian Building at Tepe Hissar.* (Publications of the Iranian Section of the University Museum). Philadelphia: University of Pennsylvania Press.

Schmidt, K.-H. (2009): Hillslopes as Evidence of Climatic Change. In: A. J. Parsons, A. D. Abrahams, Anthony J. Parsons and Athol D. Abrahams (Eds.): *Geomorphology of Desert Environments* (2. Aufl.): 675–694. Dordrecht: Springer; Springer Netherlands.

Schneevoigt, N. J.; van der Linden, S.; Thamm, H.-P.; Schrott, L. (2008): Detecting Alpine landforms from remotely sensed imagery. A pilot study in the Bavarian Alps. *Geomorphology 93* (1-2): 104–119.

Schnurrenberger, D.; Russel, J.; Kelts, K. R. (2003): Classification of lacustrine sediments based on sedimentary components. *Journal of Paleolimnology 29* (2): 141–154.

Schrott, L.; Sass, O. (2008): Application of field geophysics in geomorphology: Advances and limitations exemplified by case studies. *Geomorphology 93* (1-2): 55–73.

Schütt, B. (2004): The chemistry of playa-lake-sediments as a tool for the reconstruction of Holocene environmental conditions - a case study from the central Ebro basin. In: Werner Smykatz-Kloss and Peter Felix-Henningsen (Eds.): *Paleoecology of Quaternary Drylands* (Lecture Notes in Earth Sciences, 102): 5–30. Berlin, Heidelberg: Springer.

Seijmonsbergen, A. C. (2013): 14.4 The Modern Geomorphological Map. In: John F. Shroder (Eds.): *Treatise on Geomorphology*: 35–52. London, Waltham, MA: Academic Press.

Shahrabi, M. (1991): *Geological Map of Gorgan. 1 / 250 000* (Geological Quadrangle Map of Iran, No. H4). Tehran: Geological Survey of Iran.

Shanahan, T. M.; Peck, J. A.; McKay, N.; Heil, C. W.; King, J.; Forman, S. L. et al. (2013): Age models for long lacustrine sediment records using multiple dating approaches – An example from Lake Bosumtwi, Ghana. *Quaternary Geochronology 15*: 47–60.

Sharifi, A.; Pourmand, A.; Canuel, E. A.; Ferer-Tyler, E.; Peterson, L. C.; Aichner, B. et al. (2015): Abrupt climate variability since the last deglaciation based on a high-resolution, multi-proxy peat record from NW Iran. The hand that rocked the Cradle of Civilization? *Quaternary Science Reviews 123*: 215–230.

Singhvi, A. K.; Porat, N. (2008): Impact of luminescence dating on geomorphological and palaeoclimate research in drylands. *Boreas 37* (4): 536–558.

Smith, D. G.; Jol, H. M. (1995): Ground penetrating radar. Antenna frequencies and maximum probable depths of penetration in Quaternary sediments. *Journal of Applied Geophysics 33* (1-3): 93–100.

Smith, M. J. d.; Goodchild, M. F.; Longley, P. A. (2015): *Geospatial Analysis. A Comprehensive Guide to Principles, Techniques and Software Tools* (5th ed.). Access at 13.03.2016, https://spatialanalysisonline.com.

Smith, Mike J.; Paron, Paolo; Griffiths, James S. (Eds.) (2011): *Geomorphological mapping. Methods and applications* (1st ed.). Oxford: Elsevier.

Smykatz-Kloss, W., Felix-Henningsen, P. (Eds.) (2004): *Paleoecology of Quaternary Drylands* (Lecture Notes in Earth Sciences, 102): 5–30. Berlin, Heidelberg: Springer.

Snyder, J.; Wasylik, K.; Fritz, S.; Wright, H. J. (2001): Diatom-based conductivity reconstruction and palaeoclimatic interpretation of a 40-ka record from Lake Zeribar, Iran. *The Holocene 11* (6): 737–745.

Stäblein, Gerhard (Hg.) (1978): *Geomorphologische Detailaufnahme. Beiträge zum GMK-Schwerpunktprogramm I* (Berliner geographische Abhandlungen, 30). Berlin: Institut für Physische Geographie der Freien Universität Berlin.

Stanley-Wood, N. (2005): Particle Characterisation in Bulk Powders. In: Don McGlinchey (Ed.): *Characterisation of Bulk Solids*: 1–47. Oxford, UK: Blackwell Publishing Ltd.

Staubwasser, M.; Weiss, H. (2006): Holocene climate and cultural evolution in late prehistoric–early historic West Asia. *Quaternary Research 66* (3): 372–387.

Stevens, L. R.; Ito, E.; Schwalb, A.; Wright, H. E. (2006): Timing of atmospheric precipitation in the Zagros Mountains inferred from a multi-proxy record from Lake Mirabad, Iran. *Quaternary Research 66* (3): 494–500.

Stöcklin, J. (1971): *Stratigraphic lexicon of Iran. 1, Central, North and East Iran*. (Sāzmāni Zamīn-Šināsī-i Kišwar: Report, 18). Tehran: Geological Survey of Iran.

Stöcklin, J.; Ruttner, A.; Nabavi, M. H. (1964): *New data on the lower paleozoic and pre-cambrian of north Iran* (Report / Geological Survey of Iran, no. 2). Tehran: Geological Survey of Iran.

Stow, D. A. (2008): *Sedimentgesteine im Gelände. Ein illustrierter Leitfaden. Unter Mitarbeit von V. Schweizer und J. Seeling* (1. Aufl.). Heidelberg, Neckar: Spektrum Akademischer Verlag.

Taghizadeh Mehrjardi, R.; Mahmoodi, S.; Taze, M.; Sahebjalal, E. (2008): Accuracy Assessment of Soil Salinity Map in Yazd-Ardakan Plain,Central Iran, Based on Landsat ETM+ Imagery. *American-Eurasian Journal of Agricultural and Environmental Sciences 3* (5): 708–712.

Thornton, C. P.; Rehren, T. (2009): A truly refractory crucible from fourth millennium Tepe Hissar, Northeast Iran. *Journal of Archaeological Science 36* (12): 2700–2712.

Tucker, M. E. (2011): *Sedimentary rocks in the field. A practical guide* (4th ed.) (The geological field guide series). Chichester, West Sussex, Hoboken, NJ: Wiley-Blackwell.

U.S. Geological Survey (2016): *LANDSAT 8 (L8) - Data Users Handbook* (Version 2.0) (Landsat Project Documents, LSDS-1574). Sioux Falls, SD: U.S. Geological Survey. Access at 01.11.2016, https://www.usgs.gov/land-resources/nli/landsat/landsat-project-documents.

Ullmann, T. (2015): *Characterization of Arctic Environment by Means of Polarimetric Synthetic Aperture Radar (PolSAR) Data and Digital Elevation Models (DEM).* Dissertation. Universität Würzburg. Würzburg: Institut für Geographie und Geologie.

Ullmann, T.; Büdel, C.; Baumhauer, R.; Padashi, S. M. (2016): Sentinel-1 SAR Data Revealing Fluvial Morphodynamics in Damghan (Iran): Amplitude and Coherence Change Detection. *International Journal of Earth Science and Geophysics 2* (1): 1–14.

Ullmann, T.; Büdel, C.; Baumhauer, R. (2017): Characterization of Arctic Surface Morphology by Means of Intermediated TanDEM-X Digital Elevation Model Data. *Zeitschrift* für *Geomorphologie, Supplementary Issues 61* (1): 3–25.

USGS National Cooperative Geologic Mapping Program (NCGMP) (Ed.) (2011): *NCGMP09—Draft Standard Format for Digital Publication of Geologic Maps* (Version 1.1.). Access at 31.10.2016, http://ngmdb.usgs.gov/Info/standards/NCGMP09/

Vaziri, S. H.; Majidifard, M. R. (2000): *Geological Map of Shahrud. 1 / 100 000*. Tehran: Geological Survey of Iran.

Vogel, S.; Märker, M.; Rellini, I.; Hoelzmann, P.; Wulf, S.; Robinson, M. et al. (2015): From a stratigraphic sequence to a landscape evolution model. Late Pleistocene and Holocene volcanism, soil formation and land use in the shade of Mount Vesuvius (Italy). *Quaternary International 394:* 155–179.

Walker, R.; Fattahi, M. (2011): A framework of Holocene and Late Pleistocene environmental change in eastern Iran inferred from the dating of periods of alluvial fan abandonment, river terracing, and lake deposition. *Quaternary Science Reviews 30* (9-10): 1256–1271.

Warren, J. K. (2016): *Evaporites.* Cham: Springer International Publishing.

Wasylikowa, K.; Witkowski, A.; Walanus, A.; Hutorowicz, A.; Alexandrowicz, S. W.; Langer, J. J. (2006): Palaeolimnology of Lake Zeribar, Iran, and its climatic implications. *Quaternary Research 66* (3): 477–493.

West, I. (1973): Vanished Evaporites--Significance of Strontium Minerals. *SEPM Journal of Sedimentary Research 43* (1): 278–279.

Wick, L.; Lemcke, G.; Sturm, M. (2003): Evidence of Lateglacial and Holocene climatic change and human impact in eastern Anatolia: high-resolution pollen, charcoal, isotopic and geochemical records from the laminated sediments of Lake Van, Turkey. *The Holocene 13* (5): 665–675.

Wintle, A. G. (2008): Luminescence dating. Where it has been and where it is going. *Boreas 37* (4): 471–482.

Online Supplement

The e-book version of this study as well as supplementary maps are freely available online at the repository of the University of Würzburg:
https://doi.org/10.25972/WUP-978-3-95826-115-0

Appendix I
Damghan Basin, 1 : 25 000 Geomorphological Maps

Following map sheets are compiled in this Appendix:

- *Sheet 6962IV-SW "Geomorphological map of Shahrak-e-Mehmandust"*
- *Sheet 6962IV-SE "Geomorphological map of Kalateh-Molla"*
- *Sheet 6962III-NW "Geomorphological map of Mehmandust"*
- *Sheet 6962III-NE "Geomorphological map of Pariabad"*
- *Sheet 6962III-SE "Geomorphological map of Kavir-e-Haj Aligholi"*

Appendix II
Stratigraphic Overview Map

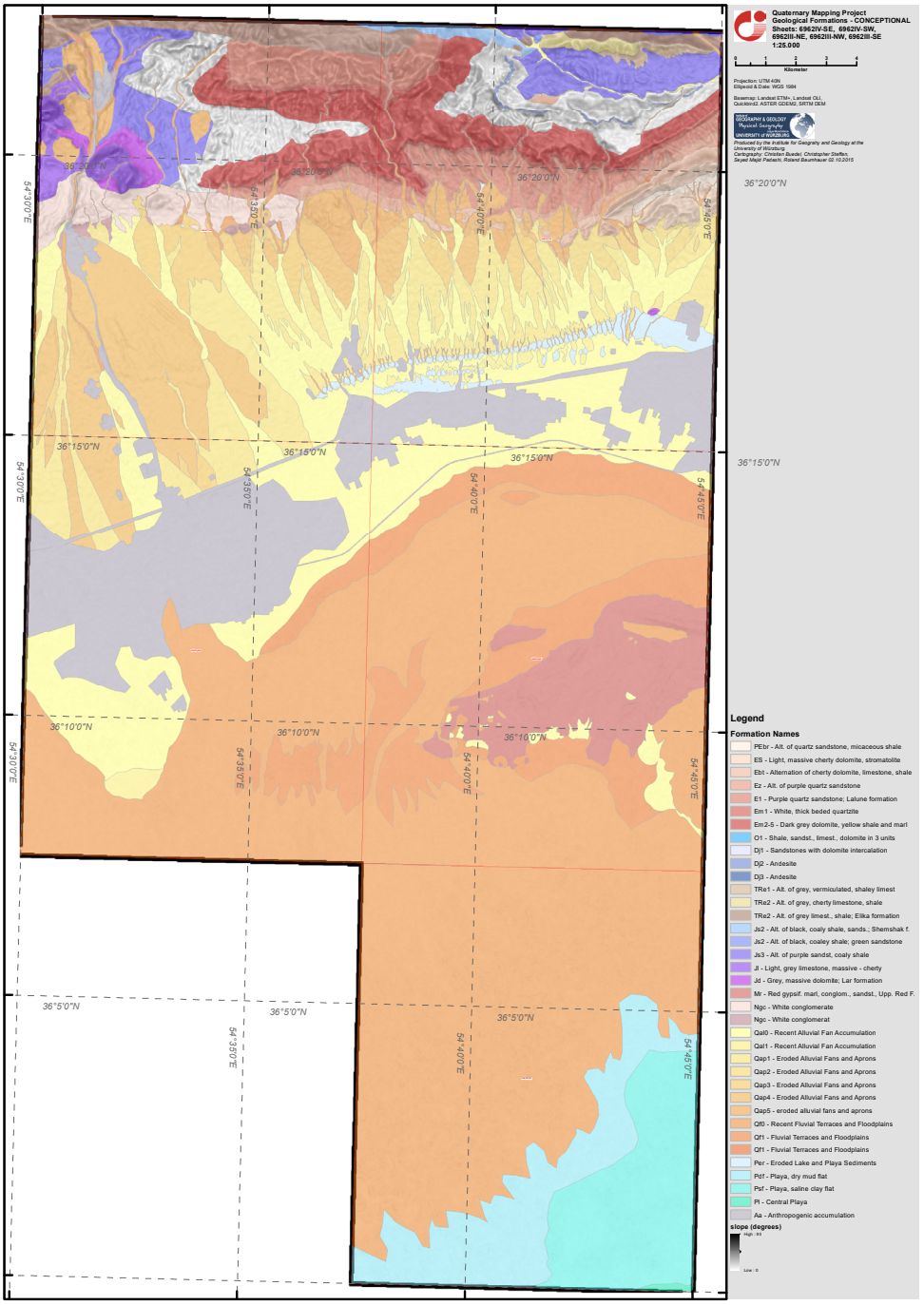

GGW
Geographische Gesellschaft Würzburg

Würzburger Geographische Arbeiten

Availability of water and desiccation of important water reservoirs is a vital challenge in semi-arid to arid climates with growing economy and population. Low quantities of precipitation and high evaporation rates leave the water supply vulnerable to human activity and climatic variations. Endorheic basins of North Iran were hydrologically landlocked within geological timescales and thus bear evidence of past variations of water resources in generations of water related landforms, like abandoned lake level shorelines, alluvial fans and stream terraces. Understanding the development of these landforms reveals crucial information about past water reservoirs and landscape history.

This study offers a comprehensive approach on understanding the geomorphological development of the landscape throughout Late Pleistocene and Holocene times. It integrates remote sensing and geographic information system analysis with geomorphological and stratigraphical mapping fieldwork and detailed sedimentological investigations.

The work shows the importance of analytical geomorphological mapping for delineating stratigraphic units of the Iranian Quaternary. Thus, several phases of drying and lake level retreat were identified in parallel geoarchives and could be dated to a time span from today to Late Pleistocene. The findings link the fate of the citizens of the ancient city of 'Tepe Hissar' to their access to water and to the power of geomorphological processes, which started changing their environment.

ISBN 978-3-95826-114-3

Würzburg University Press